MPHIL

Blast impact simulation on composite military armours

Dolce, Nando

Award date:
2009

Awarding institution:
University of Bath

Blast impact simulation on composite military armours

Department of Mechanical Engineering

Capt. Ferdinando Dolce

A thesis submitted for the
Degree of Master of Philosophy

February 2009

This page is intentionally left blank

TABLE OF CONTENTS

Chapter 4 – Finite Element Method (FEM) applied to blast load phenomenon

Chapter 5 – Composite materials experimental data: EUROPA programme tests

Chapter 6 – FEM models

Chapter 7 – Results of FE models and comparison with experimental tests

LIST OF FIGURES

LIST OF TABLES

to my Queen Annamaria and my little Princess Chiara, with love

ACKNOWLEDGEMENTS

I would like to thank everyone that has played a part in this work and contributed to his completion.
Many thank to my Italian Air Force Commanders, in particular to L.T.Col. Manuele Bernabei, who encouraged and promoted this Master trusting in my technical skills.
Thank you to QinetiQ® Company, in the persons of Dr. Mark French and Mr. Andrew Wright, for the fundamental data provided to realise this study.
A big thank to all my friends and colleagues both at University and from home. From those of you at University's office that satisfied my annoying requests of borrowing their PCs to run more and more simulations, to those that have sustained me with their genuine friendship, particularly in the last four months. A special mention at Ettore Barbieri, till the end a huge help for the development of this work.
Sincere thanks to my supervisor Dr. Michele Meo for the technical support, constantly and generously given for the whole academic year.

Lastly, a special thank to my wife Annamaria. Without her support this experience in UK would have been much more stressful… your smiles, your patience and your love have brought the sunshine in the dark days of this way!

This page is intentionally left blank

SUMMARY

Civil and military structures, such as helicopters, aircrafts, navies, tanks or buildings are exposed more and more to blast threats as both terroristic attacks in Western World and guerrilla warfare scenarios in Middle East are increasing.

During an explosion the peak pressure produced by shock wave is much greater than the static collapse pressure. Metallic structures usually undergo large plastic deformations absorbing blast energy before reaching equilibrium. Due to their high specific properties, fibre-reinforced polymers are being considered for energy absorption applications in Armoured Fighting Vehicles (AFVs), where improved strategic and operational air mobility are key requirements.

A deep insight into the relationship between explosion loads, composite architecture and deformation/fracture behaviour will offer the possibility to design structures with significantly enhanced energy absorption and blast resistance performance.

This study examines the performance of both metallic and composite plates subjected to blast loads using commercial Finite Element Method (FEM) explicit code LS-DYNA with a particular attention to hybrid composite panels. The thesis deals with numerical 3D simulations of response caused by air blast waves generated by C-4 charges on fully clamped rectangular targets.

Two different approaches have been used to simulate the blast load. Firstly CONWEP load function was applied in order to generate the blast equivalent pressure distribution on the Lagrangian plate model. The second approach considered Multi Materials Arbitrary Lagrangian Eulerian (MMALE) formulation to simulate the shock phenomenon. Numerical results have been presented and compared with the tests performed by the EUROPA Research Technology Programme (RTP) military consortium and kindly provided by QinetiQ® showing an acceptable agreement.

OUTCOME

The thesis deals with FEM numerical 3D simulations of the effects that induce air blast waves generated by C-4 charges on fully clamped rectangular targets made of steel and composite material.
For the steel model simulations excellent results were obtained in terms of both dynamic and residual deflection.
Regarding the composite models, assuming the composite matrix failure as the damage criterion, these very well simulated the CFRP armour tests, while in the case of hybrid targets the capability to predict the experimental results is slightly less reliable, probably due to the insufficient availability of experimental data. A reasonably good agreement between numerical and experimental results was also found in terms of fracture morphology.

This page is intentionally left blank

CHAPTER 1

Introduction

1.1 Literature review - structural material analysis under blast load

Structural materials behaviour under blast load is a relatively recent issue that during the last years has been concerning more and more both academic world and military industry as terroristic attacks [1] and guerrilla warfare contexts are becoming more and more frequent. In this scenario, studies regarding protection against landmine threats of army vehicles, buildings and personnel have been having an increasing role in Defence research. Since the costs of experimental trials are usually very high [2, 3] numerical FEM analysis can be an useful tool in order to minimize the number of experiments and, also, to understand general phenomenological aspects.

The first studies regarding the response of structural components to blast loads concerned homogenous metal beams and plates [4-14] were focused on the effect of boundary, load and material properties in order to understand the physical phenomenon and to classify the failure morphologies.

Initially three failure modes on fully clamped aluminium beams subjected to increasing uniform impulsive loads were identified [6] (Figure 1):

- mode I *"large ductile deformation"*;
- mode II *"tensile-tearing and deformation"*;
- mode III "*transverse shear*.

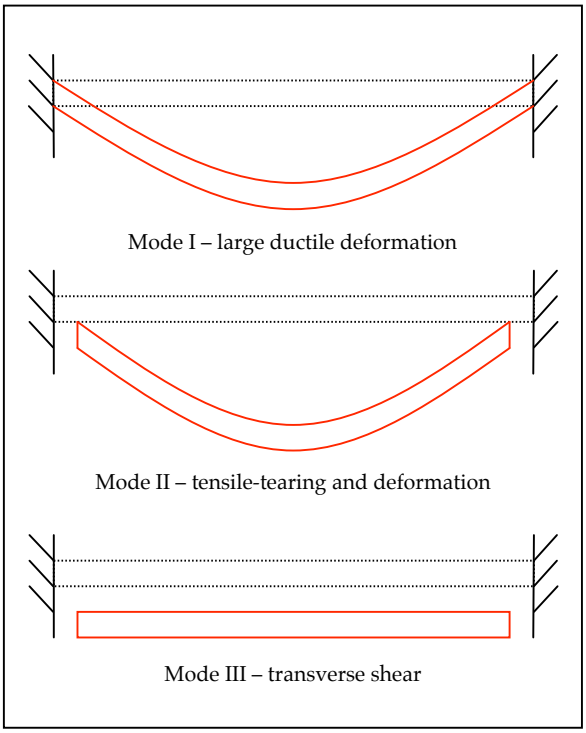

Figure 1 - Failure modes of fully clamped aluminium beams subjected to increasing uniform impulsive loads

In the same load conditions, the failure modes of circular [9] and square [11, 14] plates were found very similar to the beam ones. However, Nurick and Shave [14] observed three further phases for the failure mode II:

- mode II* where the plate exhibits only partial tearing and the mid-point deformation continues to increase with increasing impulse;
- mode IIa where the plate is completely failed and the mid-point deformation continues to increase with increasing impulse;
- mode IIb where the plate is totally torn but the mid-point deflection decreases with increasing impulse.

They also compared the response of square and circular plate showing that mode IIa applies only to square plates. As observed by Shen and Jones these failure mode are obviously also related to boundary conditions [12, 15].
A certain number of studies concerned also the behaviour of structural components under localised blast load [16-21]. The response to this different load condition is not significantly different from the previous one. The principal difference is the comparison of a new failure mode, called *"capping mode"*, that is thinning and tearing of a central fragment or "cap". This latter

failure mode was sub-divided by Nurick and Radford [17] in three further failure modes, that are:

- mode Itc: large inelastic response with thinning in the central area;
- mode II*c: partial tearing in the central area;
- mode IIc: complete tearing in the central area "capping failure".

The mode IIc "capping failure" seems to be related to thermo-mechanical instability as Wiehahn *et al.* [19, 20] showed through a numerical model of circular plates with temperature-dependent material properties.

The first studies regarding the effects of blast loads on composite structures were driven by maritime defence engineering demand. A fairly wide number of studies, in fact, concerned the effects of underwater blast shock on fibre-reinforced polymer matrix composites. Mouritz and co-workers investigated their influence on the fatigue life, damage, failure and bending properties [22-26]. They showed that glass reinforced plastic (GRP) panels backed by air and loaded by underwater blast wave at low overpressure exhibit only matrix cracking, while, as load increases, the damage appears in form of fibre failure and delamination. These damages imply reduction of both tensile and compressive strength, elastic modulus [22], fatigue life [23] and bending strength and modulus [26]. Further studies [25] demonstrated that for composites produced by resin transfer moulding the damage produced by blast load starts from original composite defects. Mouritz also verified the positive role of stitching in increasing the resistance capability of polymer composite against both ballistic and explosive threats. Composites stitched in the through-thickness direction with thin Kevlar®-49 yarn exhibited an increasing Mode I inter-laminar fracture toughness improving the damage resistance to explosive blast loading. However, in this case, additional localised damages in the GRP close to the stitches as well as lower tensile strength at higher shock load were found [24].

Comtois *et al.* [27] analysed the effect of explosives on polymer matrix composite laminates focusing on the effect of the joining methods applied on the composite panel. They also studied the effect of two kind of attachment, bonded and clamped, revealing that the joining method is the main factor influencing the pattern of damage. The damage found in adhesively bonded samples was less than that produced in clamped

structures and this is proportional to the applied impulse. Furthermore, carbon fibre composite panels exhibited a higher fibre resistance than the lower strength glass fibre.
In 2002 Franz [28] published a work regarding experimental investigation into the response of glass-fibre chopped-strand mat laminates subjected to air blast pressure. In this work the author indentified three different damage modes:

- matrix cracking (*incipient damage*);
- delamination/debonding;
- penetration (*final damage*).

The damage endurance of each mode, damage propagation with increasing pressure impulse, damage distribution in the thickness direction of the targets and the way the blast attenuation and large-area support change the target resistance were analysed at relatively small charges. Laminated strength was found to improve by increasing the thickness, although delamination/debonding resistance decreased with increasing thickness and areal density. Moreover the impulse thresholds for the onset of delamination and perforation were found that increased with areal density. This study suggested the use of composite with different mechanical properties through the thickness that is high energy absorbing for the external layer in front of the charge and rear layer with high flexural rigidity. Since thermosetting-based fibre metal laminates (FML) such as GLARE have a certain number of disadvantage like long processing cycles, low inter-laminar fracture toughness and lack of reparability, Langdon et co-workers [29] investigated the response under blast impact of thermoplastic FML based on unidirectional glass fibre reinforced polypropylene (GFPP). Energy absorbing capability was found through delamination at the 0°/90° interface (Figure 2), debonding between aluminium and composite (Figure 3 - a), perforation of the panels and spalling/petalling of the rear surface aluminium layer (Figure 3 - b). In order to classify the failure mode for laminated materials, the authors also stated new failure modes (Table 1) [29] that are the traditional failure modes [4-14] adapted and expanded to include the failure morphologies observed in these 2/1 (that is 2 layers of aluminium and 1 of composite) laminated materials.

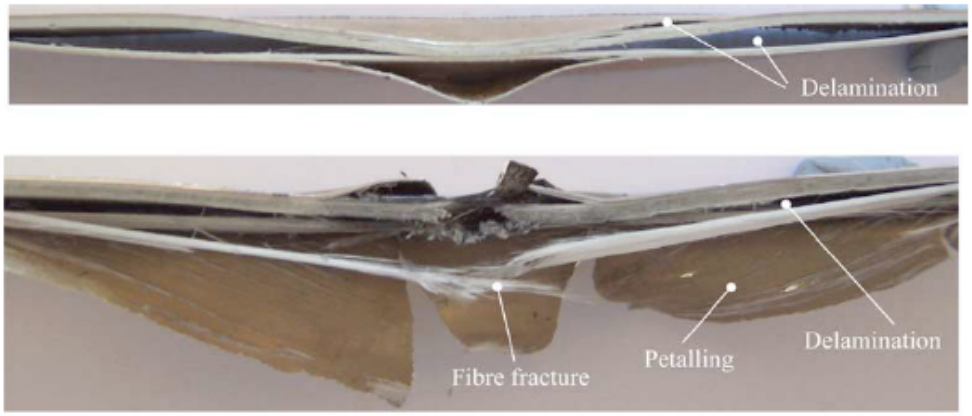

Figure 2 – Delamination, petalling and fibre fracture of thermoplastic FML based on GFPP under blast impact [29]

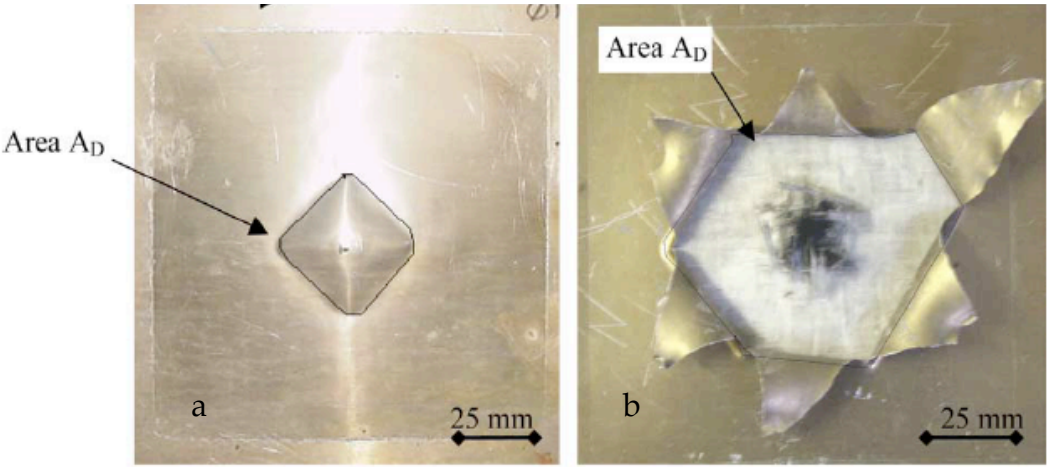

Figure 3 – Debonding (a) and spalling/petalling (b) of the rear surface aluminium layer [29]

Table 1 - Failure mode for laminated materials under blast impact [29]

In Mode I failure category	
Mode Idb	Large inelastic deformation with debonding evident in the cross-section
Mode Idl	Large inelastic deformation with delamination of the composite plies
Mode Idbdl	Large inelastic deformation with debonding and delamination
In Mode II* failure category	
Mode IIdb	Partial tearing (no petals) with debonding evident in the cross-section
In Mode II failure category	
Mode IIsp	Symmetric petalling of the panel
Mode IIspr	Symmetric petalling of the rear surface of the laminated panel
Mode IIspf	Symmetric petalling of the front surface of the laminated panel
Mode II sprf	Symmetric petalling of the rear and front surfaces of the laminated panel
Mode II spe	Symmetric petalling with the petals elongated in one direction
Mode II spre	Symmetric petalling of the panel rear surface, elongated in one direction

The influence of the thickness and material distribution on FML blast response was examined by Lemansky [30]. No important difference between

different plates of similar overall thickness and increasing number of layers was found, suggesting that debonding does not absorb a significant amount of explosion energy. Moreover, thicker and thinner panels have different front and rear layer deformations. Because thicker panels have a higher bending stiffness they show larger debonded area. This is because for thick panels' debonding is a less energetic failure mechanism compared to plate bending.

The response under blast load of FMLs manufactured using 2024-O aluminium and woven glass fibre-reinforced polyamide 6,6 (GFPA) was also studied [31]. Aluminium/GFPA interlaminar fracture toughness was found significantly lower (940 J/m^2) than aluminium/GFPP fracture resistance but greater than that measured on other thermosetting composites. On the back face the damage exhibited diamond and circular shape dependent upon the panel thickness (Figure 4).

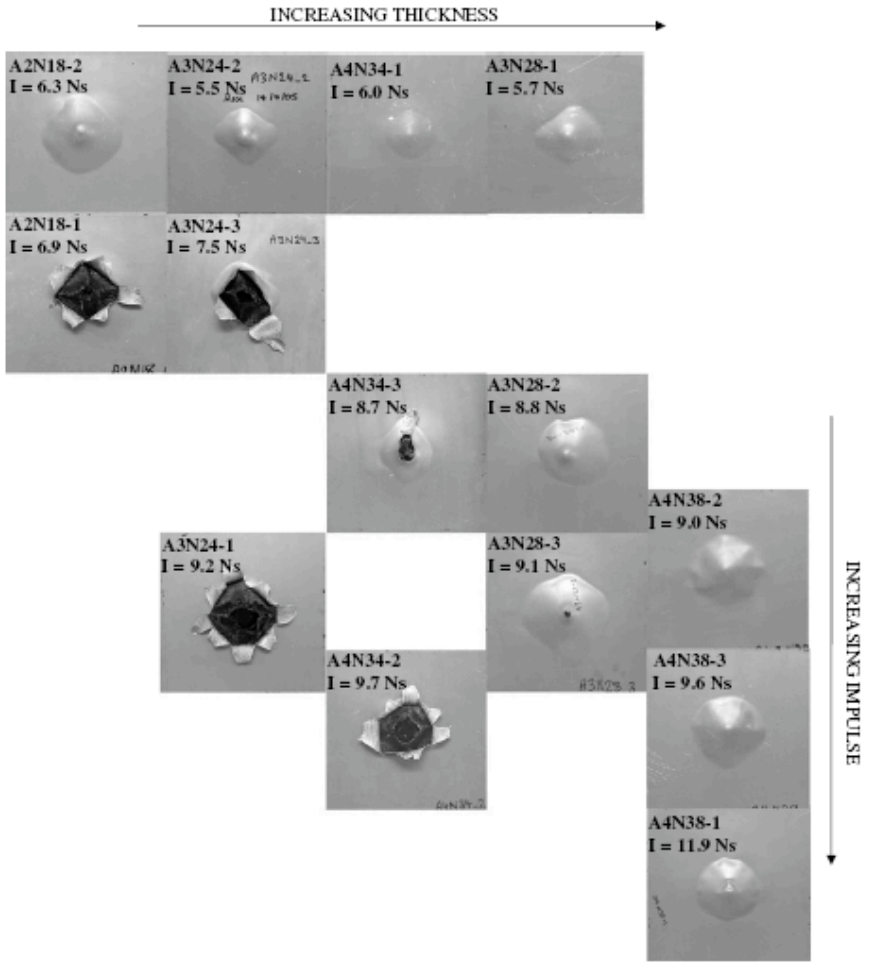

Figure 4 – Back face damage increasing thickness and impulse [31]

Thin panels showed diamond damage while thicker (>10 mm) panels had a less defined damage shape. On the front face different damages, such as pitting (Figure 5), global displacement and tearing were observed. Cross section inspection also showed multiple debonding and delamination, large plastic displacement and fibre breakage (Figure 6).

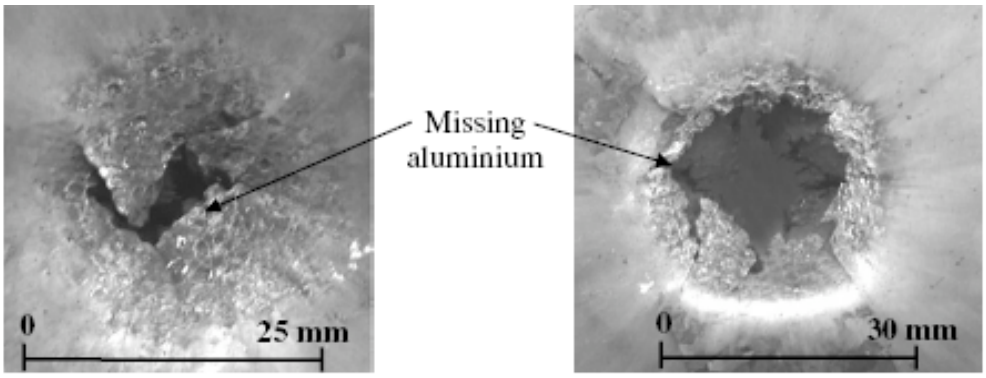

Figure 5 – Pitting on the front face [31]

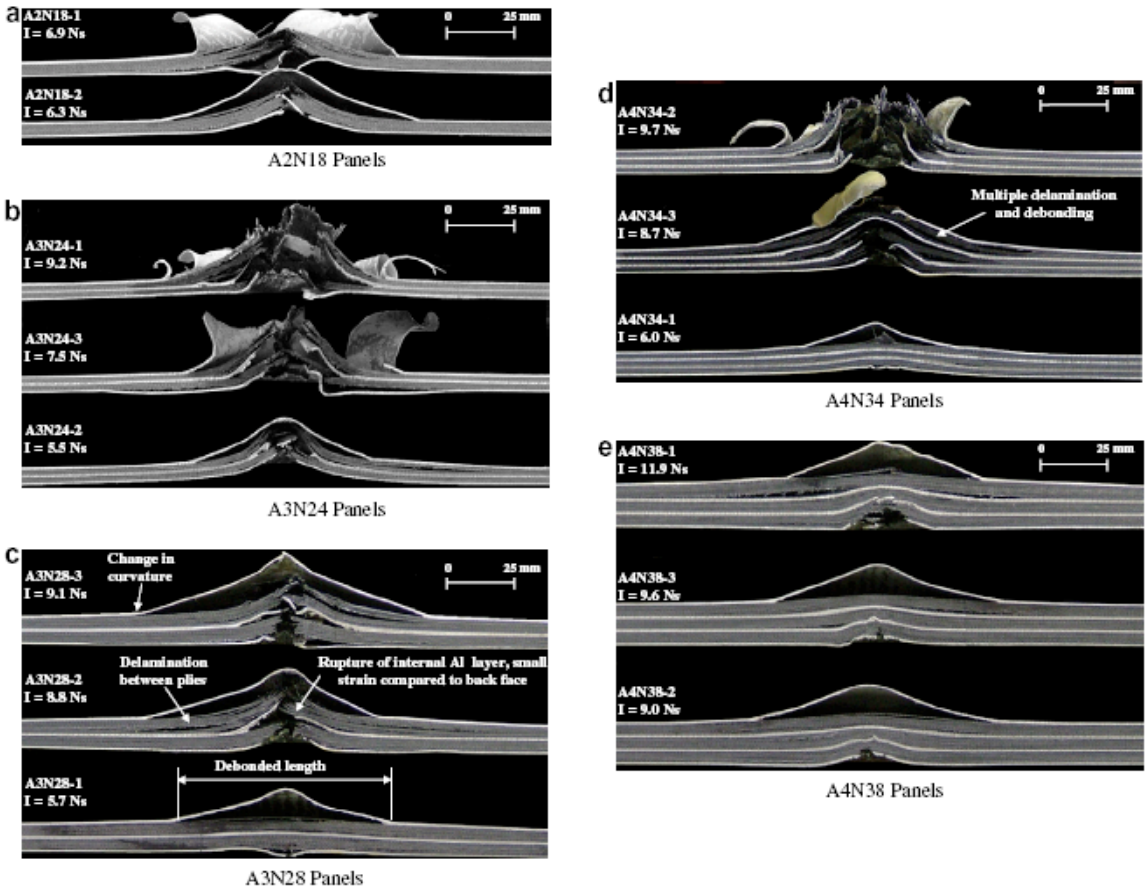

Figure 6 - Cross section debonding, delamination, large plastic deformation and fibre breakage [31]

Regarding analytical and numerical works, although modelling of blast impact on structures is quite complex due to the dependence on both load history and boundary conditions, a rather wide literature about prediction of structures behaviour under blast load can be found.

In the 90s Olson and Nurick analysed stiffened and un-stiffened clamped square mild steel plates under uniformly distributed blast load [11, 32]. In the case of un-stiffened plate the non linear numerical models showed strain rate-sensitive plates exhibiting mode I, mode II and a trend towards mode III failure as the load intensity increases. For the stiffened plates, mode I is predicted well for both maximum deflection and deformation shape, while initiation of mode II is predicted by a maximum strain criterion but with an insufficient number of data for conformation. However, few years later Rudrapatna *et al.* [33, 34], applying super-plate element formulation, introduced a new FE model that was able to reproduce modes II and III, the failure progression and complete tearing with also post-failure analysis.

In 2001 Wang [2] presented a benchmark work of simulation of explosion in soil and air using LS-DYNA commercial code and Eulerian formulation. From this report it appears that for a landmine explosion simulation results are in a satisfactory agreement with experiments. Although the predicted pressure is in certain cases 50% greater than the measured one, the author showed how this overpressure decreases as the Eulerian mesh size decreases.

Jacob *et al* and Ramajeyathilagam [35, 36] carried out numerical simulation of blast impact in air on mild steel quadrangular plates (1.6, 2.0, 3.0 and 4.0 mm) with ABAQUS/explicit and underwater on mild steel rectangular plates (0.002 mm thick) with DYNA3D respectively, obtaining reasonably good predictions. Balden [37] described numerical simulation results of experiments on mild-steel plates presented in [9] with uniform blast loading and in [38] with localised blast loading. The author used finite element code ABAQUS to simulate the structural response and hydro-dynamic code AUTODYN to determine localised blast pressure, time and spatial history showing a good correlation with experiments in terms of energy, input, large inelastic deformations and post-failure motion.

Chung, Longdon, Yuen and Nurick analysed [39, 40] the response of mild steel plates at different stiffener conditions to both uniform and localised blast loading. The simulation was conducted using ABAQUS/Explicit with

temperature-dependent material properties and strain rate sensitivity. The numerical results well predicted large inelastic deformation and the tearing by high-temperature bands. The influence of support configurations was numerically analysed for the first time by Gupta and Nagesh [41] who performed some transient dynamic finite element analysis of circular plates by varying support configurations under uniform single square wave form impulsive load in ANSYS, comparing the results with experimental test presented in Refs. [9] and [13]. Mode II failure was simulated using a rupture strain criteria, while mode III using a shear strain failure criteria as proposed by Jones [42]. The authors also proposed a stiffness reduction approach in order to influence the initiation and progression of tearing under modes II and III.

Recently Bonorchis and Nurick [15] presented the results of a series of experiments finalized to understand how the boundary conditions influence the response of a mild steel plate under localised blast load. The experiments were performed using a ballistic pendulum and showed that the impulse measured increases as the height of the clamps increases. The authors pointed out that, although the impulse changes as the boundary conditions change, the plate deformation does not change, meaning that not all the impulse measured is transformed in deformation energy.

1.2 Lightweight Armoured Fighting Vehicles (AFVs)

Modern military vehicles are a compromise between the need of a great mobility and the increasing payload request [43]. These fairly opposite design requirements are leading the development of lightweight AFVs and research into lightweight vehicle structures are playing an important role in this process.

With the associated request for lighter protection systems, there has been an increasing move towards armour systems which are both structural and protection components at the same time. Fibre-reinforced composite materials respond to this demand as an acceptable combination of structural performance and low density. In particular, carbon fibre reinforced plastics (CFRP) exhibit excellent specific structural properties.

1.3 Thesis objective and structure

The aim of this thesis is to develop a 3D numerical model in order to simulate the behaviour of composite (laminated and hybrid) clamped panel under uniform free air blast impact.

The literature survey showed that neither experimental nor numerical works regarding uniform blast impact response of clamped hybrid glass/carbon fibre laminated composite panels are available.

Numerical model was developed through FE explicit commercial code LS-DYNA. Firstly a clamped monolithic steel rolled homogenous armour (RHA) panel were modelled with two different approaches and the numerical results were compared with experimental data in order to validate the simulation approach, then the composite models were developed. Both metallic and composite models have been carried out at the same stand-off distance with increasing mass charge (decreasing scaled distance).

The numerical results were compared with experimental results obtained by EUROPA RTP consortium and kindly provided by QinetiQ® Company.

This page is intentionally left blank

CHAPTER 2

Blast waves

2.1 Introduction

This chapter provides an overview of blast loads and associated effects.

2.2 Detonation and explosion

From a scientific point of view there is an explosion if:

> *"…energy is released over a sufficiently small time and in a sufficiently small volume so as to generate a pressure wave of finite amplitude travelling away from the source [...] however, the release is not considered to be explosive unless it is rapid enough and concentrated enough to produce a pressure wave that one can hear. Even though many explosions damage their surroundings, it is not necessary that external damage be produced by explosion. All that is necessary is that the explosion is capable of being heard."* (Baker and Strehlow, 1976 p.106) [44].

There are many types of sources which generate explosions, such as high explosives, fuel-air explosive and nuclear bombs and the blast wave produced can be strongly affected by the kind of explosive material. However, explosive needs a detonator and a booster charge in order to generate an explosion. Detonator and booster produce a shock wave of sufficient energy to realize a sustained chemical reaction in the explosive material [45]. This shock wave compresses and heats the explosive material above its ignition point. At this point it starts a chemical reaction within a confined area just behind the shock wave called the reaction zone. If velocity of reaction is equal to explosive shock velocity, the reaction and the propagation are called detonation and detonation wave respectively. During detonation, pressure rises rapidly (Von Neuman spike - Figure 7) and produces the reaction. In Figure 7 the Chapman-Jouguet (C-J) point

represents the state of the detonation products at the end of the reaction zone [46].

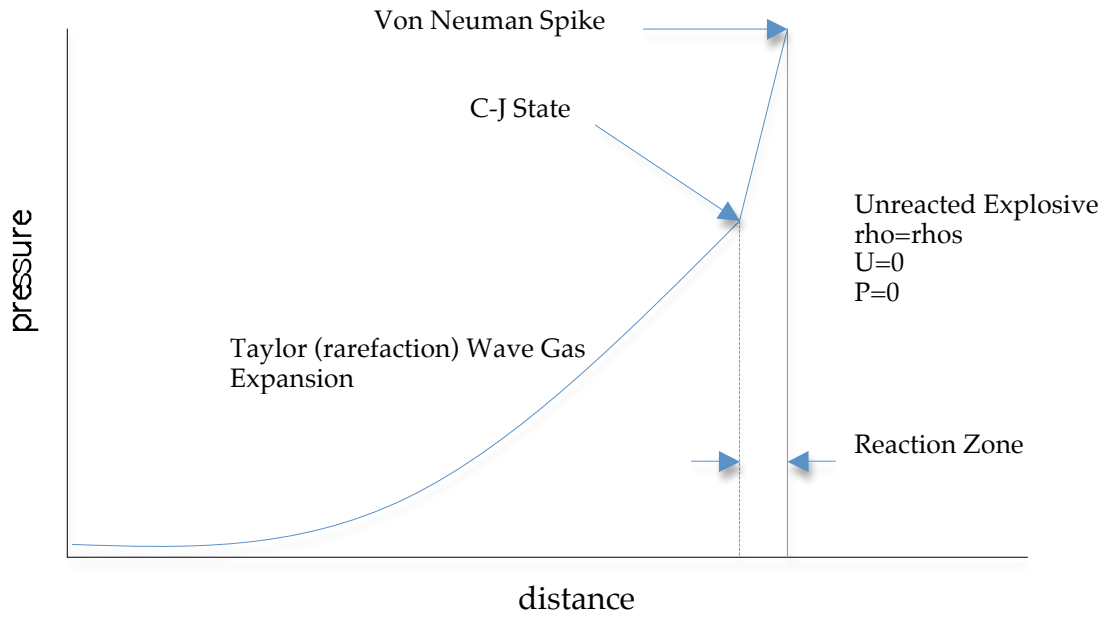

Figure 7 - Pressure vs distance diagram of a detonation wave [46]

Detonation produces a rapid release of energy that produces a sudden local increase of temperature and pressure. The reaction heat produces a high pressure shock wave also called *blast* wave propagating at high velocity in the surrounding medium.

2.3 Blast wave

Blast wave is characterized by a rapid and strong increase of pressure that decreases with the time, as described for the ideal case by the following equation (Figure 8) [47]:

$$p(t) = (P_{s0} + P_{amb})(1-\tau)(ae^{-\alpha\tau} + be^{-\beta\tau}) \qquad (1)$$

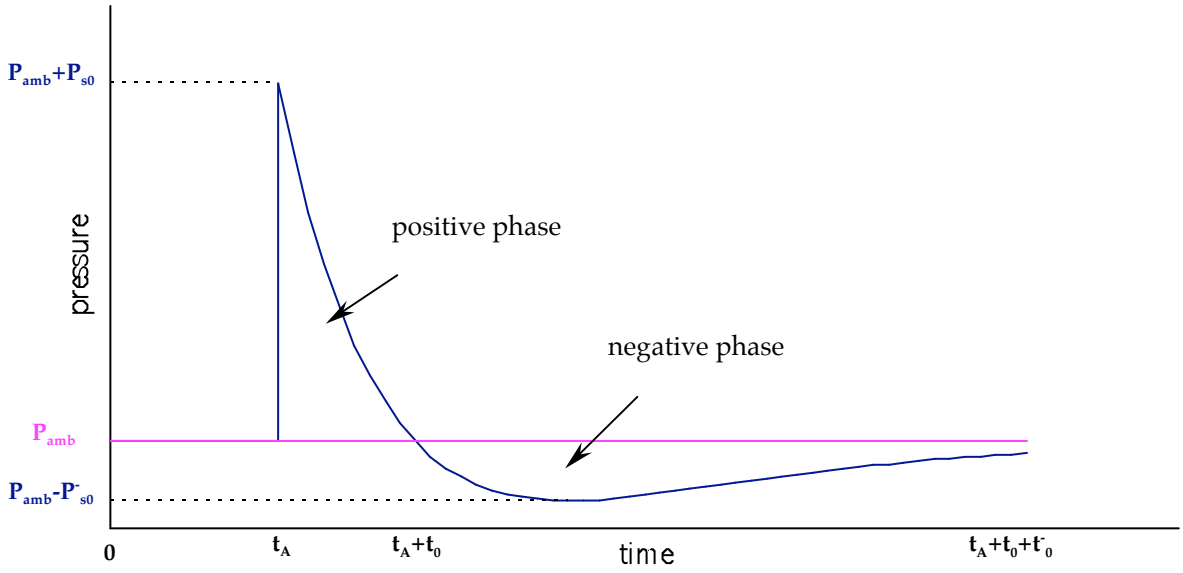

Figure 8 – Blast wave pressure – time history

where P_{s0} is the peak overpressure (shock front), a and b functions of peak overpressure, α and β decay parameters, τ the dimensionless abscissa t/t_0 and t_0 the duration of positive phase.

P_{s0} decreases with the time, but also with the distance from the source. Furthermore moving away from the shock front the pressure reaches a value below the pressure ambient P_{amb}. In this zone the air is sucked instead of being pushed (negative phase). The negative phase is caused by the vacuum produced by the rarefaction of the gas during the explosive reaction.

As blast wave travels into the air, the mass of medium behind the front produces a wind, whose intensity will depend on the density and on velocity of the air. This wind is called dynamic pressure whose positive phase is usually longer than the overpressure positive phase. Also if the overpressure is the main cause of destruction during an explosion, in some cases dynamic pressure can be significantly important [48].

The properties of a blast wave are related to properties directly measurable or to the damages that the shock front produces on the structures situated in the surrounding ambient. Hence for thin walled structures design the main effect of an explosion are both peak overpressure and primary fragments.

Positive and negative impulses are important parameters that characterize the blast wave and are defined by:

$$i_s^+ = \int_{t_A}^{t_A+t_0} [p(t) - P_{amb}]\,dt \qquad (2)$$

$$i_s^- = \int_{t_A+t_0}^{t_A+t_0+t_0^-} [P_{amb} - p(t)]\,dt \qquad (3)$$

2.4 Scaling laws

The magnitude of an explosion depends on the amount of energy released, expressed in energy units, as Calories or Joule, but in certain cases a relative measure for explosion size may be more practical. This requires a sort of standard that is the energy released by TNT (symmetrical trinitrotoluene), chosen because it is a chemically pure material. The character of the blast waves from condensed high explosive is nearly similar to those of TNT. Besides, TNT gives quite reproducible blast effects and the curve (1) generated by TNT can be used for other explosives by calculating an equivalent charge weight of the explosive required to produce the same effect as a spherical TNT explosive. The explosion of one gram of TNT produces an explosion energy of about 1120 cal (~4700 J), but because of some uncertainty in the measured values during both laboratory and field tests, it was generally accepted a different arbitrary standard for blast waves. This corresponds to a blast energy release of 1E+06 kilocalories for 1 ton of TNT that is in approximate agreement with average experimental values [49].

Blast wave characteristics will depend on both explosive energy release and physical properties of medium surrounding the point source, as density and temperature. However, in certain cases throughout specific scaling laws it is possible to transfer the results of a specific explosive test, in terms of blast wave properties, into another test with different conditions. These laws are based on geometrical similarities and they have the same principles of any other kind of scaling law. Through these laws, for example, a test conducted at sea level ambient atmospheric conditions gives results that can predict the response of explosives detonated at high altitude conditions, while two explosions can have the same blast wave overpressure at distances that are proportional to the cube root of the respective energy release. That is to produce a given blast impulse at twice a given distance requires eight times

the explosive energy release. This scaling law is the most common form of blast scaling, also called "cube-root" scaling, formulated by Hopkinson (1915) and independently by Cranz (1926). This law states that "*self-similar blast waves are produced at identical scaled distance when two explosive charge of similar geometry and of the same explosive, but of different sizes, are detonated in the same atmosphere"* [50].

The scaled distance is usually defined with a dimensionless parameter:

$$Z = \frac{R}{E^{1/3}} \quad \text{or} \quad Z = \frac{R}{W^{1/3}} \tag{4}$$

where R is the distance from the center of the explosive source, E is the total explosive energy released by the detonation (represented by the heat of detonation of the explosive, H), and W is the total weight of a standard explosive, such as TNT, that can represent the explosive energy. Blast data at a distance R from the center of an explosive source of characteristic dimension D will be subjected to a blast wave with amplitude of P, duration T and a characteristic time history showed in the equation (1). The integral of the pressure-time history is the total impulse I defined as the sum of (2) and (3). The Hopkinson-Cranz scaling law then states that such data at a distance λR from the center of a similar explosive source of characteristic dimension λD detonated in the same atmosphere will define a blast wave of similar form with amplitude P, duration λT and impulse λI (Figure 9). The characteristic times are scaled by the same factor as the length scale factor λ [51]. In Hopkinson-Cranz scaling, pressures, temperatures, densities, and velocities are unchanged at homologous times. The Hopkinson-Cranz scaling law was thoroughly verified by many experiments conducted over a large range of explosive charge energies. Limited reflected impulse measurements showed that Hopkinson-Cranz scaling may become inapplicable for close-in detonations, e.g. Z<0.4 ft/lb1/3 (0.16 m/kg1/3) [52]. Generally, the equivalent weight factors found by comparing blast data from different high explosives vary slightly with scaled distance.

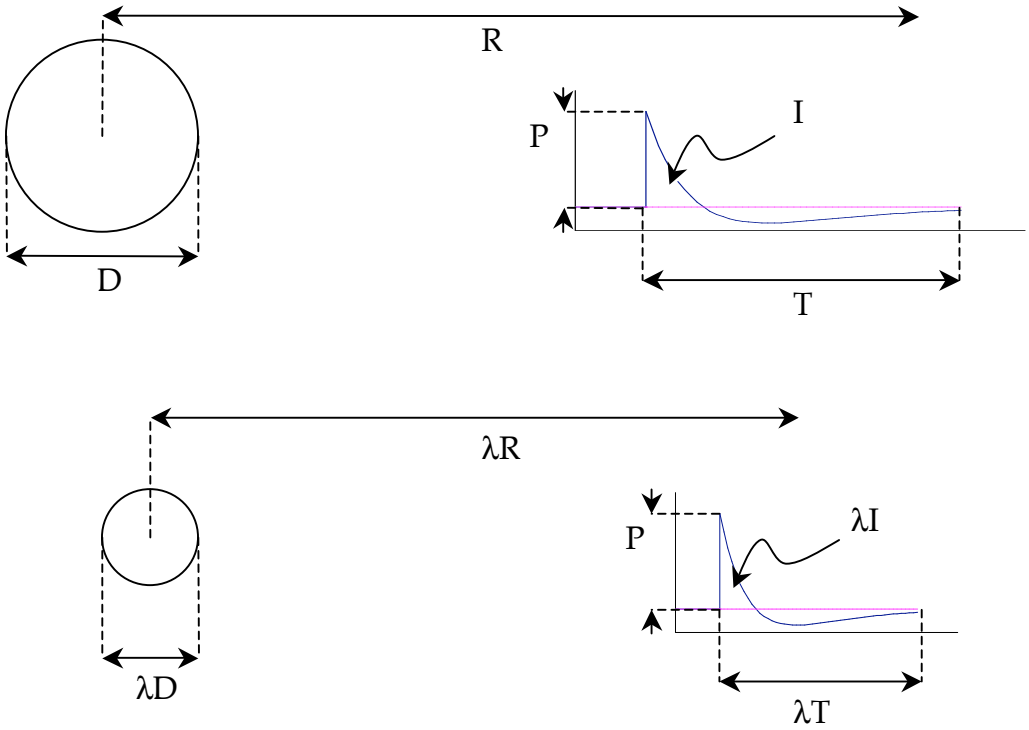

Figure 9 - Hopkinson-Cranz scaling law

Table 2 [53] shows the relationship between the overpressure and its consequences in terms of scaling distance, with explosive weight in Z calculated with TNT equivalent weight.

Table 2 - Overpressure and its consequences in terms of scaling distance

Scaled distance $Z=R/W^{1/3}$ [m/kg$^{1/3}$]	**Overpressure [KPa]**	**Consequences**
900 – 270	7.0e-2 - 2.5e-1	Minimum damage to glass panels
125 – 60	7.0e-1 - 1.5	Typical window glass breakage
60 – 30	1.4 - 2.8	Minimum overpressure for debris and missile damage
24.5 – 12.5	3.5 - 7.6	Windows shattered, plaster cracked, minor damage to some building
13.2 – 9.5	7.6 – 10	Personnel knocked down

13.2 – 8.5	7.6 – 12.5	Panels of sheet metal buckled
13.2 – 7.2	7.6 – 15	Failure of wooden siding for conventional homes
8.4 – 6	12.5 – 20	Failure of walls constructed of concrete blocks or cinder blocks
6 – 4.8	20 – 30	Self-framing paneled buildings collapse, oil storage tanks ruptured
4.2 – 3.3	40 – 60	Reinforced concrete structures severely damaged, railroad cars overturned
2 – 1.35	200 – 500	Lung damage
1.15 – 0.8	700 – 1500	Lethality
0.7 – 0.55	2000 – 3000	Crater formation in average soil

2.5 Blast loads classification

The loads generated on a structure that interferes with a blast wave path will depend on the orientation, geometry and size of this structure. Three main kinds of unconfined explosions can be defined [48] (Figure 10):

- free air burst load. The blast wave propagates away from the center of the explosion striking the structure without intermediate amplification of the initial shock wave;
- air burst load. The explosion is located at a distance away from and above the structure so that ground reflections of initial wave occur before the blast wave reaches the structure;
- surface burst load. The explosion is located close to or on the ground so that the shock wave is amplified at the point of detonation due to ground reflections.

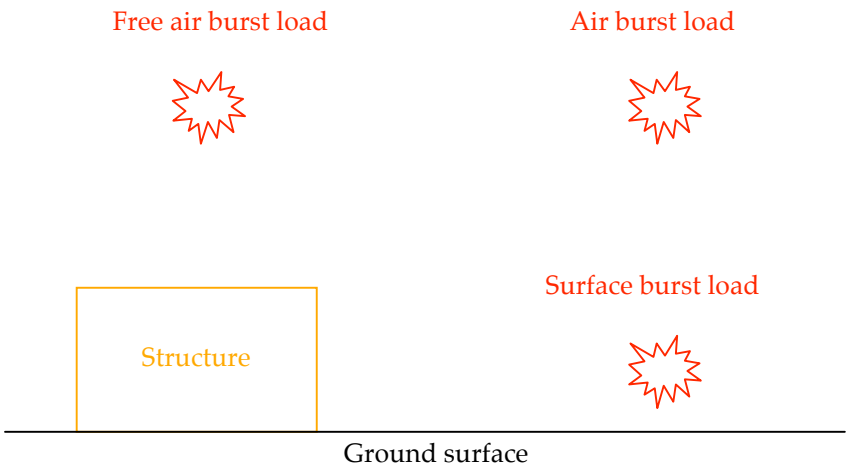

Figure 10 – The three main kind of unconfined explosion

In this thesis the structure response under free air burst load will be analysed

In a free air burst load the shock wave stresses each point of a flat surface with a different angle respect to the direction of wave propagation and the normal surface direction. In case of angle of incidence α different from 90° a reflected pressure is instantly developed on the surface and the pressure is increased to a value in excess of the incident pressure. This reflected pressure will be in function of the incident pressure and angle. The pressure time variation for free air burst and for infinite plane reflectors is shown in Figure 11.

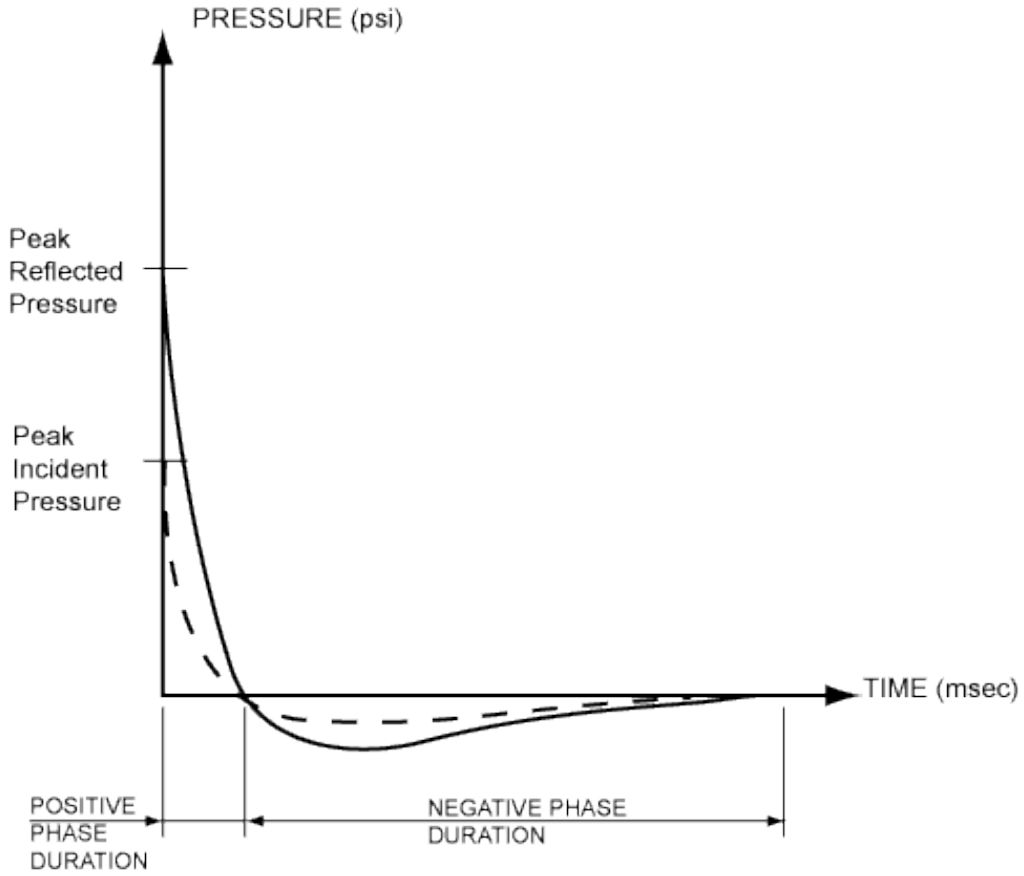

Figure 11 – Pressure-time variation for free air burst [54]

When the shock incidence angle is 0° (path of travel of the wave normal to surface), the point of initial contact sustain the maximum pressure and impulse. The positive phase pressure and impulse patterns on the structure vary with distance from a maximum at this normal distance to a minimum where the plane of the structure is parallel to the shock front. Under this condition, the instantaneous peak value of the reflected overpressure p_r is given by:

$$p_r = 2p + (\gamma + 1)q \qquad (5)$$

where p and q are incident and dynamic pressure respectively and γ is the ratio C_p/C_v relating to the propagation medium (γ=1.4 for air). Dynamic pressure can be expressed through the Rankine-Hugoniot conditions at the shock front by:

$$q = \frac{p^2}{2\gamma p_a + (\gamma - 1)p} \tag{6}$$

that gives:

$$p_r = 2p\frac{7p_a + 4p}{7p_a + p} \tag{7}$$

where P_a is ambient pressure. The variation of the pressure and impulse patterns on the surface between the maximum and minimum values is a function of the angle of incidence α. The effect of the angle of incidence on the peak reflected pressures is shown in Figure 12 [54] which is a plot of the angle of incidence versus the peak reflected pressure coefficient as a function of the peak incident pressure. The peak reflected pressure is $p_{ra}=C_r p_{s0}$. For α=0 the values can be obtained by the equation (7).

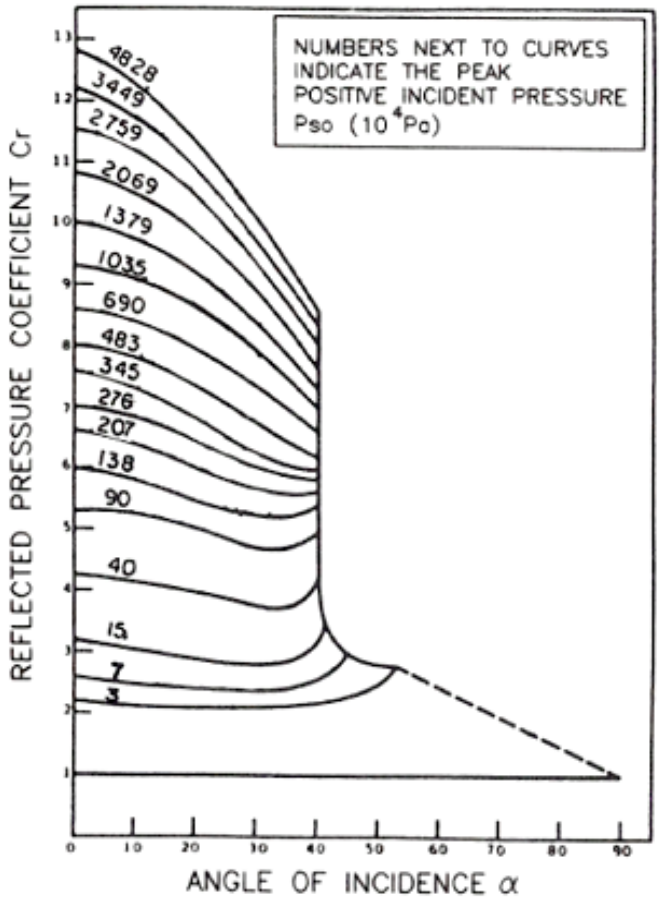

Figure 12 – Reflected pressure coefficient vs. angle of incidence

2.6 Blast loads on composite laminates phenomenology

In general, during blast loading on panels, a compressive stress wave within the material is generated by the pressure wave's impact at the front face of the target. This compressive wave propagates throughout the material until it reaches the target's rear surface, where it is reflected as a tensile wave.

In a composite material laminate, the initial compressive stresses may produce some degree of crushing failure in the composite matrix. The tensile reflected wave starting from the back surface produces an extensive delamination between the last plies of the laminate.

In the following instants, the pressure on the target distributes on the whole material and generates a bending load on the panel, which can also lead to fibre breakage.

This page is intentionally left blank

CHAPTER 3

State of art of blast wave prediction

3.1 Introduction

To ensure structural integrity from explosive blast structural engineers today need guidance on how to design structures to withstands various terrorist acts [1]. The professional skill required to provide blast resistant consulting services include structural dynamics, knowledge of the physical properties of explosive detonations and general knowledge of physical security practices and material behaviour.
The steps commonly followed in this process are:

- determination of the threat;
- development of the design loadings for the determined threat;
- analysis of the behaviour and selection of structural systems.

This chapter will focus on the techniques for reproducing the blast loads that can be used to evaluate the structural response of a new or an existing structure.

3.2 Methods for blast loads prediction

In order to predict the blast effect on structures the following methods are available:

- empirical methods;
- semi-empirical methods;
- numerical methods.

Empirical methods are correlated with analysis of experimental data. Basically most of these techniques are limited by the experimental database. In general, the accuracy of all empirical equations decreases as the scaled distance diminishes.

Semi-empirical methods are based on approximation of theoretical and analytical solutions attempting to describe the physical processes with simplified models. They require an extensive data however their accuracy is generally better than that provided by empirical methods.
Numerical methods are based on mathematical equations that describe the basic laws of physics governing a problem, such as conservation of mass, momentum and energy laws, while the physical behaviours of either structural and fluid materials are described by constitutive relationships. These techniques are implemented in commercial FEM such as LS-DYNA.

3.3 Empirical methods

Results of numerous research and test programs provided a considerable number of analytical methods for predicting blast loading. These analytical procedures are described in several technical manuals and reports.
TM 5-1300 [55] is one of the most widely used manuals for designing protection structures against blast load. The design curves presented in the manual give the blast wave parameters as a function of scaled distance (§2.4) for the three main kind of unconfined explosion: free air burst, air burst and surface burst (Figure 10 - §2.5). In the manual a step-by-step procedure is described for determining blast wave parameters for a surface blast:

- determine the charge weight W, as TNT equivalent, and the stand-off distance R from the charge to the surface of a structure;
- calculate scaled stand-off distance, Z;
- read the blast wave parameters from the manual TM 5-1300 [55] for corresponding scaled stand-off distance, Z.

Another important manual for predicting blast loads is TM5-855-1 that provides procedures for design and analysis of protective structures subjected to the effects of conventional weapons, such as air-blast loads. In the manual closed-form equations are also provided to generate the air-blast pressure time histories. In TM5-855-1 a methodology is also presented to calculate blast load on multi-stored buildings, and the main steps are:

- divide a surface into sub-domain and evaluate a pressure time history and impulse for each small area;

- summing up each impulse in order to obtain the total impulse applied to the surface;
- the total load-time history is then defined to have an exponential form with peak calculated assuming an average peak pressure applied on all the surface.

3.4 CONWEP

In 1984 Kingery and Bulmash [56] developed equations to predict air blast parameters from spherical air burst and from hemispherical surface bursts. In the report data from explosive tests with charge weight from 1 kg to over 400.000 kg are illustrated. The authors curve-fitted these data with high-order polynomial equations. These curves can also be found in TM5-855-1, but only in graphical form.

These equations have been implemented into the computer program CONWEP (CONventional WEaPon) [57]. CONWEP assumes the following exponential decay of the pressure with time:

$$p(t) = p_{s0}\left[1 - \frac{t - T_a}{T_0}\right] e^{\frac{-A(t-T_a)}{T_0}} \qquad (8)$$

where p(t) [kPa] is the pressure at time t, p_{s0} [kPa] is the peak incident pressure, T_0 [ms] is the positive phase duration, A is the decay coefficient (dimensionless) and T_a [ms] is the arrival time. The equation (8) is usually referred to as the Friedlander equation and their parameters can be calculated using the equation found in [56]. CONWEP can be used to simulate free field and reflected conditions generated by a 100 kg hemispherical charge of TNT explosive at the distance of 15 m from the point of detonation. The program also accounts for the angle of incidence of the blast wave (Figure 12).

The results generated with this program have been found generally accurate and for phenomena as dynamic explosions a “generally correct” answer can be the best solution.

The main disadvantages of CONWEP are:

- the pressure curve can be generated from only one point at a time;

- the program doesn't allow structure-fluid interaction/penetration;
- it does not account for shadowing by intervening objects or for confinement effects [58].

3.5 Numerical methods

Numerical methods are based on both mathematical equations that describe the physical behaviour of materials by constitutive relationships and basic laws governing the problem by conservation of mass, momentum and energy equations. These models are called Computational Fluid Dynamic (CFD) models and can be formulated with Finite Element Method which will be briefly described in chapter §4.

Some commercial FEM codes implement also CONWEP program. In particular LS-DYNA uses the CONWEP algorithm through the *LOAD_BLAST card. This card defines an air-blast function for the application of pressure loads due to explosive in conventional weapon [59]. The implementation is based on a report presented in [58], where the authors incorporated the CONWEP blast model into DYNA2D and DYNA3D (that in 1988 became LS-DYNA).

This page is intentionally left blank

CHAPTER 4

Finite Element Method (FEM) applied to blast load phenomenon

4.1 Introduction to the FEM

FEM consists of imaging a structural component to be composed of discrete parts (finite elements) which are then assembled in such a way as to represent the deformation of the structure under load [60]. The first step in FE analysis is called "mesh generation" and it consists of dividing the real structural system (or a skilled simplified real system) up in a finite number of sub-systems of nodes and elements (Figure 13).

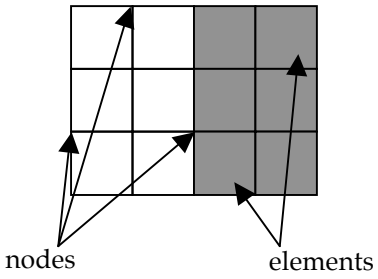

Figure 13 – Nodes and elements (FEM)

Each element has an assigned displacement field and part of the skill of FE modeller is in selecting appropriate elements of the correct size and distribution (FE mesh). In the case of composite materials, various element formulation and material models are available to take into account the laminated form of construction and to represent the anisotropic behaviour.

However, in structural analysis problems the response of a structure under load certainly depends on the intensity of applied load but also on the rate at which the load is applied. In general, the analysis of the response of a deformable body comes under two classes known as wave propagation problems or structural dynamics problems. Wave propagation problems are defined by loading that excites a large number of the structure's highest natural frequency modes. When the load's frequency is similar to the

structure's lowest natural frequency modes and the response is governed by inertia, the problem is called a structural dynamic problem. The first typology of problem concerns the blast wave impact problem.

4.2 Dynamic motion equation

Consider a single degree of freedom (DOF) system such as the one shown in Figure 14 in which a single mass M is subjected to a load R and its motion is acted upon by resistive forces proportional to the mass displacements through the constant K and to the mass velocity through the constant C.
The equation of motion of this system can be expressed as:

$$R = m\ddot{d} + Kd + C\dot{d} \tag{9}$$

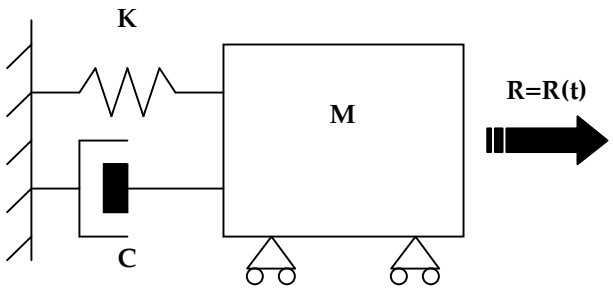

Figure 14 – Single DOF system

where R is the sum of external loads that can vary with time, K and C are the stiffness and the damping coefficients respectively. In a deformable body, R is normally called external load while the spring force Kd is equivalent to internal stiffness forces. The above equation was derived using a single DOF system but it can also be applied to a multi-mass system. In this case the equation becomes:

$$[M]\{\ddot{d}\} + [C]\{\dot{d}\} + [K]\{d\} = \{R^{ext}\} \tag{10}$$

where [M] is the mass matrix, [C] is the damping matrix, [K] is the stiffness matrix, {d} is the nodal displacements and $\{R^{ext}\}$ represents the externally applied loads. The nodal displacements {d} are discrete functions of space but also continuous functions of time. The equation defines a system of coupled, second order, ordinary differential equations in time. In the case of

materials that exhibit non-linear behaviour the stiffness matrix [K] becomes a function of displacement and the dynamic equation of motion is expressed as:

$$[M]\{\ddot{d}\}+[C]\{\dot{d}\}+\{R^{\text{int}}\}=\{R^{ext}\} \qquad (11)$$

where [K]{d} is replaced by $\{R^{int}\}$ that can be used for linear and non-linear materials.

4.3 Implicit and explicit formulations

Dynamic motion equations can be solved in two different ways: modal superposition or direct integration methods [61, 62].

The β-Newmark and the central difference methods are the two main direct integration algorithms. The β-Newmark method calculates the structure displacement history, without changing the form of the dynamic equations neither calculates eigenvalues. It shows better stability and worse accuracy then the central difference method. Direct integration methods are in general particularly useful for non-linear problem solution rather than modal superposition's. In direct integration method the structure's response is calculated at intervals separated by a difference in time Δt. The displacement of the structure is therefore computed at times Δt, 2Δt, 3Δt ... nΔt [63]. When the n_{th} time step is reached, the equation of motion is given by:

$$[M]\{\ddot{d}\}_n+[C]\{\dot{d}\}_n+[K]\{d\}_n=\{R^{ext}\}_n \qquad (12)$$

The β-Newmark algorithm is also called implicit method because it *directly* applies the equation at time t+h after velocity and acceleration equations have been solved. Central difference method is also called explicit method because it considers the equations at time t and combines these equations with finite difference equations to explicitly solve the equation at time t+h.

When a transient load excites only the structure's lowest natural frequencies (structural dynamic problems) then it is possible to use implicit direct integration or modal superposition method to obtain a solution for the response. If the load excites numerous frequencies and the response of the

structure must be analysed for a few multiples of the longest period of vibration (wave propagation problem), explicit direct integration methods are more effective. In explicit methods the displacements at time t+Δt are independent of the acceleration and can be written as:

$$\left\{d\right\}_{n+1} = f\left(\left\{d\right\}_{n}, \left\{\dot{d}\right\}_{n}, \left\{\ddot{d}\right\}_{n}, \left\{d\right\}_{n-1}, \ldots\right) \qquad (13)$$

which uses only historical information consisting of displacements and time derivatives of displacement at time nΔt and earlier to calculate the displacements at time step n+1. Explicit methods are said to be conditionally stable, meaning that there is a critical time step Δt_{cr} that must not be exceeded and therefore the set time-step must often be very small to insure numerical stability. As Δt_{cr} is very small a large number of time steps, which nevertheless are executed very quickly, are needed to complete the calculation. In implicit methods a difference expression is used, that is:

$$\left\{d\right\}_{n+1} = f\left(\left\{d\right\}_{n+1}, \left\{\dot{d}\right\}_{n+1}, \left\{\ddot{d}\right\}_{n+1}, \left\{d\right\}_{n}, \ldots\right) \qquad (14)$$

and therefore the calculation of displacements at time step n+1 requires knowledge of the time derivatives of d_{n+1}, which are unknown and have to be calculated. This is why implicit methods are computationally more costly than explicit methods. Implicit methods are usually unconditionally stable meaning the calculation will remain stable no matter how large the time step size is. Although the time step size can be large in implicit methods a loss in accuracy may occur with extremely large time steps.

In transient analysis implicit methods are best suited to structural dynamics problems. That is if the structural response is dominated by the lower frequency modes or the duration and rise time of the load is a few multiples greater than the time spent by a sound wave to travel through the structure, the implicit method is more efficient. Explicit methods are most effect for wave propagation problems created by impact or blast loading where higher frequency modes must be taken into account. The structure's response usually needs to be analysed over a small time interval.

4.4 Central difference method

The central difference method is a common technique used with explicit integration methods to solve second order differential equations [62]. In the central difference method velocity is expressed as:

$$\left\{\dot{d}\right\}_n = \frac{1}{2\Delta t}\left(\left\{d\right\}_{n+1} - \left\{d\right\}_{n-1}\right) \tag{15}$$

and acceleration as:

$$\left\{\ddot{d}\right\}_n = \frac{1}{\Delta t^2}\left(\left\{d\right\}_{n+1} - 2\left\{d\right\}_n + \left\{d\right\}_{n-1}\right) \tag{16}$$

The above equations are obtained through Taylor series expansions of $\{d\}_{n+1}$ and $\{d\}_{n-1}$ at time $n\Delta t$:

$$\begin{aligned}
\left\{d\right\}_{n+1} &= \left\{d\right\}_n + \Delta t\left\{\dot{d}\right\}_n + \frac{\Delta t^2}{2}\left\{\ddot{d}\right\}_n + \frac{\Delta t^3}{6}\left\{\dddot{d}\right\}_n + \ldots\ldots \\
\left\{d\right\}_{n-1} &= \left\{d\right\}_n + \Delta t\left\{\dot{d}\right\}_n + \frac{\Delta t^2}{2}\left\{\ddot{d}\right\}_n + \frac{\Delta t^3}{6}\left\{\dddot{d}\right\}_n + \ldots\ldots
\end{aligned} \tag{17}$$

$$\left[\frac{1}{\Delta t^2}M + \frac{1}{2\Delta t}C\right]\left\{d\right\}_{n+1} = \left\{R^{ext}\right\}_n - \left[K\right]\left\{d\right\}_n + \frac{1}{\Delta t^2}\left[M\right]\left(2\left\{d\right\}_n - \left\{d\right\}_{n-1}\right) + \frac{1}{2\Delta t}\left[C\right]\left\{d\right\}_{n-1}$$

The equations (17) represent a linear algebraic system. Because the internal and external forces depend only on the loads and stresses at time step n, all the terms on the right hand side of the equations known at the time $n\Delta t$. If the damping and mass matrices are diagonal then the system becomes uncoupled and d_{n+1} solution can be calculated without simultaneously solving any other equation.

4.5 Lagrangian and Eulerian approach

The configuration of a FE model, as well as how properties such as mass, energy and material strength are analysed is the main way of distinguishing between various models. Lagrangian and Eulerian codes are the two basic methods which are both implemented in hydrocodes such as LS-DYNA. In a

Lagrangian approach the mesh is created so that elements' boundaries outline the free surfaces and material boundaries. Hence in this case the local reference system is "attached" to the structure's body and it "follows" the structure's displacements. So the mesh will distort as much as the material will (Figure 15). In a typical Lagrange mesh, coordinates, velocities and forces are related with the corner nodes, while stresses, strains, pressures and energies are associated with the finite elements.

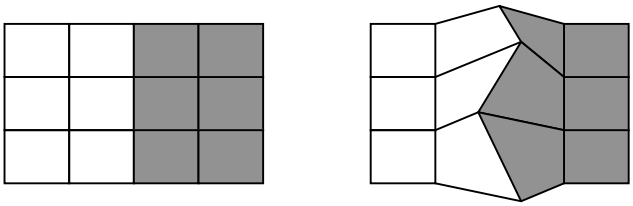

Figure 15 – Example of Lagrangian FE model

The main problems with Lagrange solvers occur when large deformations are involved. Severe distortion of the mesh can result in inaccuracies, negative densities and extremely small time-steps (Figure 16).

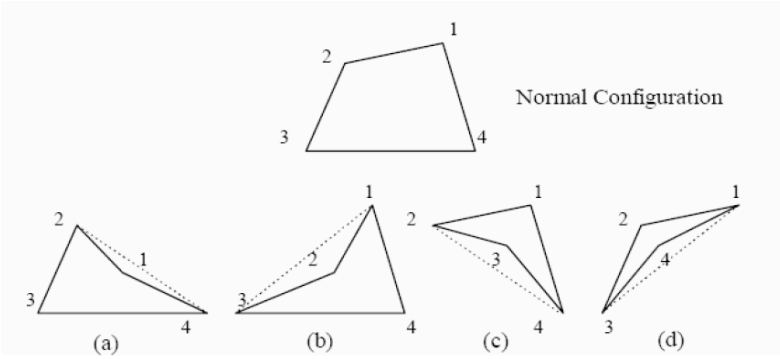

Figure 16 – Example of mesh distortion (a)-(d)

In order to deal with this problem it can be necessary to manually redraw the mesh ("rezoning") or eliminating distorted elements through erosion algorithms. Therefore they are typically not used for models which involve flow or large distortion, although Lagrangian approach is often used in impact models where two solid objects collide, as both target and projectile.

The Eulerian approach differs from Lagrangian approach in a few fundamental concepts. First of all instead of confining the grid to the structural component, Eulerian models place a grid over the space in which the materials can move. As the FE analysis progresses, the component will

move while the mesh remains motionless (Figure 17). Individual nodes and cells basically "observe" as the material modelled flows by. In a typical Euler model, the centers of the cells are used as interpolation points for all variables. In an Eulerian model the material moves through a computational mesh which is fixed in space and each element is allowed to contain a number of different materials. The main problems with Eulerian formulation are the amount of elements that Eulerian model require and their poor handling of geometry. Since you are not only modelling the object of interest, but the space around that object, more elements and therefore more memory and time can be required than a standard Lagrange model. Also since the mesh does not distort with the observed material, it becomes more difficult to track the various components of a part, and therefore observe a single piece evolution. Therefore Eulerian models are typically not used to model solid objects.

The advantage of Euler solvers is that they do not deform and therefore are not subject to the limitations imposed by deformation in Lagrange solvers. They can also allow the mixing of different materials inside the elements. Therefore the shape of material surfaces is not completely limited by element size. They are used when a problem involves high levels of deformation or fluid flow (i.e. gases and liquids), while Lagrangian solvers are normally used to model solids which do not experience such large deformations.

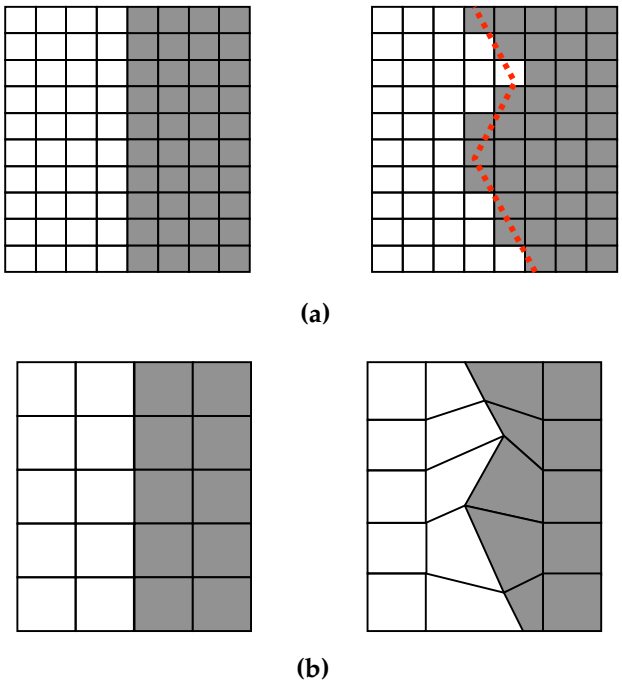

Figure 17 – Example of FE Eulerian model (a) compared with a FE Lagrangian model (b)

4.6 Arbitrary Eulerian-Lagrangian (ALE) model

As we previously said, the Eulerian approach is a popular choice for simulating impact and blast problem as it does not have particular complications with modelling large deformations involved with penetrations or explosions.

The Eulerian method does not have the equivalent of structural elements so if it is used to model fluid-structure interaction it must be coupled with structural elements (CFD models). The coupling is usually done with a Lagrangian based model and the combination is known as Arbitrary-Lagrangian-Eulerian (ALE). There are two main types of ALE algorithms:

- single-material, where each Eulerian element can contain one type of material;
- multi-material, where each Eulerian element is allowed to contain multiple materials (MMALE).

ALE formulations can be considered as algorithms that perform automatic rezoning [64]. It consists of a Lagrangian time step followed by an advection step. The advection step performs an incremental rezone, where incremental refers to the fact that the positions of the nodes are moved only a small fraction of the characteristics lengths of the surrounding elements.

The overall flow of an ALE time step is:

- perform a Lagrangian time step;
- perform an advection step, that is:
  a. decide which nodes to move;
  b. move the boundary nodes;
  c. move the interior nodes;
  d. calculate the transport of the element-centered variables;
  c. calculate the momentum transport and update the velocity.

The ALE algorithms are generally very time expensive and perhaps the simplest strategy for minimizing the cost of the ALE calculations is to perform them only every few time steps. The cost of an advection step is typically two to five times the cost of the Lagrangian time steps.

4.7 Hydrocodes

Hydrocodes such as LS-DYNA make use of a set of equations called equations of state (EOS). An EOS relates the density (or volume) and internal energy (or temperature) of the material with pressure [65] by applying the principles of conservation of mass, momentum and energy. For example, uniform gas would typically be modelled with an EOS based on the Ideal Gas Law. Other functions (constitutive relationships) describe the material behaviour by relating stress and strain, such as strain-rate, work hardening and thermal softening laws. Using these relationships, the FE code advances the calculation forward for a very short period, called time-step, and then performs again the same sequence of calculation. Since the time-step is an important variable, the commercial FE code has an algorithm to determinate this parameter. This subroutine needs many inputs, such as the speed of sound in the material, the FE size mesh and the safety factor, which prevents that the time-step becomes too large [3]. Smaller safety factors result in smaller time-steps and therefore more accurate solutions. However, smaller time-steps will require more calculations to reach the termination time. Therefore in hydrocodes algorithms element size not only determines the complexity of the problem spatially but temporally as well.

A typical order for calculations can be seen in Figure 18.

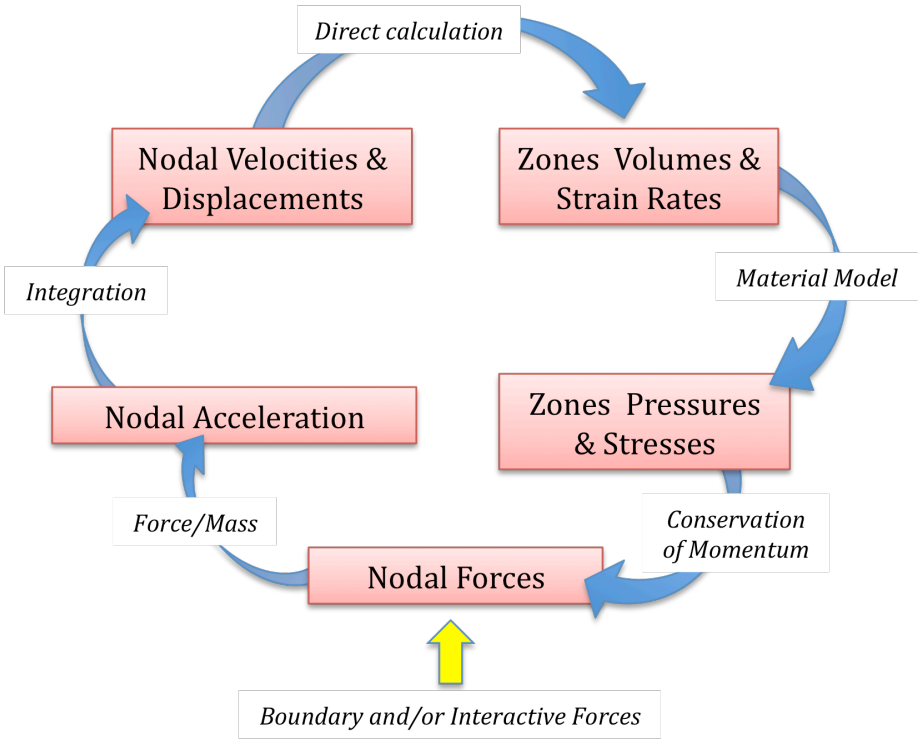

Figure 18 – FEM calculation process [64]

Generally smaller element sizes give more accurate calculations, while larger element sizes sacrifices accuracy for rapidity. Size mesh is not the only factor to consider in mesh generation but, for example, in the case of eulerian model the element's shape plays a role as important as the size.

This page is intentionally left blank

CHAPTER 5

Composite materials experimental data: EUROPA programme tests

5.1 Introduction

The aim of this chapter is to give a general overview of composite materials definitions/classification and to describe some of the experimental tests performed on composite materials during the EUROPA military research programme whose results were kindly provided by QinetiQ [43, 68]. These tests, here briefly illustrated, concern the estimation of mechanical properties of FRP laminates and blast impact tests.

5.2 Definitions and classification of composite materials

A composite can be defined as a mixture of two or more distinct constituents or phases [60] with three principles that have to be satisfied to call a material a composite. These are:

- both constituents have to be present in reasonable proportions;
- the constituent phases should have different properties;
- a synthetic composite should be formed by deliberating mixing and combining the constituents by various means.

The phase that is continuous and is almost always present in the greater percentage in the composite is termed matrix that can be made of ceramic, metallic or polymeric materials. In general, ceramics are strong, stiff and brittle, polymers have low strengths and Young's moduli and metals have intermediate properties with a good ductility. The second component of composite material is known as the reinforcing phase. In most cases the reinforcement is harder, stronger and stiffer than matrix (although there are some exceptions). The geometry of the reinforced material is one the main parameter in determining his effectiveness; in fact the mechanical properties of composite materials are function of the shape and dimensions of the

reinforcement. In Figure 19 it is described a classification scheme for composite materials.

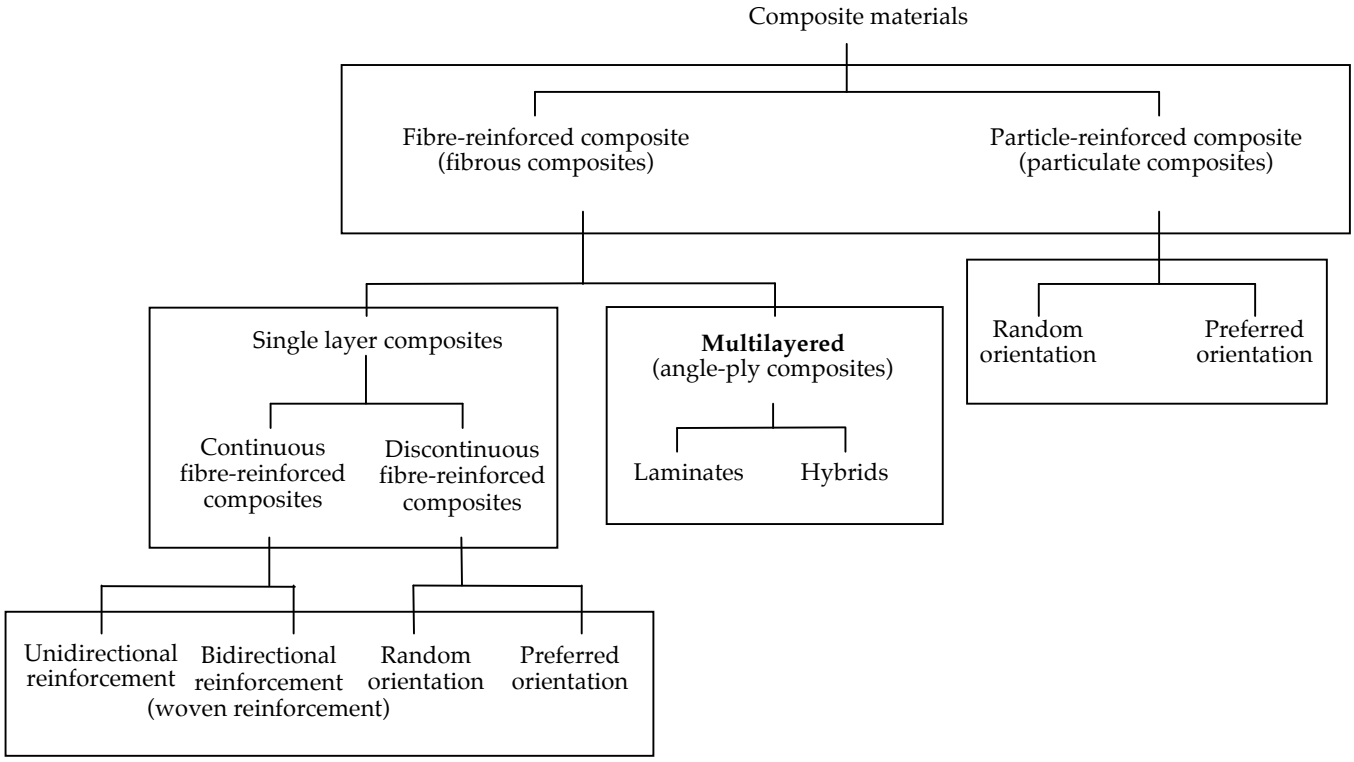

Figure 19 – Classification of composite materials [60]

The blast FEM model performed in this thesis deals with multilayered FRC panels, therefore the following discussion will be particularly focused on this typology of composite. Multilayered FRC are classified as either laminates or hybrids. Laminates are sheet constructions which are made by stacking layers (also called plies or laminate and usually unidirectional) in a specific sequence. The layers are often in the form of "prepreg" (fibres pre-impregnated with partly cured resin), which are consolidated in an autoclave. Hybrids are composites with mixed fibres. The fibres may be mixed within a ply or layer by layer and these composites are designed to benefit from the different properties of the fibres employed. In this thesis, for example, a mixture of glass and carbon fibres incorporated into a polymer matrix will be investigated. Laminates will be typically between 4 and 40 layers, each ply being around 0.125 mm thick if it is carbon or glass fibre/epoxy prepreg. Typical lay-ups are cross-ply, angle ply and quasi-isotropic (Q.I.). When making a laminate, the sequence in which the plies are placed through the thickness (stacking sequence) has to be defined. There is a convention for denoting both lay-up and stacking sequence. Thus, a four-

ply cross-ply laminate which has the ply fibre orientations in the sequence 0°, 90°, 90°, 0° from the upper to the lower surface, would be denoted $(0/90°)_s$. The suffix 's' means that the stacking sequence is symmetric about the mid-thickness of the laminate.

5.3 Mechanical test specimen description

The mechanical properties used to perform the FEM simulation described in the next chapter, regard three different specimens:

- standard High Tensile Strength (HTS) quasi isotropic Non Crimp Fabric (NCF) carbon in an epoxy matrix;
- standard HTC quasi isotropic NCF carbon with 50% fibre weight replaced by NCF E-glass;
- standard HTC quasi isotropic NCF carbon with 50% fibre weight replaced by NCF S2-glass.

Plain tension and compression tests were performed on 8 ply biaxial NCF laminates with a (+/-), (90/0), (+/-), (90/0), (0/90), (-/+), (0/90), (-/+) lay-up and different dimensions. Each panel was C-scanned before the mechanical tests for quality control.

5.4 Mechanical test methods

Laminate mechanical properties were carried out according to British Standard BS EN ISO 527 (3) and 14126 (B2) for plain tension and plain compression respectively.

5.4.1 Plain tension and compression

Both tension and compression tests were performed with a displacement rate of 1 mm/min. In the plain tension test the strain gauges were bonded on both faces of specimens and rosette gauges were used in order to be able to measure Poisson's ratio (Figure 20 a). During plain compression test a compression fixture (Figure 20 b) was used to allow end loading of the specimen. Strain gauges were bonded to both surfaces of the specimen to determine whether buckling occurred during testing. In Figure 21 and Figure 22 some tension and compression failures are illustrated.

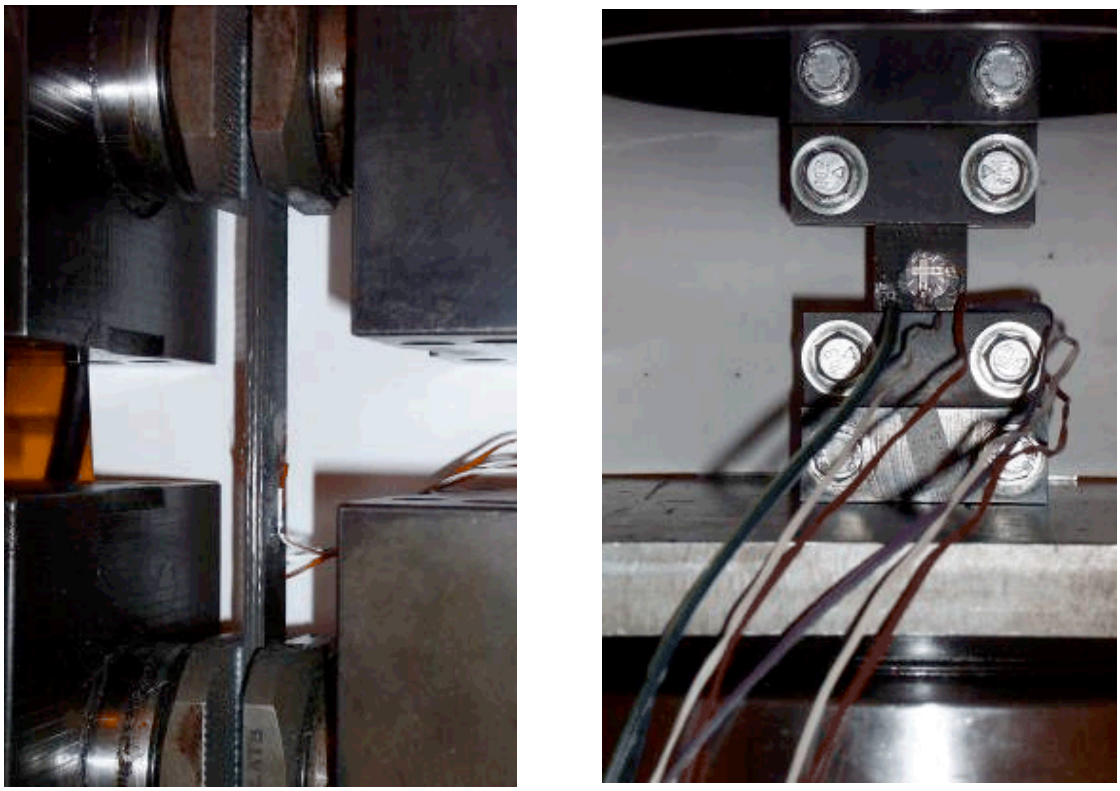

(a) (b)

Figure 20 – Plain tension (a) and compression (a) test set up

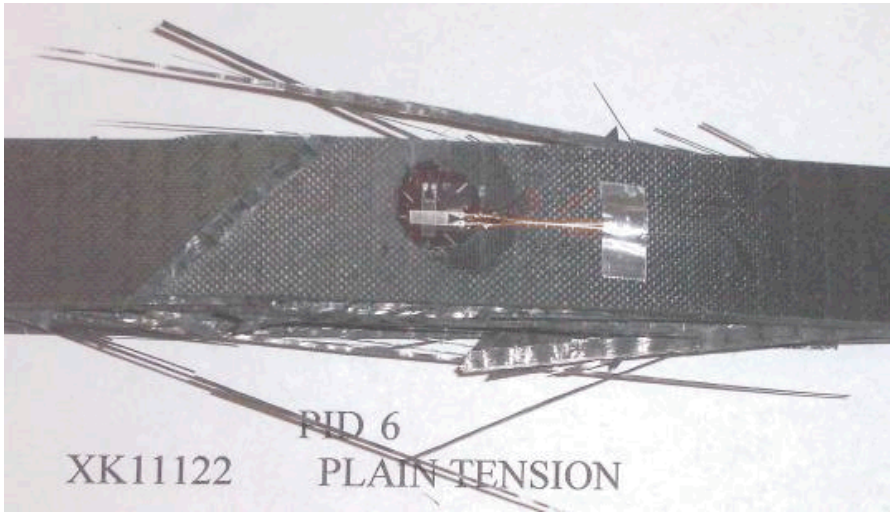

Figure 21 – Typical tensile failure

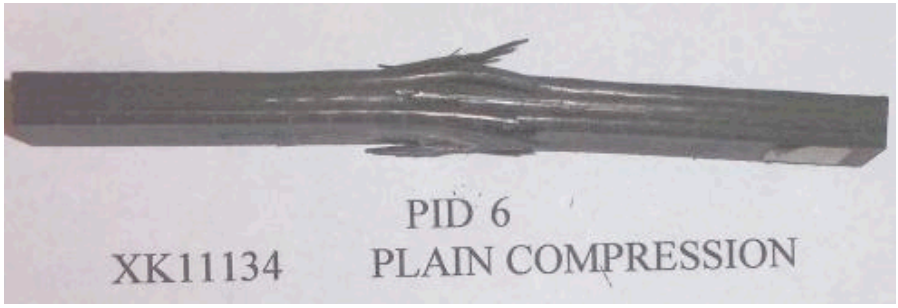

Figure 22 – Typical compressive failure

5.4.2 Mode I interlaminar fracture energy (G_{IC})

In order to perform this test aluminium loading end blocks were bonded to the specimens for pin loading (Figure 23). A 10 μm polytetrafluoroethene (PTFE) film was inserted into the mid-plane to act as a pre-crack for initiation of delamination. The tests were carried out at 2 mm/min, while crack propagation was measured throughout the test using a travelling microscope. Mode I fracture energy tests (G_{IC}) tests were carried out using 6-ply biaxial cross-ply lay-up $[0,90,90,0,90,0]_s$, incorporating the PTFE film at the central 0°/0° interface. This lay-up could not be used effectively for the hybrid laminates due to coupling effects in the unbalanced laminate.

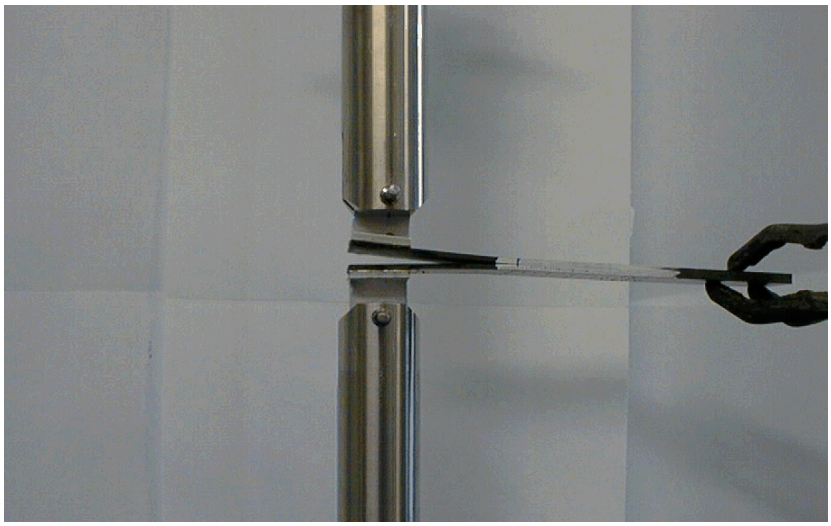

Figure 23 – Mode I interlaminar fracture energy test (G_{IC})

5.4.3 Summary of mechanical test results

Compressive and tensile test results are summarised in Table 3, while the Mode I interlaminar fracture energy test results are illustrated in Figure 24, Figure 25 and Figure 26. In terms of plain compression and tension the hybrid materials showed lower performance than the carbon materials, as expected. The values appear to be consistent with the rule of mixtures for glass and carbon. Nevertheless G_{IC} average value for hybrid specimens is greater than carbon fibre composite.

Table 3 – Mechanical test results

	Compressive			Tensile		
	Strength [MPa]	E [GPa]	υ	Strength [MPa]	E [GPa]	υ
Carbon	-342.8	47.8	0.3	553.6	52.9	0.3
E glass/Carbon	-298.4	28.0	0.4	401.5	28.8	0.3
S2 glass/Carbon	-277.3	34.7	0.3	330.8	32.0	0.3

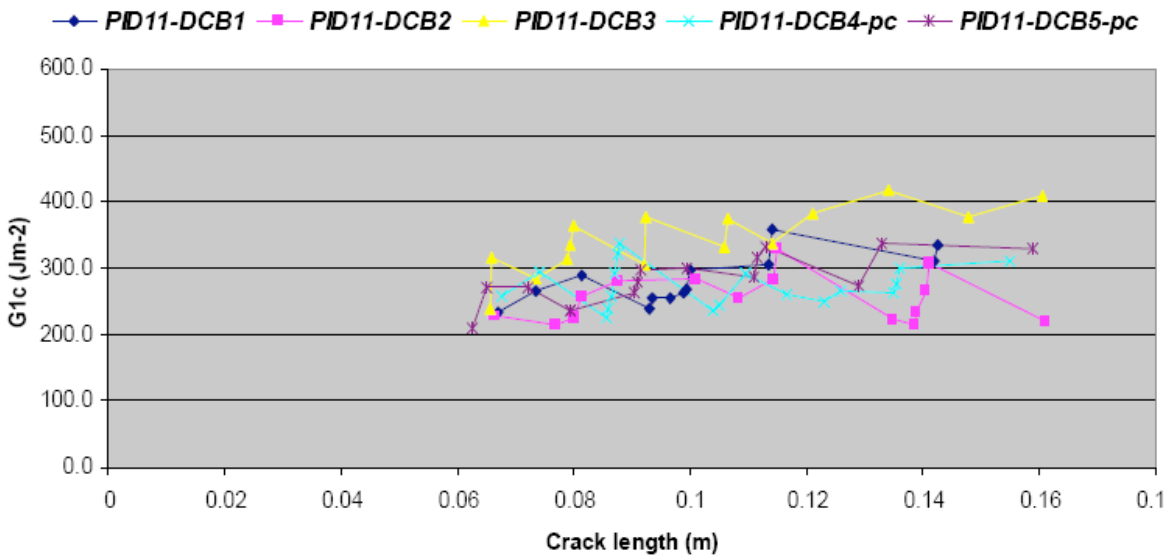

Figure 24 – Carbon G_{IC} results

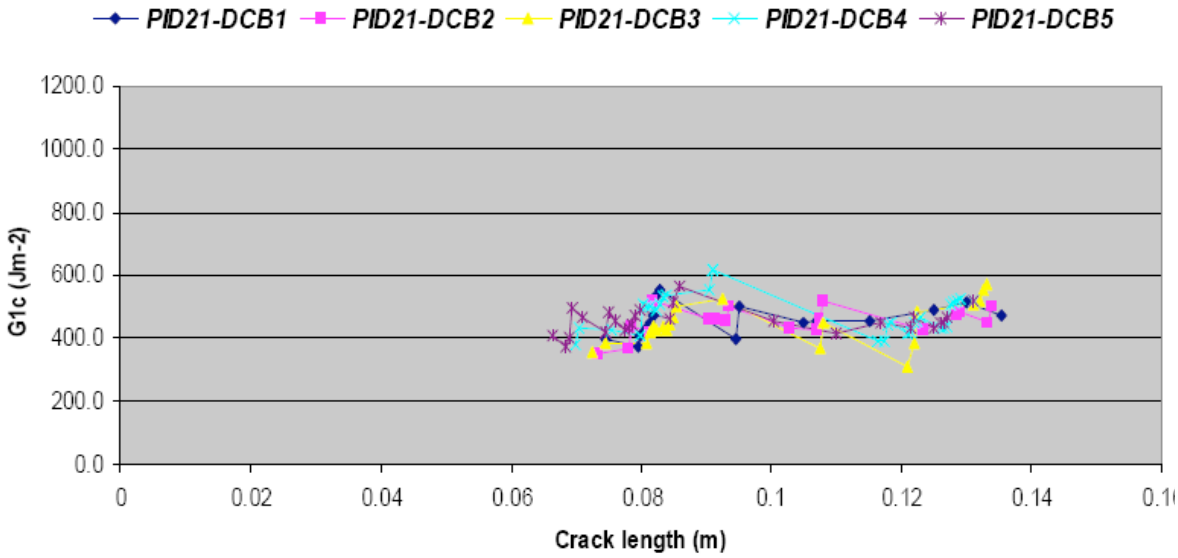

Figure 25 – 100% E glass G_{IC} results

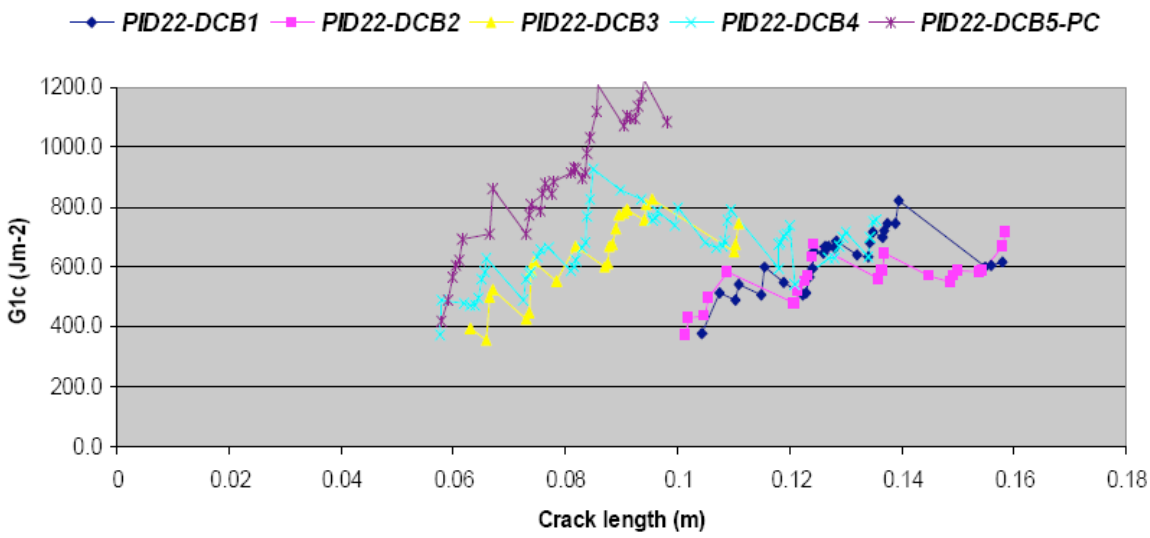

Figure 26 – 100% S2 glass G_{IC} results

5.5 Blast test configuration

The aim of these trials was to assess the response of a range of composite materials under blast load. Small scale (0.10-0.16 m/Kg^3) blast tests were performed with panel performance determined through a combination of panel deformation and estimated damage levels.

A relatively small stand-off distance of 150 mm was applied in order to concentrate the damage in the centre of the target and to reduce boundary influence. The targets were 800 mm by 800 mm square with a thickness of 27 mm. The targets were clamped in position using a purpose built test rig and a spherical explosive charge supported as shown in Figure 27 and Figure 28.

The explosive selected was the C4 (Composition 4) that is a common military plastic explosive. C4 is made up of explosives, plastic binder, plasticizer and, usually, marker or taggant chemicals such as 2,3-dimethyl-2,3-dinitrobutane (DMDNB) to help detect the explosive and identify its source. As with many plastic explosives, the explosive material in C4 is RDX (cyclonite or cyclotrimethylene trinitramine) which makes up around 91% of the C-4 by weight. The plasticizer is diethylhexyl or dioctyl sebacate (5.3%) and the binder usually is polyisobutylene (2.1%) [69].

Figure 27 – Overview of blast test ring

Figure 28 – Overview of blast test charge set up

A break wire was positioned at the base of the C4 explosive charge to provide a datum point for subsequent timing measurement. An ionization sensor was located on the surface of the target to provide time-of-arrival data for blast model validation. Aluminium honeycomb crush blocks were used to record the deformation of the target. Passive and active crush blocks were used and positioned at the quarter span point of the target, to measure peak and timed panel deflection. The active crush block contained three contact switches, allowing the initial dynamic response of the panel to be recorded for comparison with modelling results.

5.6 Blast test composite materials and charge sizes

During the EUROPA programme blast tests were performed on different kind of composite panels. In this thesis FE models will be modelled and compared with the EUROPA experimental results for the following three composite materials:

- Standard Carbon: Tenax STS 24k NCF quasi isotropic in standard epoxy matrix $(+-45/90,0)7_s$;
- E Glass / Carbon Hybrid: E Glass / STS 24k with alternating plies in balanced lay-up $(E+-45/C90,0/C+-45/E90,0)_s$;
- S2 Glass / Carbon Hybrid: S2 Glass / STS 24k with alternating plies in balanced lay-up $(S2+-45/C90,0/C+-45/S290,0)_s$.

The range of C4 charge size applied in the models is between 675 and 870 g.

5.7 Summary of blast test results

In Figure 29 the blast test results are summarised. The tests were conducted at same stend-off distance but at C-4 different charge size, varying from 600g to 900g.

The S2 Glass / Carbon Hybrid laminates exhibited the greatest resistance to blast loading, with a successful test at 825 g C4. Somewhat surprisingly, the E Glass / Carbon Hybrid displayed a very low level of blast resistance, with gross material failure under loading by 750 g C4. In Figure 30 and 31 the post-blast panel condition for the 100% Carbon target are illustrated. The specimens were also sectioned in order to inspect through-thickness damage at the centre of the target (Figure 32 and Figure 33).

Material	charge weight										
	600	675	750	788	825	863	900	975	1200	1275	1500
100% CFRP	✓		✓ ✓		✗		✗				
Carbon / E Glass Hybrid		✓	✗ ✗			✗					
Carbon / S2 Glass Hybrid			✓		✓ ✓	✗	✓ ✗ ✗				

✓ passed test ✗ failed test

Figure 29 – Summary of blast test results

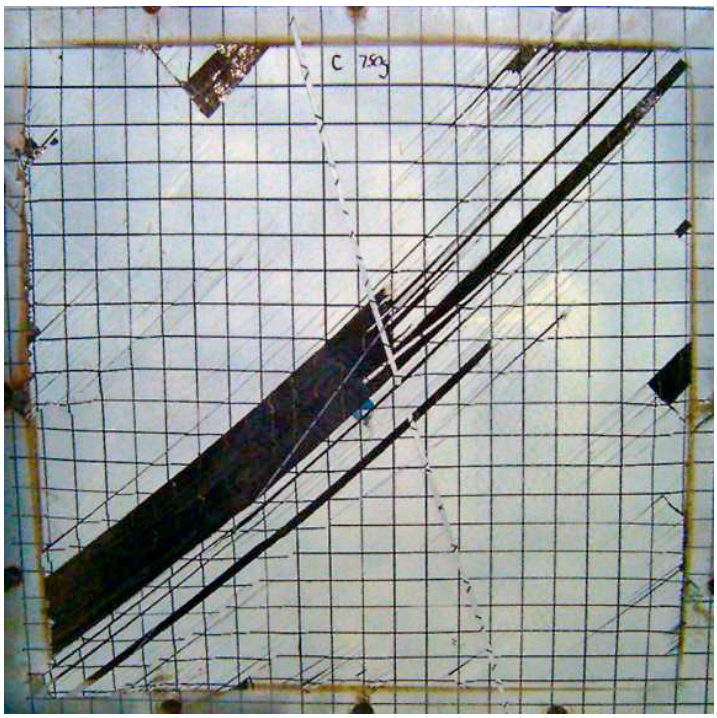

Figure 30 – Rear face condition after blast impact (100% CFRP 750 g C4 at 150 mm)

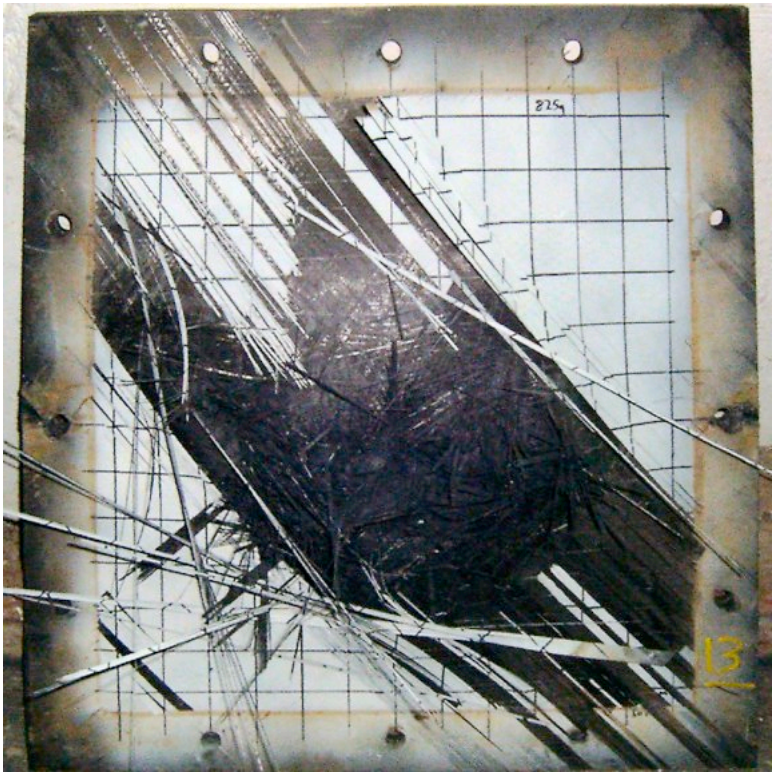

Figure 31 – Rear face condition after blast impact (100% CFRP 825 g C4 at 150 mm)

Figure 32 – Delamination damages in 100% Carbon plate loaded by 750 g C4 at 150 mm

Figure 33 – Delamination damages in S2 / Carbon plate loaded by 750 g C4 at 150 mm

For all the panel under assessment, widespread delamination was observed, with the most extensive delamination (in terms of area affected) occurring midway through the thickness. This is largely to be expected, since the mid-plane of the panel corresponds to the neutral axis under bending subjected to the highest shear stress. Close examination of damage (Figure 34) through the thickness of the panels indicates that 0/90 interfaces between carbon plies are the most susceptible to delamination. This is most likely due to a large mismatch in directional in-plane properties between adjacent plies.

100% CFRP

E glass / Carbon

S2 glass / Carbon

Figure 34 – Details of delamination damage (750 g C4 at 150 mm)

During the tests on a number of hybrid panels, it was observed that bundled glass laminates are largely intact. This can be explained by the difference in fracture energy between carbon and glass reinforced laminates, as observed during mechanical testing (Figure 24, Figure 25 and Figure 26). The interlaminar fracture energy for a carbon-reinforced panel was roughly three-quarter of that for an equivalent glass-reinforced panel.

5.8 Experimental damage assessment

As it can be noted in Figure 31, where a failed blast test is shown (Figure 29), the damage does not correspond to a hole in the target. In order to assess the damage in the laminates a reservoir of water was placed on top (rear) surface of the plates (Figure 35). If water passed through the target's thickness, the sample was considered failed.

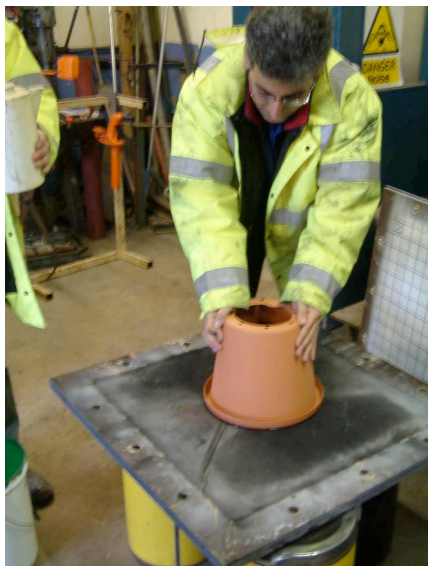

Figure 35 – Reservoir of water placed on top surface

This page is intentionally left blank

CHAPTER 6

FEM models

6.1 Introduction

The aim of this chapter is to illustrate the FEM model characteristics, in terms of material and finite elements formulations, used to simulate the blast impact on the armoured structures with the commercial FEM code LS-DYNA (Version LS971s R2 – revision 7600.1116). Because of difficulties related with the direct measurement of blast effect at the target, in order to assess the numerical model capability, the simulations have been carried out first on steel rolled homogenous armours (RHA) that is a relatively better understood and "easier" to model its material behaviour.

On the metallic target two approaches were used to simulate the blast load: simply Lagrangian model with CONWEP load function and ALE model. Because of modelling approach used for the composite panel, only ALE formulation was found applicable in the case of composite armours.

6.2 FE model general properties

The model was generated with the ANSYS pre-processor and through the ANSYS pre-processor was created the LS-DYNA input file (*name*.k file). The LS-DYNA cards, like materials and contacts cards, were manually addend into the LS-DYNA input file generated with ANSYS. The ANSYS pre-processor was only used to input geometry, mesh and boundary conditions. The FE analysis were performed with the Windows XP Pro SP2 B2600 operating system and the Fortran Intel Compiler 9.1. Single precision (I4R4) and 300Mb of memory were used for the numerical calculations.

The FE model was made of three components: frame, bolts and target (Figure 36) and, by using symmetry properties, only one quarter of the real configuration was modelled. Fixed boundary conditions were applied on the lower frame's surface in order to simulate the rest of the basement (Figure 27) and symmetry boundary conditions were applied on the nodes lying on plane XZ and YZ (Figure 37). The contacts between target and bolts and

between target and frame were modelled through the *CONTACT AUTOMATIC NODES TO SURFACE / SURFACE TO SURFACE cards for shell and solid elements respectively. Besides, the bolts and frame's confining nodes were merged; hence no contact card was applied between these components (Figure 38).

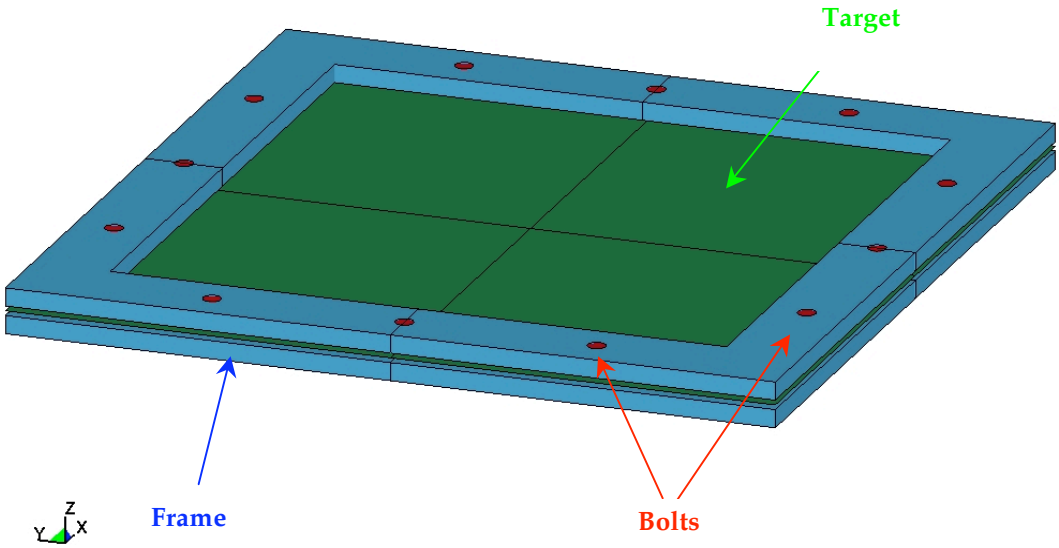

Figure 36 – Metallic FEM model

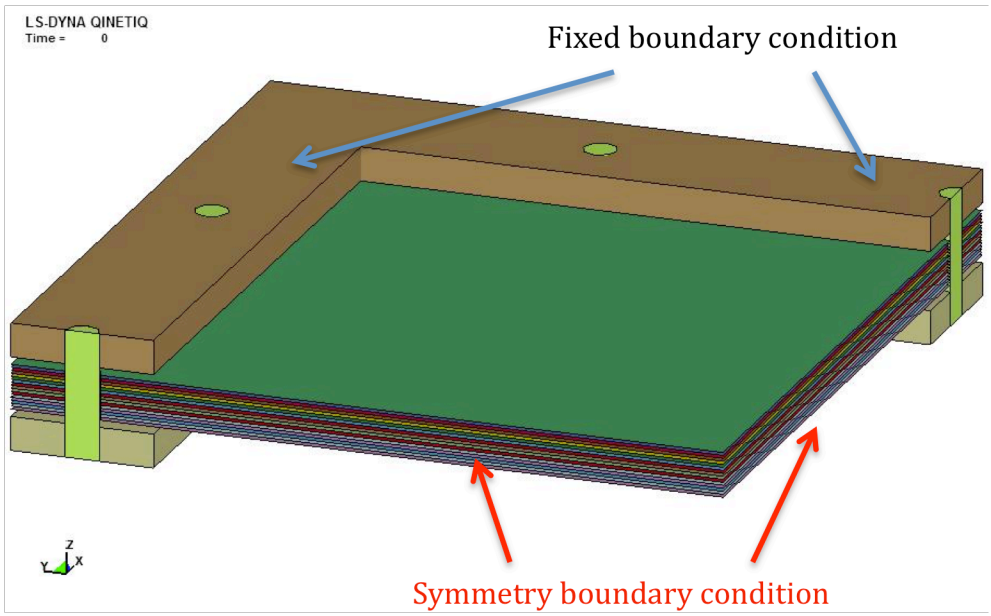

Figure 37 – Boundary conditions

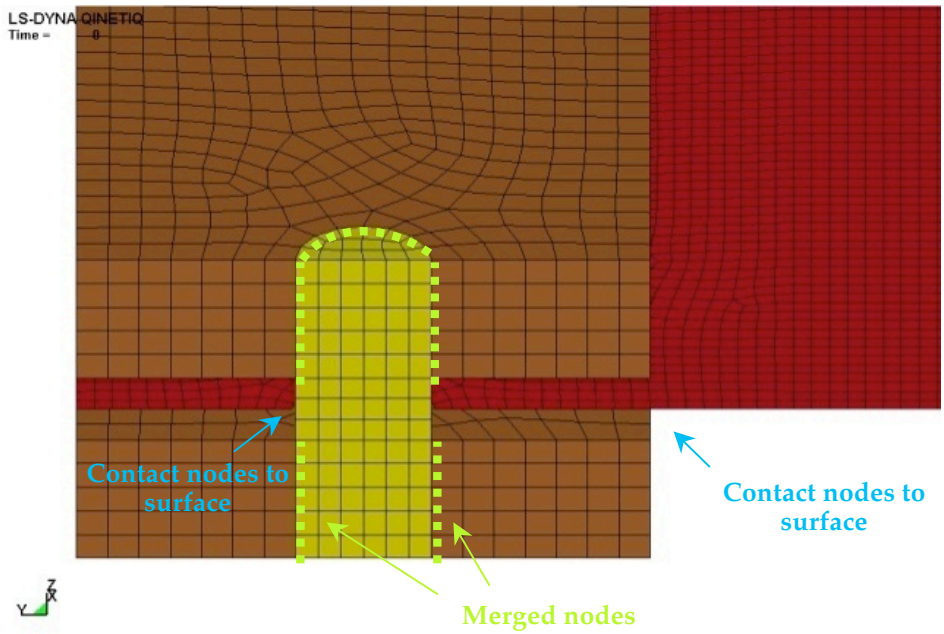

Figure 38 – Contact definitions

The accuracy of the model was verified on the basis of a similar numerical analysis found in literature [43]. This study shows that in the case of a 2D axisymmetric model as the mesh size is refined the expected convergence is not reached. Hence it is difficult to choose the most appropriate mesh size for this kind of application and for that reason in this thesis the mesh size was selected on the basis of a balance between accuracy and efficiency.

The numerical simulations were validated with SAFESA method [70]. SAFESA was a project that generated a framework for assessing structures behaviour using FE calculations, helping to minimize error and also allowing to found and to manage errors.

Moreover, it is important to underline that at the moment there are few works where the ALE approach is applied to simulate blast phenomenon, hence a benchmark for this kind of models was not possible.

6.3 Steel target model

The metallic plate was 800 by 800 mm square with different target thicknesses. The RHA blast tests had the same configuration illustrated in the previous chapter for the composite target (§5.5) with different C4 charge sizes at constant 150 mm stand-off distance.

The following thickness/charge combinations have been modelled:

- 5 mm/750 g (scaled distance Z=0.16);

- 6 mm/750 g (Z=0.16);
- 8.9 mm/1800 g (Z=0.12).

6.3.1 Steel model configuration

Both shell and solid finite elements were used to mesh the metallic target with target mesh size varying from 2.4 to 4.4 mm (Figure 39, Figure 40 and Figure 41).

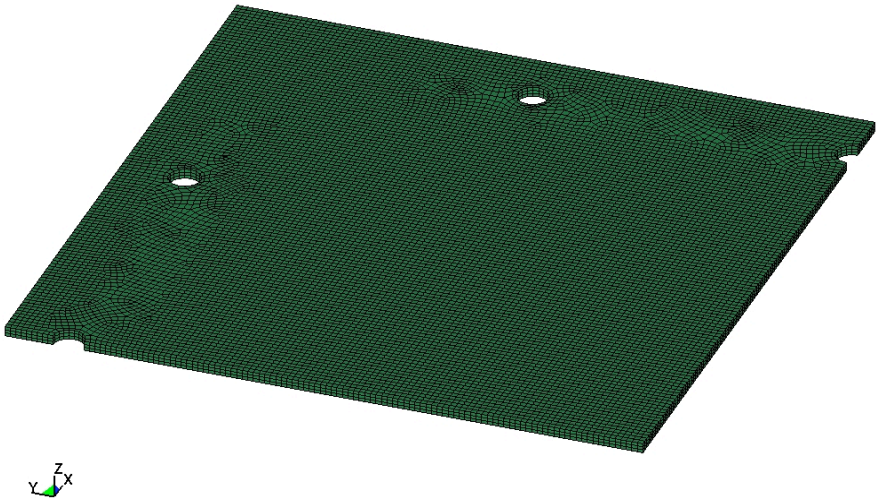

Figure 39 – Metallic target solid element model (mesh size=3.5 mm)

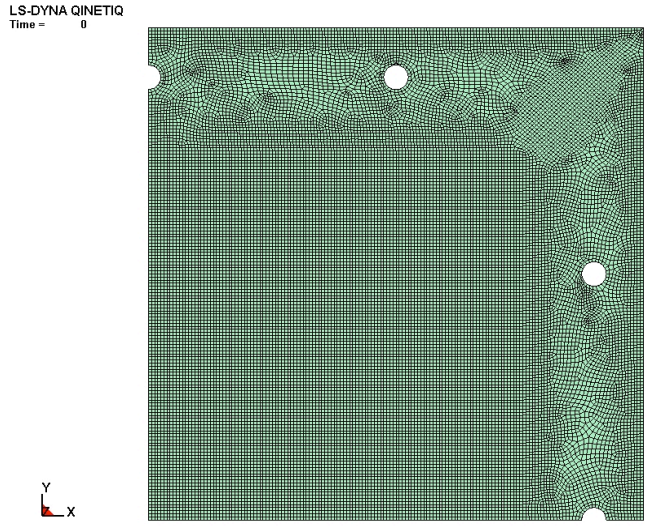

Figure 40 – Metallic target shell element model (mesh size=2.5 mm)

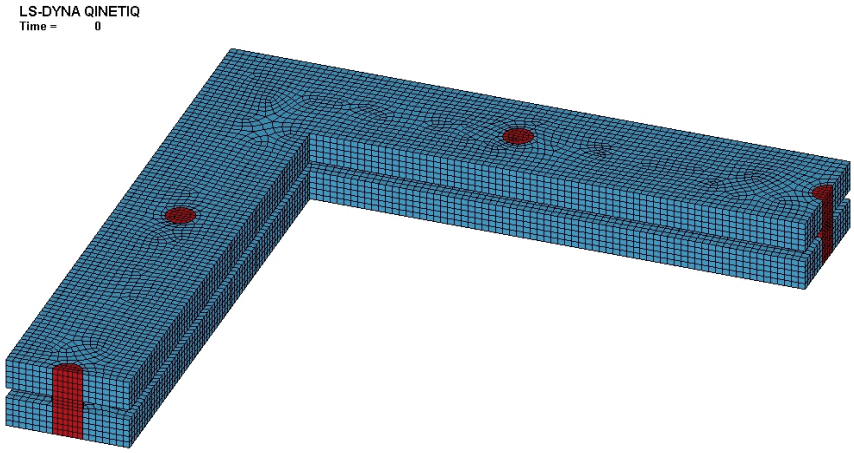

Figure 41 – Frame and bolts (mesh size=4 mm)

The total number of elements for target, bolts and frame varies from about 80.000 to 125.000 according to mesh size and type of element (shell or solid). Under-integrated Hughes-Liu (type 1) [71, 72] and fully integrated selective reduced formulations (type 2) were applied respectively to shell and solid elements.

6.3.2 Steel material model

The RHA target was modelled with Johnson-Cook (J-C) material model [73] that is implemented in LS-DYNA with *MAT_015 card.

J-C constitutive equation can be represented by the following:

$$\sigma_y = (A + B\varepsilon^n)\left(1 + C\ln\left(\frac{\dot{\varepsilon}}{\dot{\varepsilon}_0}\right)\right)\left(1 - \left(\frac{T - T_{room}}{T_m - T_{room}}\right)^m\right) \tag{18}$$

where ε is the effective plastic strain, $\dot{\varepsilon}$ is the total strain rate, $\dot{\varepsilon}_0$ is the reference plastic strain rate, T is the temperature of the work material, T_m is the melting temperature of the work material and T_{room} is the room temperature. Coefficient A is the strain hardening constant, B is the strain hardening coefficient, C is the strain rate coefficient, n is the strain hardening exponent and m is the thermal softening exponent.

The strain at fracture is given by:

$$\varepsilon^f = \left[D_1 + D_2 e^{D_3\sigma^*}\right]\left[1 + D_4 \ln\dot{\varepsilon}^*\right]\left[1 + D_5\left(\frac{T - T_{room}}{T_m - T_{room}}\right)\right] \tag{19}$$

here σ^* is the ratio of pressure divided by effective stress ($\sigma^*=p/\sigma_{eff}$) and $\dot{\varepsilon}^*$ is the ratio of effective total strain rate normalized by reference plastic strain rate. Fracture occurs when the damage parameter $D=\sum\frac{\Delta\varepsilon}{\varepsilon^f}$ reaches the value of 1. In the case of solid elements J-C LS-DYNA model requires an equation of state (EOS). In this case the Gruneisen equation was chosen that defines the pressure for compressed materials as:

$$p=\frac{\rho_0 C^2\mu\left[1+\left(1-\frac{\gamma_0}{2}\right)\mu-\frac{\alpha}{2}\mu^2\right]}{\left[1-\left(S_1-1\right)\mu-S_2\frac{\mu^2}{\mu+1}-S_3\frac{\mu^3}{\left(\mu+1\right)^2}\right]^2}+\left(\gamma_0+\alpha\mu\right)E \tag{20}$$

and for expanded materials as:

$$p=\rho_0 C^2\mu+\left(\gamma_0+\alpha\mu\right)E \tag{21}$$

where C is the intercept of the v_s-v_p curve; S_1, S_2 and S_3 are the coefficients of the slope of v_s-v_p curve; γ_0 is the Gruneisen gamma; α is the first order volume correction to γ_0, E is the internal energy per unit volume and $\mu=\rho/(\rho_0-1)$. The values for Johnson-Cook material model and Gruneisen EOS are shown in Table 4.

Table 4 – Johnson-Cook and Gruneisen EOS parameters for steel RHA [43]

***MAT_015**			
Density [kgm^{-3}]	7850	**T_m [K]**	1793
Young's Modulus, E [GPa]	210	**T_{room} [K]**	300
Shear Modulus, G [GPa]	81.8	**Reference Plastic Strain Rate [s^{-1}]**	0.001
Poisson's Ratio	0.3	**Specific Heat [J/kgK]**	452
Strain Hardening Constant, A [GPa]	0.79	**Failure parameter D_1**	0.05

Strain Hardening Coefficient, B [GPa]	0.51	**Failure parameter D_2**	3.44
Strain Rate Coefficient, C	0.014	**Failure parameter D_3**	-2.12
Strain Hardening Exponent, n	0.26	**Failure parameter D_4**	0.002
Thermal Softening Exponent, m	1.13	**Failure parameter D_5**	0.61
***EOS_GRUNEISEN**			
C [m/s]	4569	S_3	0
S_1	1.49	γ_0	2.17
S_2	0	A	0

6.4 Composite target model

The characteristics of composite material targets are illustrated in §5.5 and §5.6. In order to model hybrid composite material plates, multi-layers shell elements with interface delamination model was chosen. The same approach was also used for the non-hybrid CFRP panel.

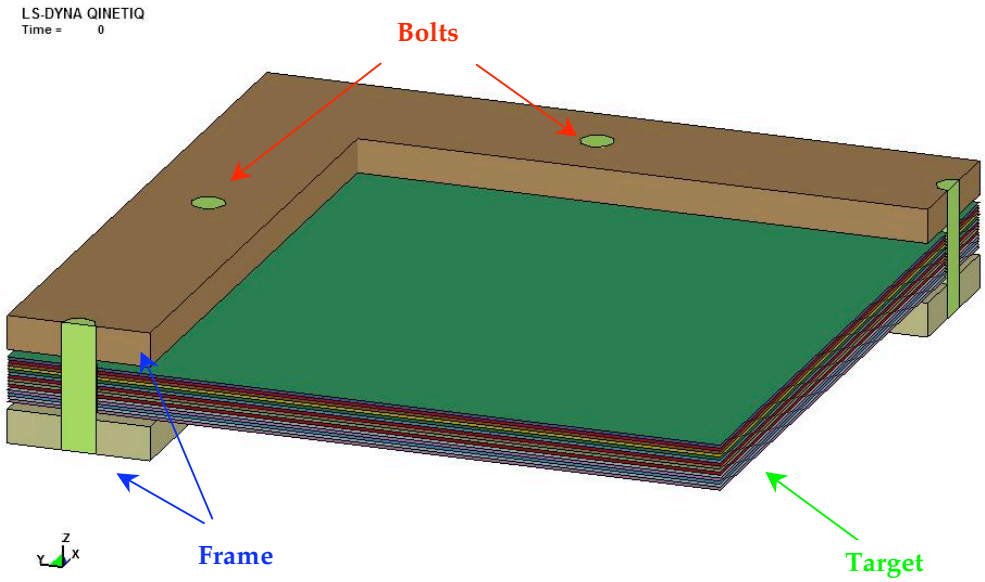

Figure 42 – Composite FEM model

In the case of hybrid panel, all the 16 layers were modelled (layer thickness=1.6875 mm) that really make the hybrid panel $(G+-45/C90,0/C+-45/G90,0)_s$ (Figure 43a). Nevertheless in the case of non-hybrid carbon fibre panel, only 14 layers were modelled (layer thickness=1.928 mm) instead of the 56 layers that really make the panel, in order to avoid too many elements

(Figure 43b). Hence, in this case, 1 layer is made of 4 integration points and each of them is associated to a different layer (+-45/90,0). In this way, for CFRP model 1 shell layer represents 4 real plies (4 integration points). This simplification was possible because CFRP is a no-hybrid material.

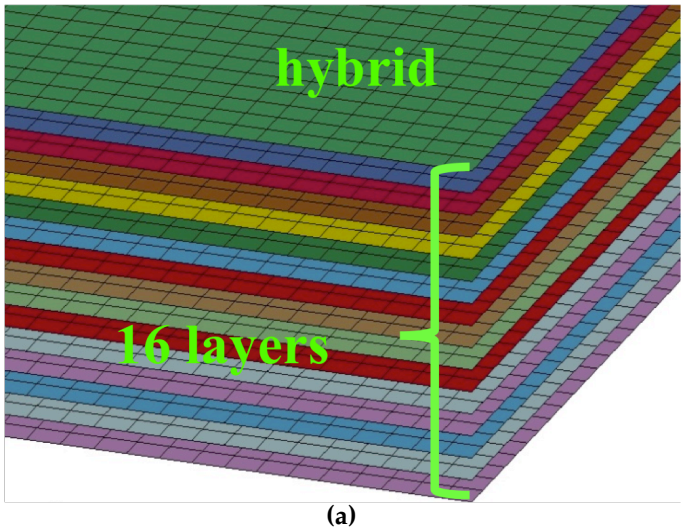

(a)

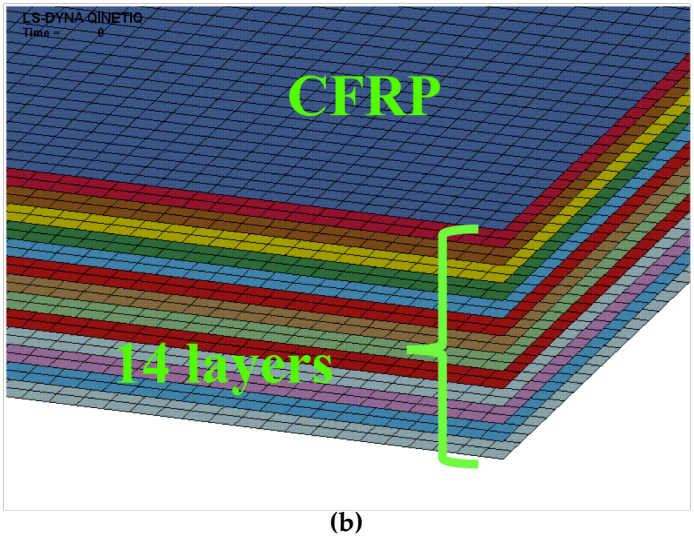

(b)

Figure 43 – Hybrid (a) and CFRP non-hybrid (b) multi-layers composite models

The following composite / C-4 charge size combinations were modelled (Figure 44):

- Standard Carbon (CFRP) no-Hybrid: 750 g and 870 g;
- E glass / Carbon Hybrid: 675 g and 750 g;
- S2 glass / Carbon Hybrid: 750 g and 870 g;

Material	charge weight										
	600	675	750	788	825	863	900	975	1200	1275	1500
100% CFRP	✓		✓ ✓		✗		✗				
Carbon / E Glass Hybrid		✓	✗ ✗			✗					
Carbon / S2 Glass Hybrid			✓		✓ ✓	✗	✓ ✗ ✗				

✓ passed test
✗ failed test
FEM simulation performed

Figure 44 – FEM simulations

6.4.1 Composite model configuration

The total number of elements for the composite model is about 169.000 with a size mesh of about 2.6 mm.

Belytschko-Tsay under-integrated formulation (type 2) was applied to composite shell elements. In this case hourglass viscous form control (type 1) was applied to under-integrated shell elements with an hourglass coefficient of $1e^{-3}$.

Hourglass modes are non-physical, zero-energy modes of deformation that produce zero strain and no stress. These modes occur only in under-integrated solid, shell and thick shell elements and LS-DYNA has various algorithms for inhibiting hourglass modes. For high velocity impacts, viscosity-based HG control (types 1,2,3) is recommended even for solid/structural parts [74].

6.4.2 Composite material model and failure criteria

The composite material behaviour was modelled with *MAT_54 (ENHANCED_COMPOSITE_DAMAGE) implemented in LS-DYNA FEM code and valid only for shell element formulation [59]. This card is the enhanced version of *MAT_22 and it models arbitrary orthotropic materials such as unidirectional layers in composite material shell structures. Optionally various types of failure can be specified following either the suggestions of Chang and Chang [67] or Tsai and Wu [75].

Generally failure criteria predict the first occurrence of failure in one of the laminate but are unable to track failure propagation until complete laminate failure. To analyse the track damage up to laminate failure, continuum damage mechanics is necessary. There are many composite failure criteria and their success in predicting failure often being confined to one fibre/resin combination subjected to a well defined set of stresses.

One of these criteria is the Chang and Chang failure criterion, which was chosen in this work. Besides, in this thesis for all shell elements laminated shell theory was activated to properly model the transverse shear deformation.

Chang and Chang criterion is given as follows [64]:

tensile fibre mode

$$\sigma_{11} > 0 \quad then \quad e_f^2 = \left(\frac{\sigma_{11}}{X_t}\right)^2 + \beta\left(\frac{\sigma_{12}}{S_c}\right) - 1 \begin{cases} \geq 0 & failed \\ < 0 & elastic \end{cases} \tag{22}$$

$$E_1 = E_2 = G_{12} = \upsilon_{21} = \upsilon_{12} = 0$$

compressive fibre mode

$$\sigma_{11} < 0 \quad then \quad e_c^2 = \left(\frac{\sigma_{11}}{X_c}\right)^2 - 1 \begin{cases} \geq 0 & failed \\ < 0 & elastic \end{cases} \tag{23}$$

$$E_1 = \upsilon_{21} = \upsilon_{12} = 0$$

tensile matrix mode

$$\sigma_{22} > 0 \quad then \quad e_m^2 = \left(\frac{\sigma_{22}}{Y_t}\right)^2 + \left(\frac{\sigma_{12}}{S_c}\right)^2 - 1 \begin{cases} \geq 0 & failed \\ < 0 & elastic \end{cases} \tag{24}$$

$$E_2 = \upsilon_{21} = 0 \rightarrow G_{12} = 0$$

compressive matrix mode

$$\sigma_{22} < 0 \quad then \quad e_d^2 = \left(\frac{\sigma_{22}}{2S_c}\right)^2 + \left[\left(\frac{Y_c}{2S_c}\right)^2 - 1\right]\frac{\sigma_{22}}{Y_c} + \left(\frac{\sigma_{12}}{S_c}\right)^2 - 1 \begin{cases} \geq 0 & failed \\ < 0 & elastic \end{cases} \tag{25}$$

$$E_2 = \upsilon_{21} = \upsilon_{21} = 0 \rightarrow G_{12} = 0$$

where:

- e_f represents the tensile fibre mode
- e_c represents the compressive fibre mode
- e_m represents the tensile matrix mode
- e_d represents the compressive matrix mode
- E_1 is the Young's modulus – longitudinal direction;
- E_2 is the Young's modulus – transverse direction;
- υ_{21} is the Poisson's ratio 21;
- G_{12} is the Shear modulus 12;
- X_C is the longitudinal compressive strength;
- X_T is the longitudinal tensile strength;
- Y_C is the transverse compressive strength, 2-axis;
- Y_T is the transverse tensile strength, 2-axis;
- S_C is the shear strength, 12 plane;
- β is the weighting factor for shear term in tensile fibre mode ($0 \leq \beta \leq 1$).

For $\beta=0$ in equation (22) we get the maximum stress criterion. In the case of hybrid panel, 3 integration points have been assigned to 1 unidirectional shell layer in order to have a more precise solution (3 integration points for 1 real composite ply). On the other hand, for the no-hybrid CFRP panels 4 integration points were assigned for each layer, although in this case each integration point represents only 1 real unidirectional ply (§6.4).
Besides, further parameters can be defined in order to define different failure modes. These parameters are:

- DFAILT: maximum strain for fibre tension (DFAILT=1 => 100% strain);
- DFAILC: maximum strain for fibre compression (DFAILC=-1 => 100% strain);
- DFAILM: maximum strain for matrix straining in tension or compression;
- DFAILS: maximum shear strain;
- EFS: effective failure strain;
- TFAIL: time step size criterion for element deletion.

In *MAT_54 the failure can occur in four different way and only when the element has occurred in all the composite layers (through-thickness integration points) the element is deleted. These failure criteria are:

- if DFAILT is zero (in this case also DFAILC must be zero), failure occurs if the Chang-Chang failure criteria are satisfied in the tensile fibre mode (22) or in compressive fibre mode (23);
- if DFAILT is greater than zero (in this case also DFAILC must be defined), failure occurs if the tensile fibre strain is greater than DFAILT or less than DFAILC;
- if EFS is greater than zero, failure occurs if the effective strain is greater than EFS;
- if TFAIL is greater than zero, failure occurs according to the element time-step.

6.4.3 Composite material properties

CFRP unidirectional (UD) lamina stiffness properties were calculated by tests performed on the laminated composite (§5.4.1). In fact, knowing number, thickness and fibre orientation of each ply of tested laminate specimens, unidirectional lamina properties can be found to match the experimental laminate properties (Table 3). This reverse procedure was applied using CADEC 2007 (Computer Aided Design Environment for Composites) algorithm [76]. Nevertheless this approach does not give a unique solution in the case of hybrid materials.

CFRP UD lamina strength properties were provide by QinetiQ [43] as well as S2 glass material properties [77]; for E glass was used literature data [78].

In Table 5 are illustrated the material properties input in MAT_54.

Table 5 – MAT_54 composite material properties

	CFRP UD lamina	**E glass UD lamina**	**S2 glass UD lamina**
Density [kgm^{-3}]	1600	1580	1990
E_1 [GPa]	127	40	56
E_2 [GPa]	17	10	18

G_{12} [GPa]	6	4	7.5
X_T [MPa]	1500	1000	1770
X_C [MPa]	1200	600	965
Y_T [MPa]	50	27.5	61.5
Y_C [MPa]	250	142	155
S_C [MPa]	70	38	113.5
β	0.5	0.5	0.5
DFAILT	0.015	N/A	0.057
DFAILC	-0.015	N/A	-0.027
DFAILM	N/A	N/A	0.012

6.5 Delamination model: tie-break contact with cohesive option

A delamination model was applied between each shell layers interface for the hybrid and CFRP composite models.

The model works through the contact tiebreak formulation [79] and, being a contact algorithm, it does not need definition of the elements. Tie-break contact allows the modelling of connections which transmits both compressive and tensile forces with optional failure criteria. Before failure, tie-break contact works both in tension and compression. After failure, this contact behaves as a surface-to-surface contact with thickness offsets. Hence, after failure, no interface tension is possible. Different tie-break failure criteria can be defined. With option 9 a failure criteria can be defined that is an extension of Dycoss Discrete Crack Model [80] based on the fracture model defined in the cohesive material model: *MAT_COHESIVE_MIXED_MODE. This card is a simplification of *MAT_COHESIVE_GENERAL restricted to linear softening. It includes a bilinear traction-separation law with a quadratic mixed mode delamination criterion and a damage formulation [59]. In the interface cohesive model the ultimate displacements in the normal and tangential directions are the displacements at the time when the material has failed completely. The bilinear traction-separation law gives a linear stiffness for loading followed

by the linear softening during the damage and provides a simple relationship between the energy release rates, the peak tractions and the ultimate displacements:

$$G_{IC} = \frac{T \cdot UND}{2}$$
$$G_{IIC} = \frac{S \cdot UTD}{2} \tag{26}$$

where:

- T is the peak traction in normal direction;
- S is the peak traction in tangential direction;
- UND is the ultimate displacement in the normal direction;
- UTD is the ultimate displacement in the tangential direction;
- G_{IC} is the Mode I energy release;
- G_{IIC} is the Mode II energy release.

If the peak tractions are not specified, they can be computed from the ultimate displacements. In the cohesive material model, the total mixed-mode relative displacement δ_m is defined as $\delta_m = \sqrt{\delta_I^2 + \delta_{II}^2}$, where $\delta_I = \delta_3$ is the separation in normal direction (Mode I) and $\delta_{II} = \sqrt{\delta_1^2 + \delta_2^2}$ is the separation in tangential direction (Mode II). The mixed-mode damage initiation displacement δ^0 (onset of softening) is given by:

$$\delta^0 = \delta_I^0 \delta_{II}^0 \sqrt{\frac{1+\beta^2}{(\delta_{II}^0)^2 + (\beta\delta_I^0)^2}} \tag{27}$$

where $\delta_I^0 = T/EN$ and $\delta_{II}^0 = S/ET$ are the single mode damage initiation separation, EN is the stiffness normal to the interface plane, ET is the stiffness into the interface plane and β is the "mode mixity" (Figure 45).

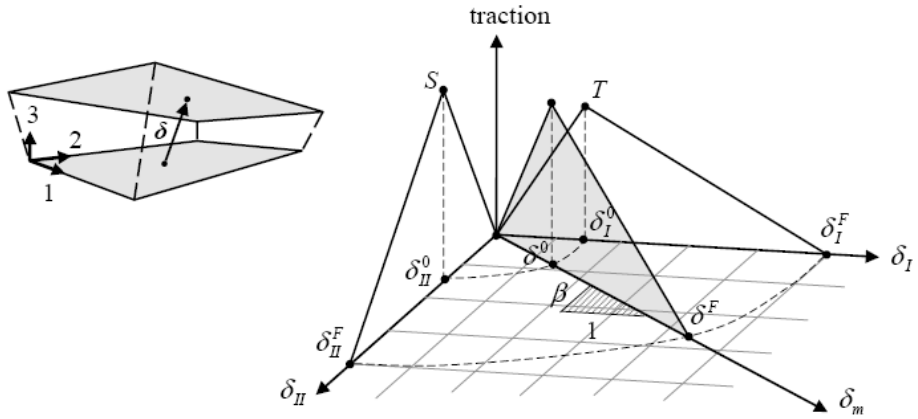

Figure 45 – Mixed-mode traction-separation law

The ultimate mixed-mode displacement δ^F (total failure) for the Benzeggagh-Kenane law is:

$$\delta^F = \frac{2}{\delta^0\left(\frac{1}{1+\beta^2}EN + \frac{\beta^2}{1+\beta^2}ET\right)}\left[G_{IC} + \left(G_{IIC} - G_{IC}\right)\left(\frac{\beta^2 ET}{EN + \beta^2 ET}\right)^{XMU}\right] \tag{28}$$

where XMU is the exponent of the mixed-mode criteria.
*AUTOMATIC_ONE_WAY_SURFACE_TO_SURFACE_CONTACT card with mixed-mode cohesive option requires:

- NFLS, normal failure stress (=T);
- SFLS, shear failure stress (=S);
- ERATEN, normal energy release (=G_{IC});
- ERATES, shear energy release (=G_{IIC});
- PARAMETER, exponent of the mixed mode criteria (=XMU);
- CT2CN, ratio of the tangential stiffness to the normal stiffness (=β).

The value inputs into the model are illustrated in Table 6. ERATEN for Carbon/Carbon, E/E and S2/S2 interfaces was obtained from EUROPA experimental tests (Figure 24, Figure 25 and Figure 26), while for E/Carbon and S2/Carbon hybrid interfaces intermediate values were applied. Besides, NFLS=SFLS and ERATEN=ERATES were assumed.

Table 6 – Delamination model parameters

*AUTOMATIC_ONE_WAY_SURFACE_TO_SURFACE_CONTACT					
Interface	Carbon/Carbon	E/E	S2/S2	E/Carbon	S2/Carbon
NFLS [MPa]	35	35	35	35	35
ERATEN [J/m^2]	300	450	800	375	550
PARAMETER	1	1	1	1	1
CT2CN	0.7	0.7	0.7	0.7	0.7

6.6 Blast modelling

To model blast pressure both CONWEP (§3.4) and MMALE (§4.6) approach were applied on steel RHA, while only Eulerian approach were used with composite models because of incompatibility between CONWEP and delamination model.

6.6.1 CONWEP

In LS-DYNA CONWEP function is called with *LOAD_BLAST card (§3.5). The inputs that it requires are the following:

- TNT equivalent mass;
- stand-off distance, 150 mm (Figure 46);
- type of burst, in this case free air spherical burst (§2.5);

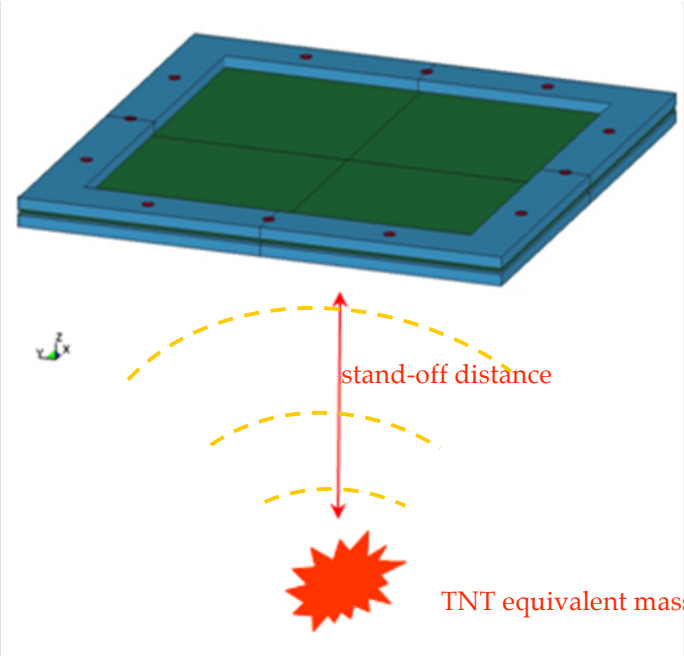

Figure 46 – CONWEP

The ratio between TNT and C-4 is a critical value. C-4 explosives release more energy per kilo than TNT by a factor 1.14 [49, 81].

*LOAD_BLAST function reproduces a field of vectors on the target's nodes that changes with the time. Unfortunately it was verified that these forces produce high distortion of the elements on the shell elements if the shell layer is in contact with another shell layer, such as for the composite model.

6.6.2 MMALE model

Another way to model the blast pressure on the target is by modelling the environment that surrounds the target as well as the land mine explosive. For the reasons argued in §4.5, the only way to model these materials is through an Eulerian approach. In order to perform this kind of analysis further inputs are required, such as explosive and air material properties and materials EOS. Furthermore, explosive and air mesh need to be generated into the FE model. The interface between Eulerian ambient (air + explosive) and Lagrangian structure (target) also needs to be defined.

This approach implies a much longer computational time than CONWEP function but in certain cases it is the only applicable way.

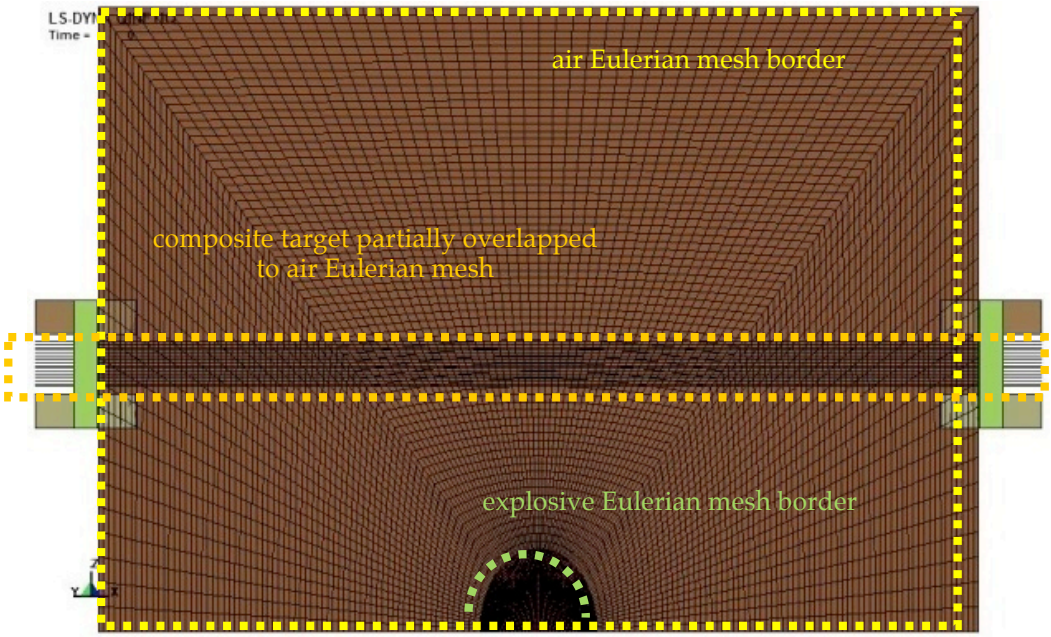

Figure 47 – Eulerian model

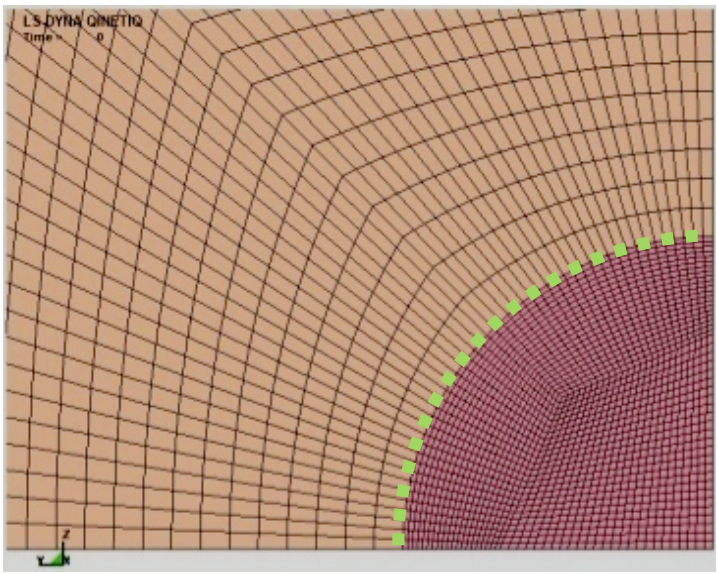

Figure 48 – Multi Material Eulerian interface

Eulerian ambient was modeled with 1 point MMALE solid element with ambient pressure outflow option in order to allow the fluid flowing outside the mesh boundaries (Figure 49). The symmetry boundary conditions were guaranteed by the slip condition applied to symmetry plane YZ and XZ (fluid flow's normal component equal to zero) (Figure 50).

The number of Eulerian elements is about 171.000, hence the elements total number is about 340.000 for the composite model and between 251.000 (shell elements) and 296.000 (solid elements) for the steel RHA model.

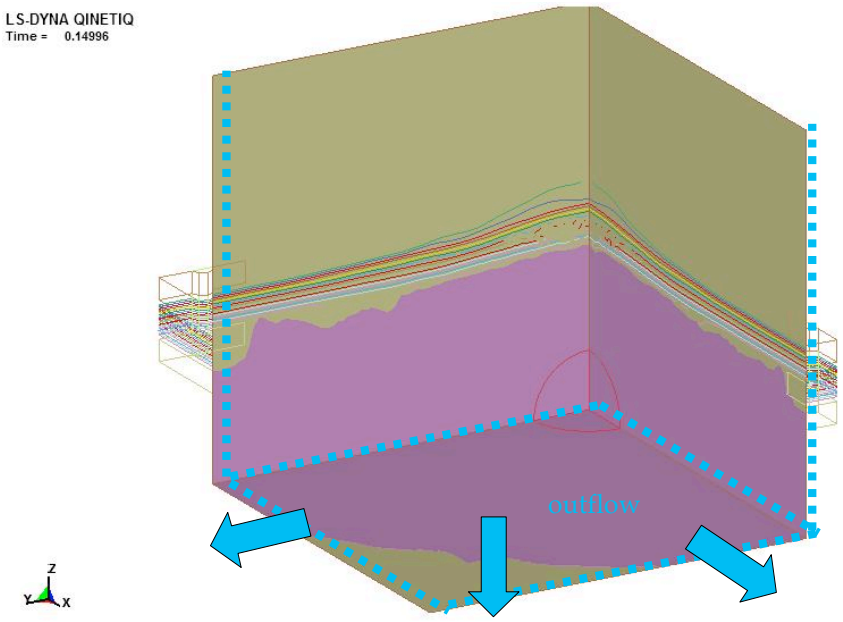

Figure 49 – Eulerian outflow conditions

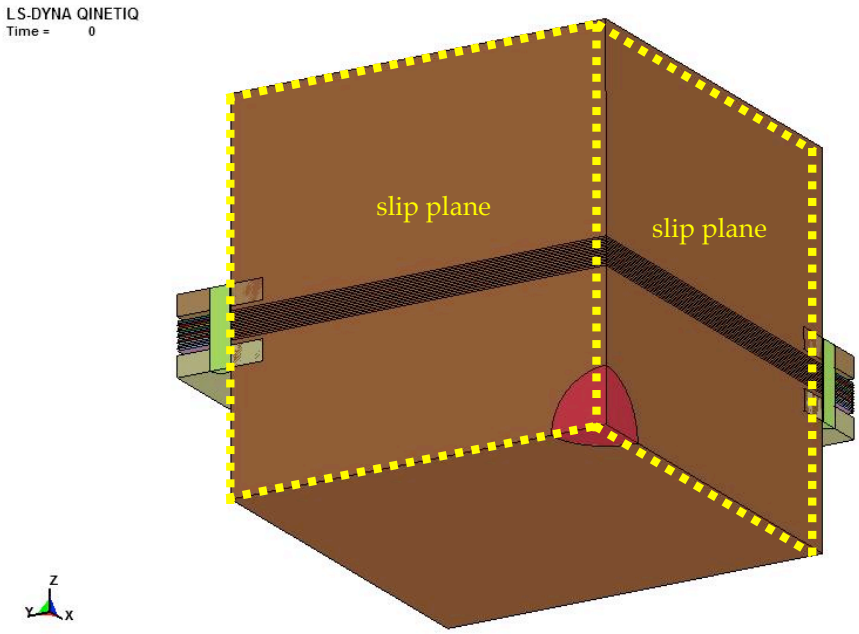

Figure 50 – Eulerian slip boundary conditions

To model air and explosive material behaviors *MAT_NULL and *MAT_HIGH_EXPLOSIVE_BURN were used respectively. These cards require an EOS: for the air was used a linear polynomial EOS, while for the explosive the JWL EOS. The values input into the models are illustrated in Table 7 [80].

Table 7 – Air and explosive LS-DYNA cards [mm, kg, ms]

***MAT_NULL (air)**

```
*MAT_NULL
        ro        pc        mu      terod      cerod        ym        pr
 1.225E-9     0.000     0.000     0.000     0.000     0.000     0.000
```

***EOS_LINEAR_POLYNOMIAL (air)**

```
*EOS_LINEAR_POLYNOMIAL
        c0        c1        c2        c3        c4        c5        c6
     0.000     0.000     0.000     0.000  0.400000  0.400000     0.000
        e0        v0
 2.5000E-4  1.000000
```

***MAT_HIGH_EXPLOSIVE_BURN (C-4)**

```
*MAT_HIGH_EXPLOSIVE_BURN
        ro         d       pcj      beta         k         g      sigy
 1.6000E-6  8193.000 28.040001         0         0         0         0
```

***EOS_JWL (C-4)**

```
*EOS_JWL
         a         b        r1        r2      omeg        e0        vo
 609.77002 12.950000  4.500000  1.400000  0.250000  9.000000  1.000000
```

The history plot of ambient pressure generated in Eulerian mesh is illustrated in Figure 51 for the case C-4 charge size of 750 g at distance of 50 and 100 mm.

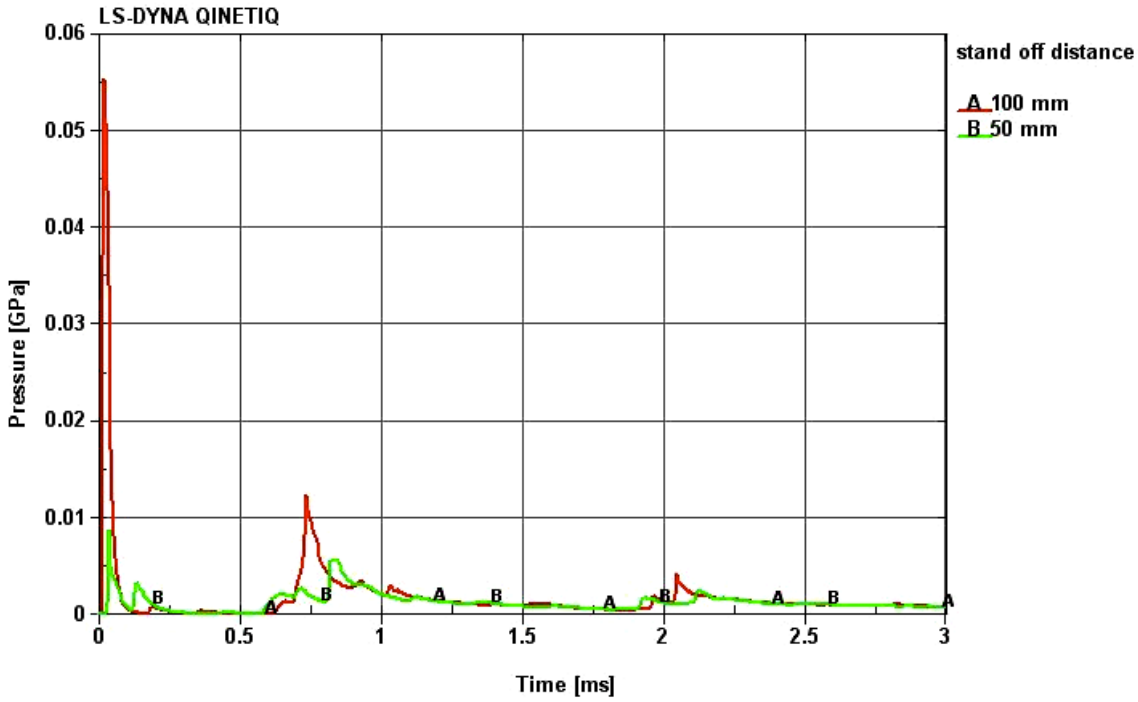

Figure 51 – Pressure history plot

The contact between the Eulerian fluid flow and the Lagrangian target can be modeled by an *ad hoc* algorithms called Arbitrary Lagrangian-Eulerian (ALE) (§4.6). This kind of function is defined in LS-DYNA through a specific card called *CONSTRAINED_LAGRANGE_IN_SOLID that provides the coupling mechanism for modeling Fluid-Structure Interaction (FSI) (Figure 52). In the case of composite model an FSI card was defined for each ply giving a total number of 16 and 14 FSI cards for hybrid and CFRP models respectively in order to guarantee the interaction also in the case of through thickness shells composite failure.

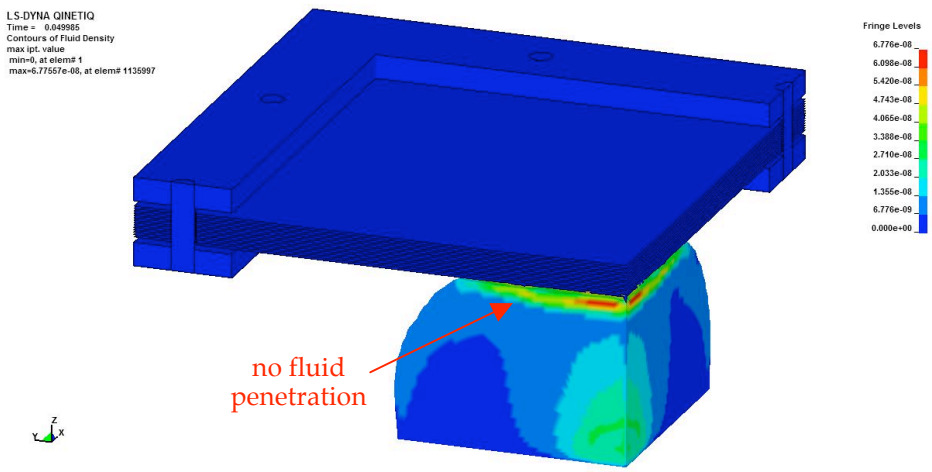

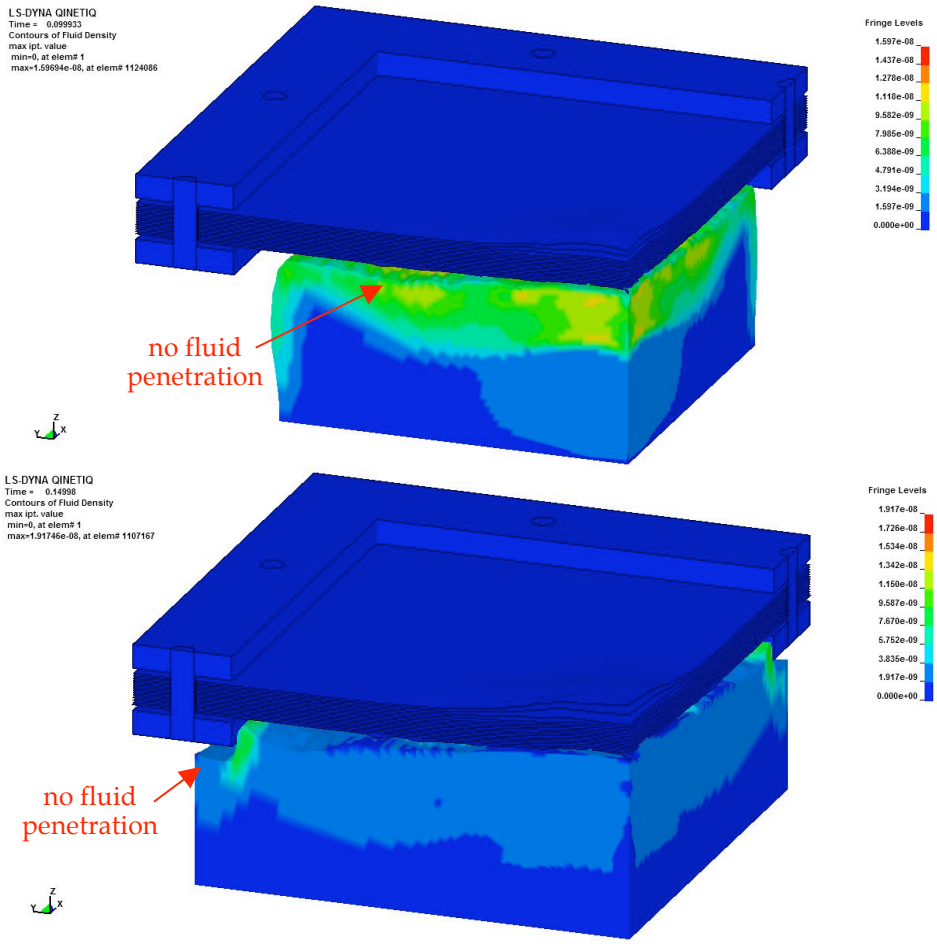

Figure 52 – Fluid Structure Interaction

This page is intentionally left blank

CHAPTER 7

Results of FE models and comparison with experimental tests

7.1 Introduction

In this last chapter numerical results obtained with the FE models described in Chapter 7 will be presented.

The results of steel RHA models comparing dynamic and residual deflection with experimental data will be presented. Then FE composite models response will be presented and compared with experimental data.

7.2 Steel target models results

The dynamic response of the RHA model is compared with experimental results [43] showing an excellent agreement for armour thickness of 10 mm and C-4 charge size of 1000 g (Figure 53). In this case the response of CONWEP and Eulerian models are quite similar, while there is an excellent agreement between shell and solid element models for the 5 mm target loaded by 750 g C-4 charge (Figure 54).

As time progresses the experimental response shows a greater deflection than that predicted by the FE models with a phase difference that is likely due to a numerical damping factor.

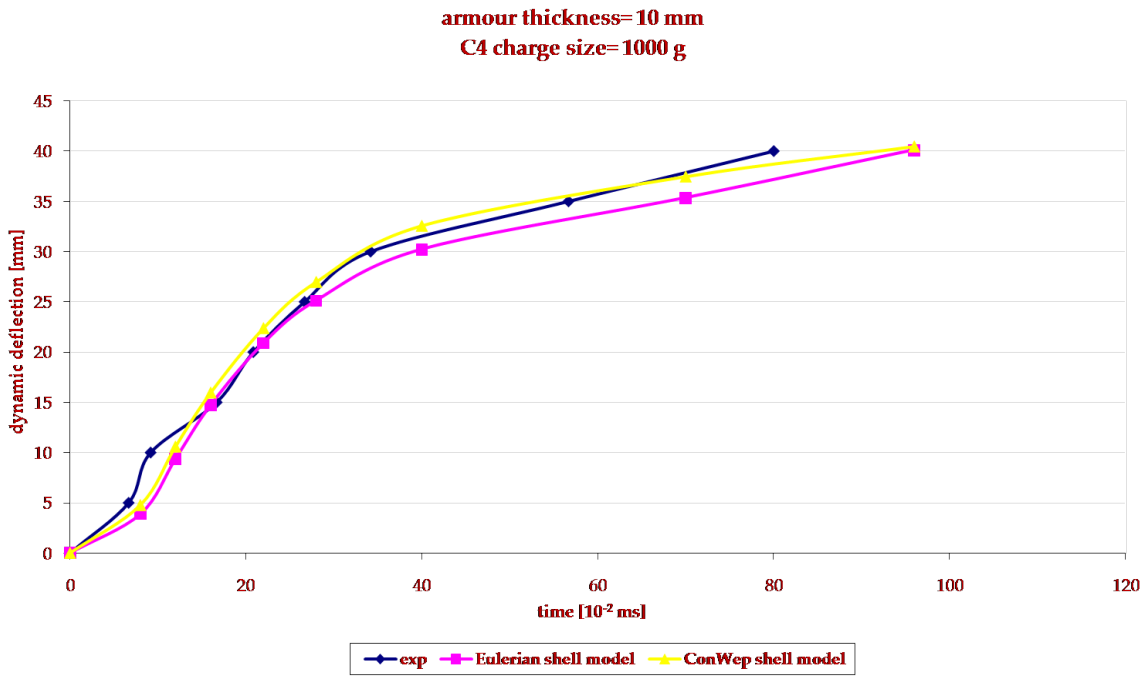

Figure 53 – Dynamic deflection steel RHA (10 mm 1000 g)

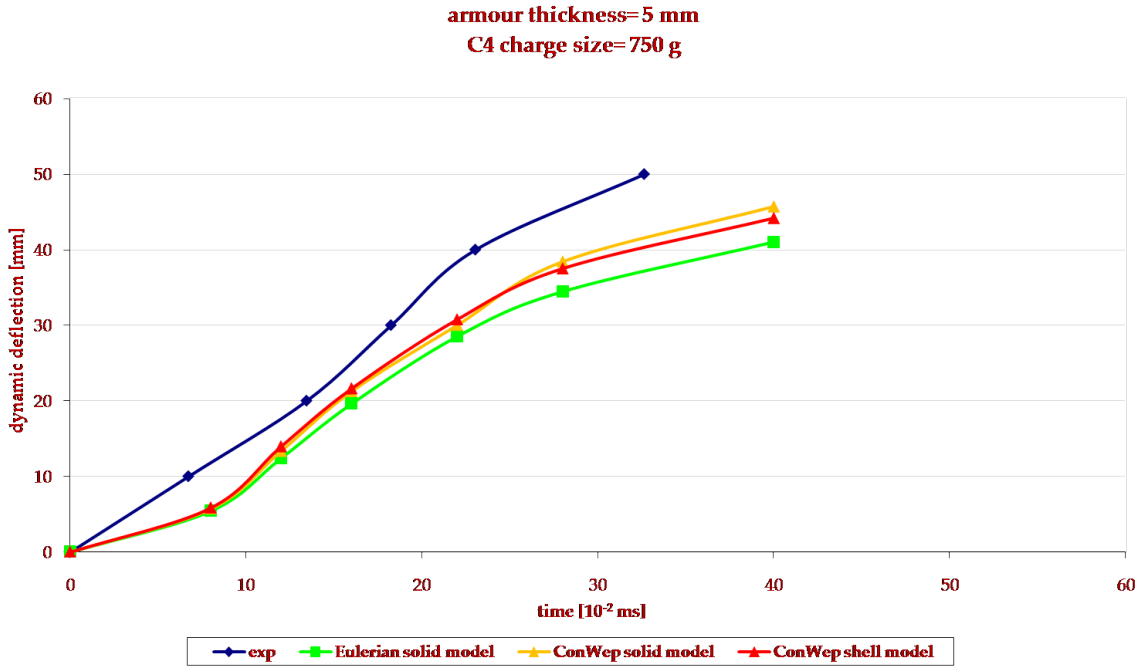

Figure 54 – Dynamic deflection steel RHA (5 mm 750 g)

The results of numerical modelling predictions are also compared with experimental response in terms of residual deflection for plates of varying thickness and loaded by different charge sizes (Figure 55, Figure 56 and Figure 57). Simulated deflection shows a good agreement with experimental data with a numerical response that, in general, overestimates the measured permanent deformation, except for the case of 6 mm thickness and 750 g

charge size. Nevertheless, in this particular case residual deflection (55 mm) is also greater than the 5 mm thickness response (51 mm).

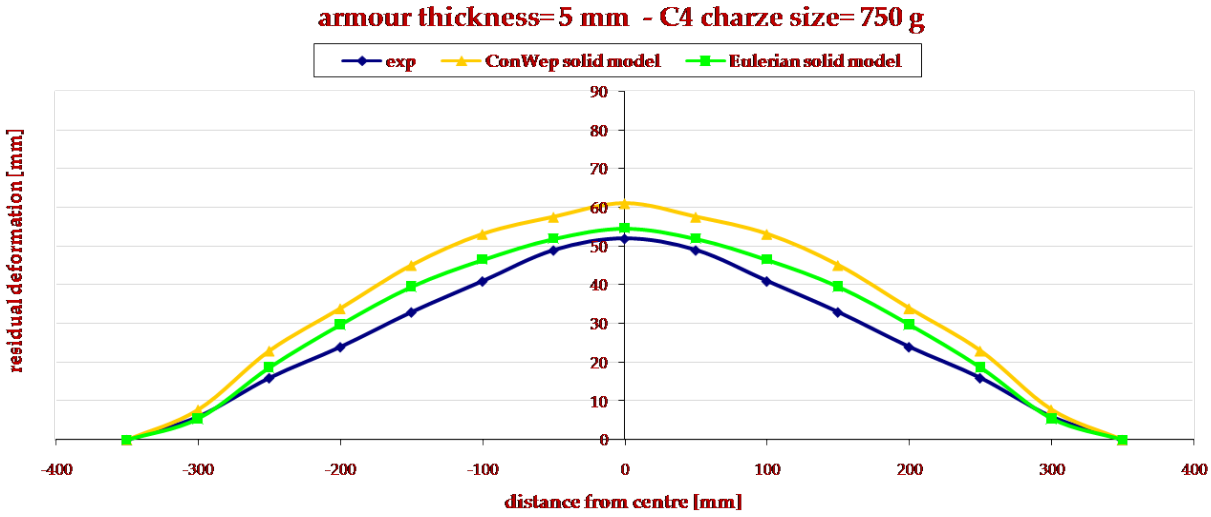

Figure 55 – Residual deflection steel RHA (5 mm 750 g)

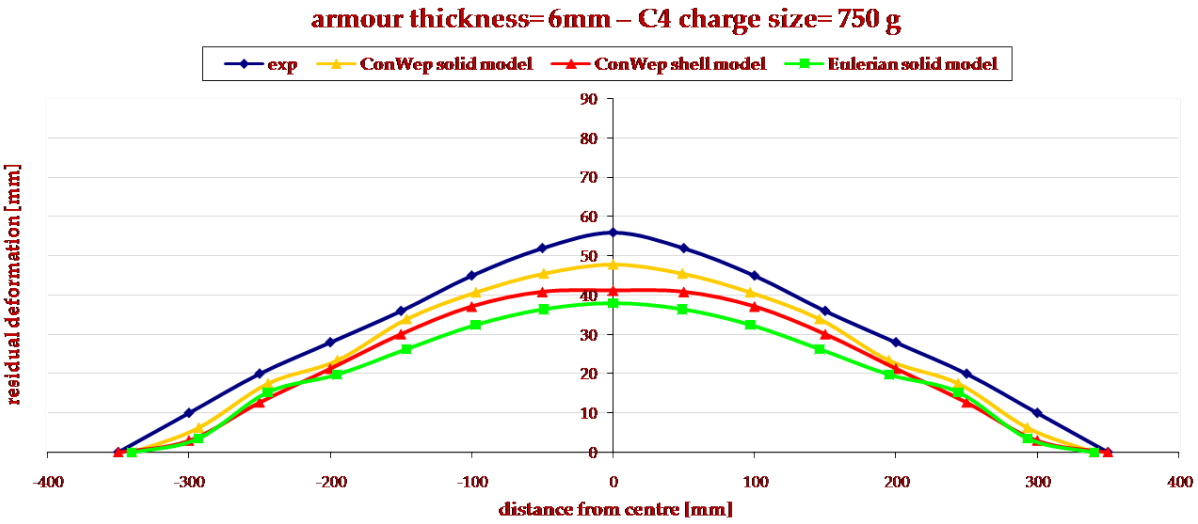

Figure 56 – Residual deflection steel RHA (6 mm 750 g)

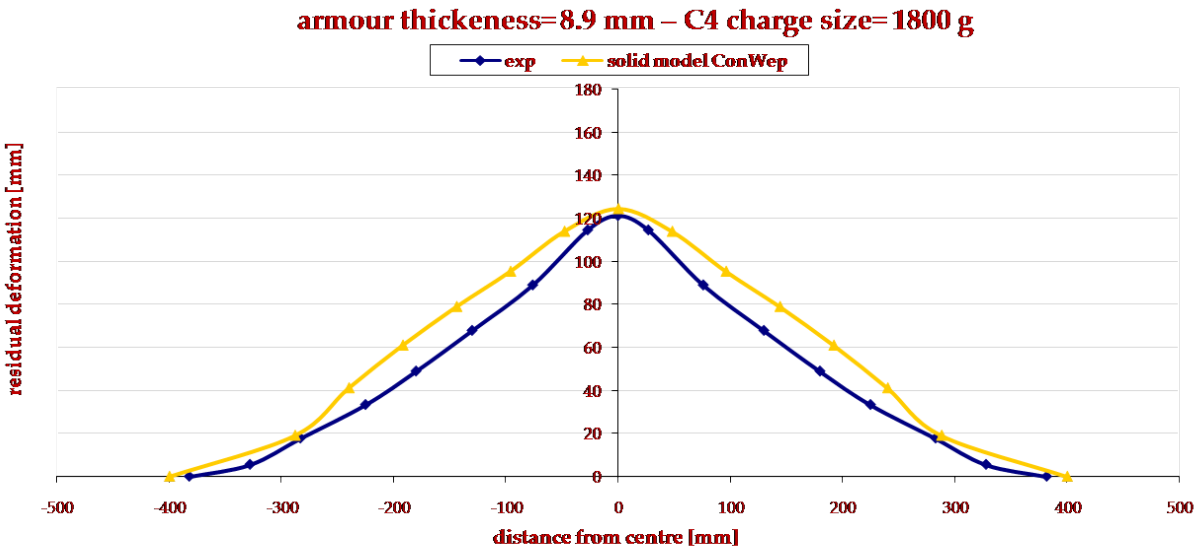

Figure 57 – Residual deflection steel RHA (8.9 mm 1800 g)

One explanation for this incoherent difference [43] is the natural variability of test results, which are highly dependent on a number of factors that are difficult to precisely control. Secondly, while both tests were conducted against RHA targets, the targets were produced by different manufacturers. Moreover, although both targets met the requirements for classification as RHA, small differences in mechanical properties can still exist.

However this anomalous test data could partially justify a numerical response different from experimental results as well as the dynamic deflection that overestimates the numerical prediction.

Figure 58 illustrates the vertical displacement of central node history plot and deformation shape sequence for the case 8.9 mm / 1800 g.

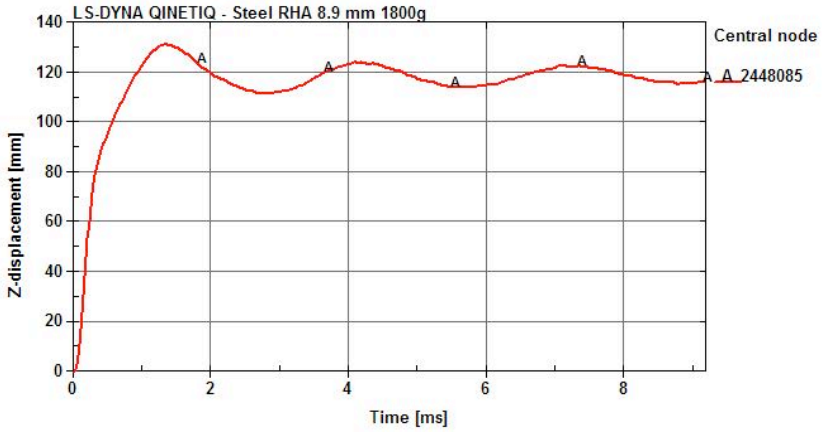

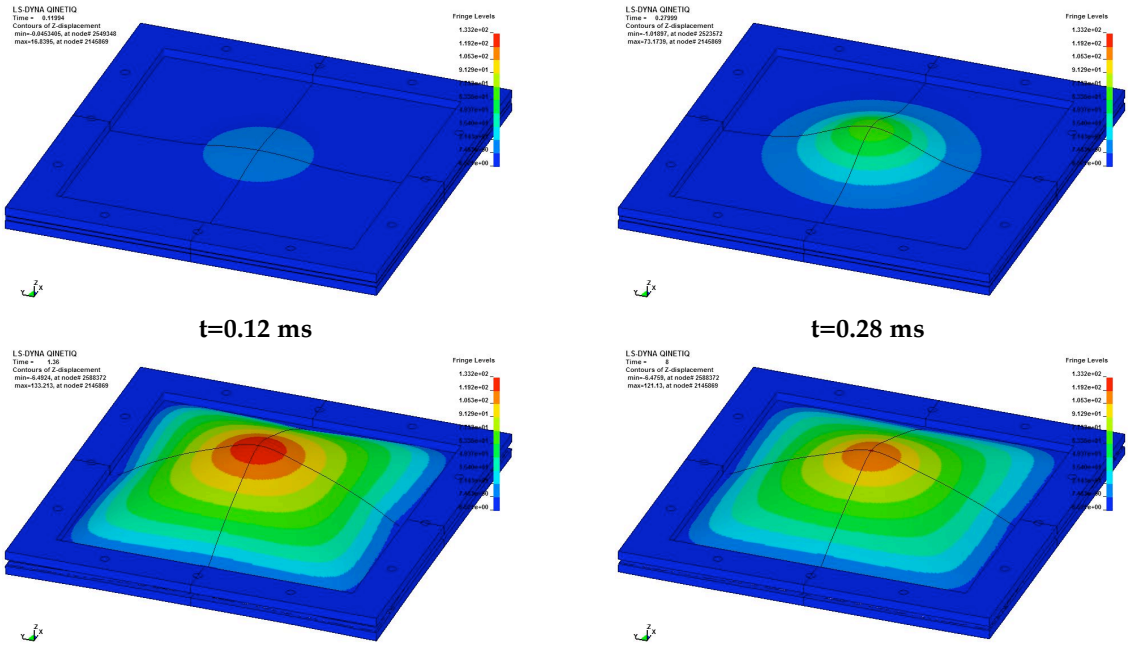

t=0.12 ms t=0.28 ms

t=1.36 ms t=8 ms

Figure 58 – Z displacement steel RHA (thickness 8.9 mm – charge size 1800 g)

7.3 Composite target models results

A comparison of FE with available experimental data provided by QinetiQ [43] in terms of dynamic deflection and damage extension as well as in terms of blast test results (passed/failed tests) is illustrated in Figure 44.

Two models were simulated for each composite material (CFRP, E/Carbon hybrid, S2/Carbon hybrid §5.6), one to simulate a passed and one to simulate a failed blast test in order to verify if the model can predict the measured armour's performance. However, new failure criteria need to be defined to assess the numerical damage; in fact, experimental damage assessment (§5.8) cannot certainly be applied to numerical models.

In Figure 59 is illustrated numerical dynamic deflection compared with experimental measure. Also if in the first instants of deflection numerical model appears fairly over-stiff, the steady-state response tends to the same deflection value and rate.

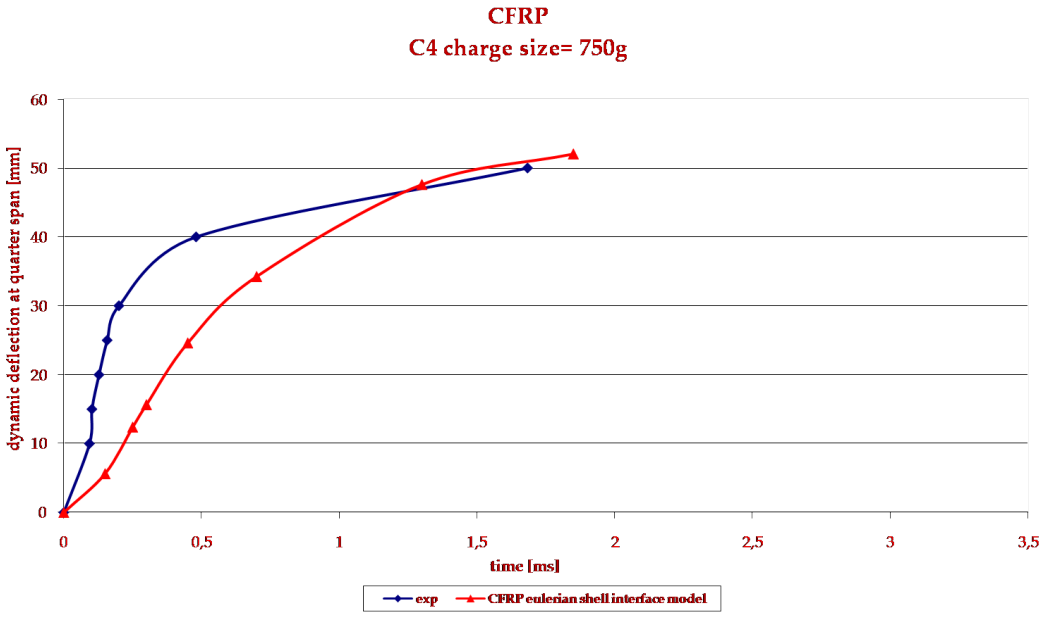

Figure 59 – Dynamic deflection CFRP

Composite ply internal energy histories are plotted for C-4 with charge size of 750 g. In Figure 60 the legend represented refers to Figure 61, Figure 62 and Figure 63.

The graphs show the contribution of front (P=16) and rear (A=1 and B=2) glass plies in the blast energy absorption. It can be noted how the presence of external glass plies reduce the energy absorption of internal carbon fibres plies that in this way preserve their blast resistance capability.

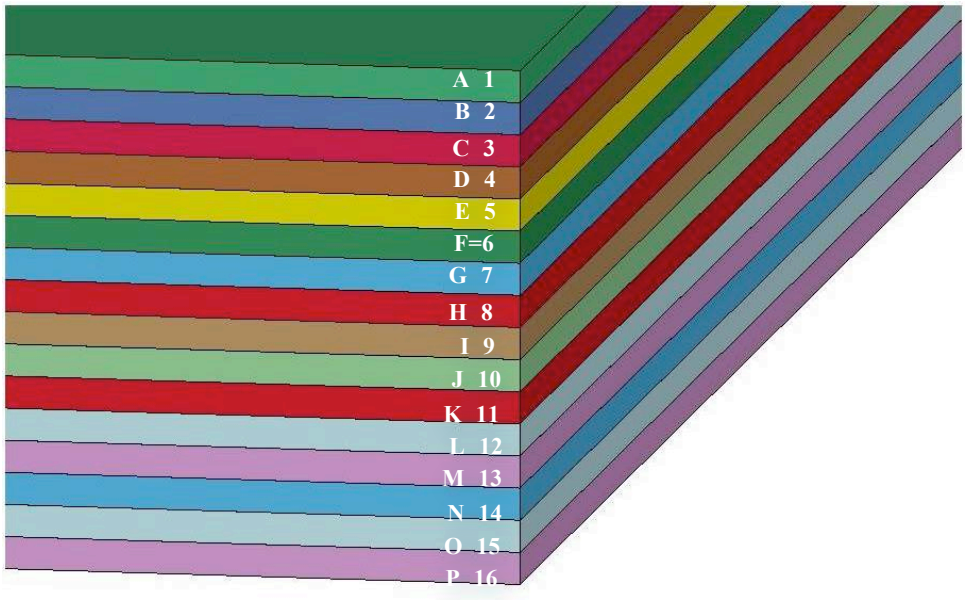

Figur gend

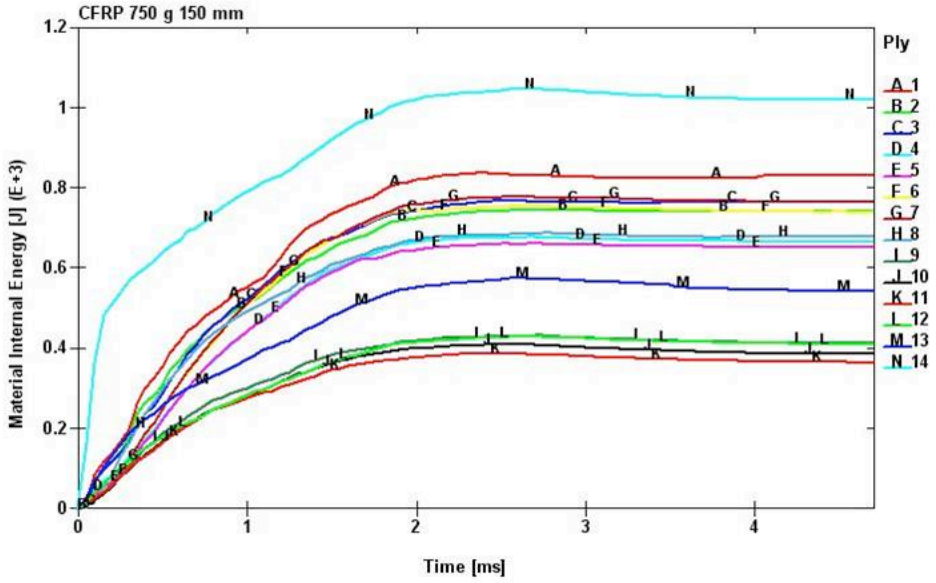

Figure 61 – CFRP internal energy history plot

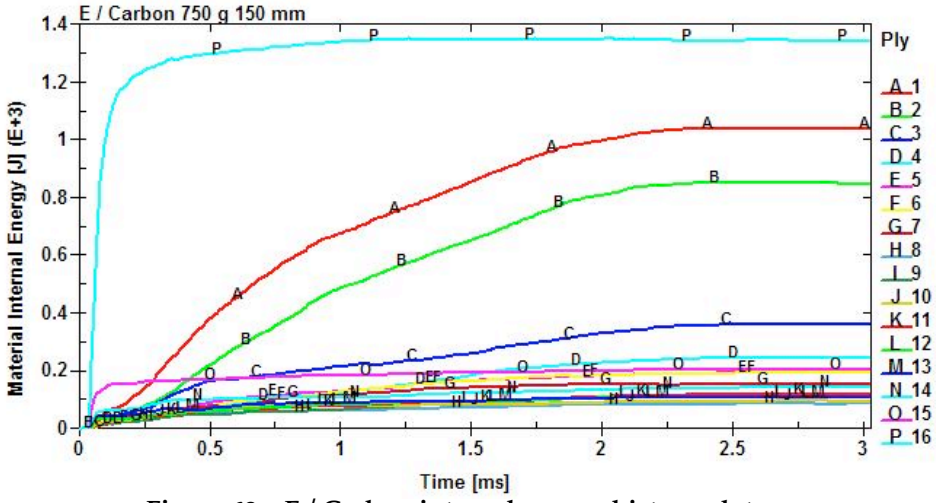

Figure 62 – E / Carbon internal energy history plot

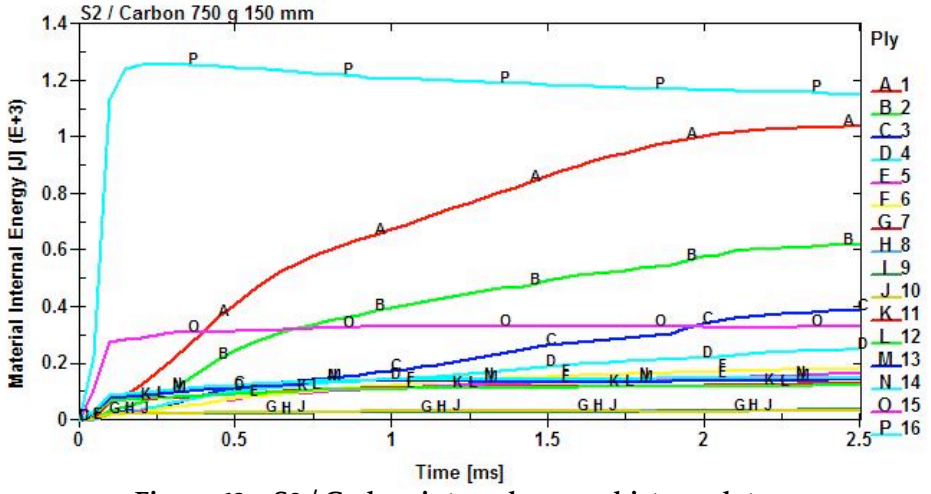

Figure 63 – S2 / Carbon internal energy history plot

In the following Figures from 64 to 75, results are summarised in terms of deformation shape evolution and damage map for each composite model.

The damage maps represent the composite failure distribution and they are split in fibre/matrix - tension/compression damages. The damage is maximum if it is equal to 0 (blue regions), minimum if it is equal to 1 (red regions). Each element is removed by LS-DYNA when the damage is equal to 0 in all its own integration points (4 integration points for CFRP model and 3 integration points for hybrid models §6.4.2).
Maximum integration point values (conservative condition) are illustrated in exploded view (z direction - factor 2) to better visualize the damage in each ply.

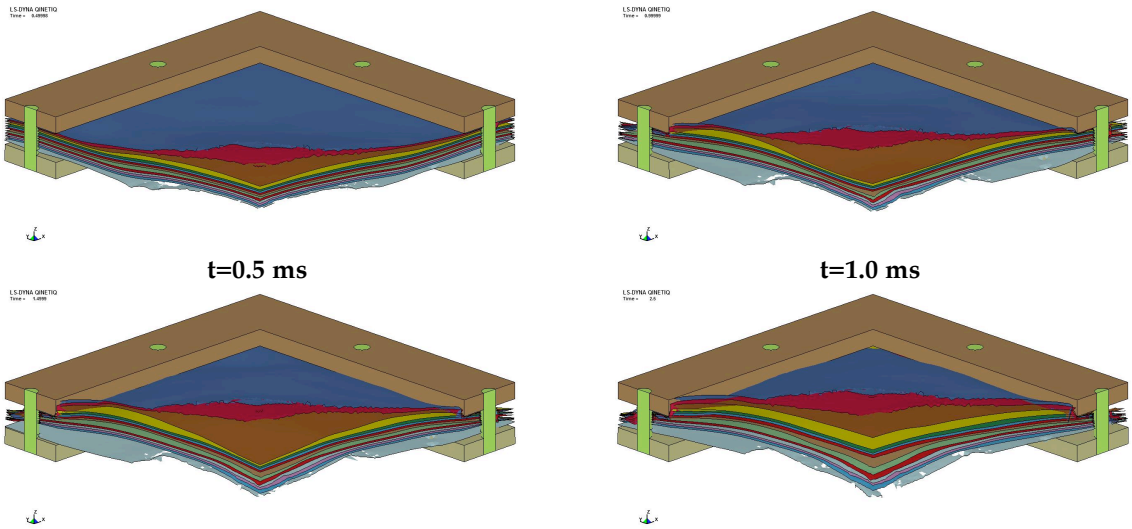

t=0.5 ms t=1.0 ms

t=1.5 ms t=2.5 ms

Figure 64 – Deformation shape CFRP 750 g

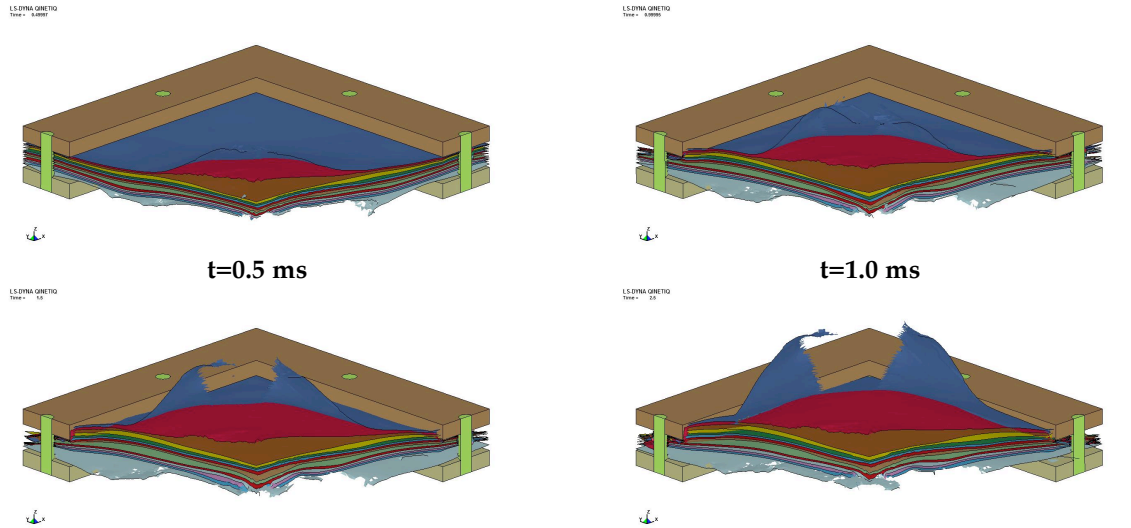

t=0.5 ms t=1.0 ms

t=1.5 ms t=2.5 ms

Figure 65 – Deformation shape CFRP 870 g

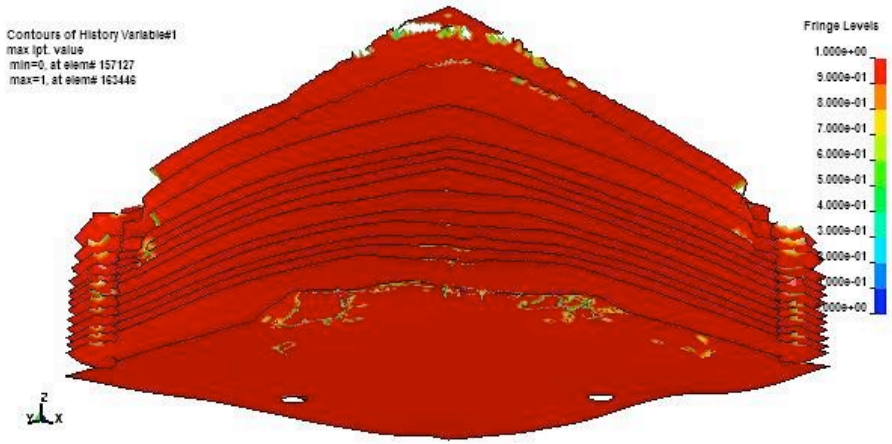

tensile fibre damage

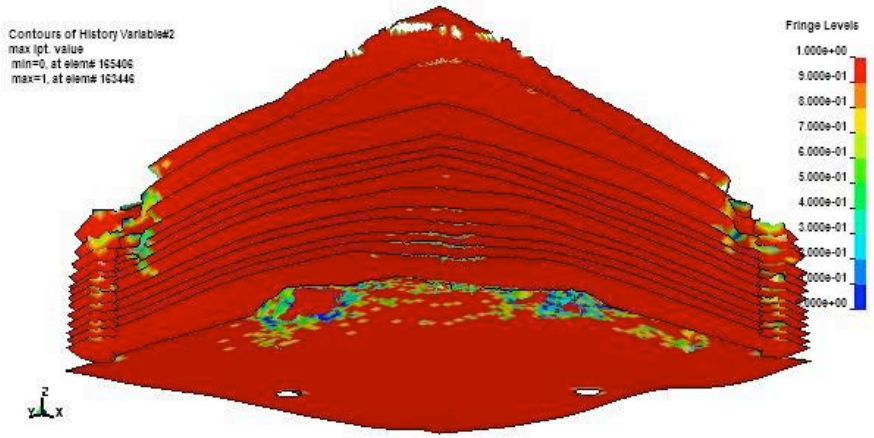

compressive fibre damage

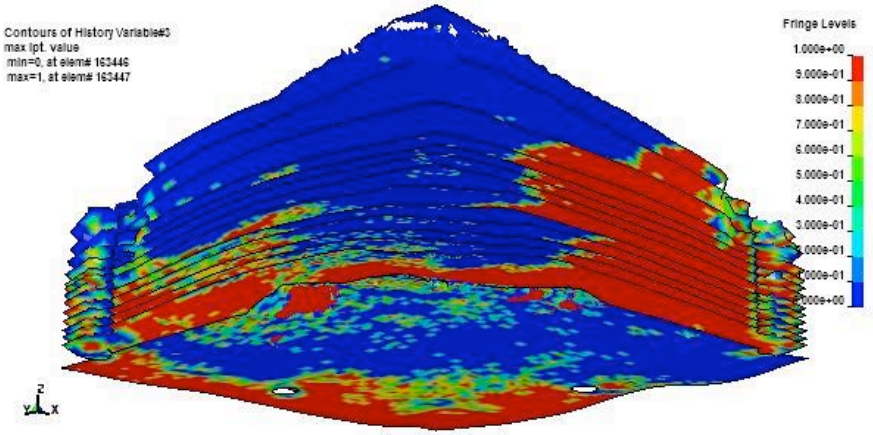

tensile matrix damage

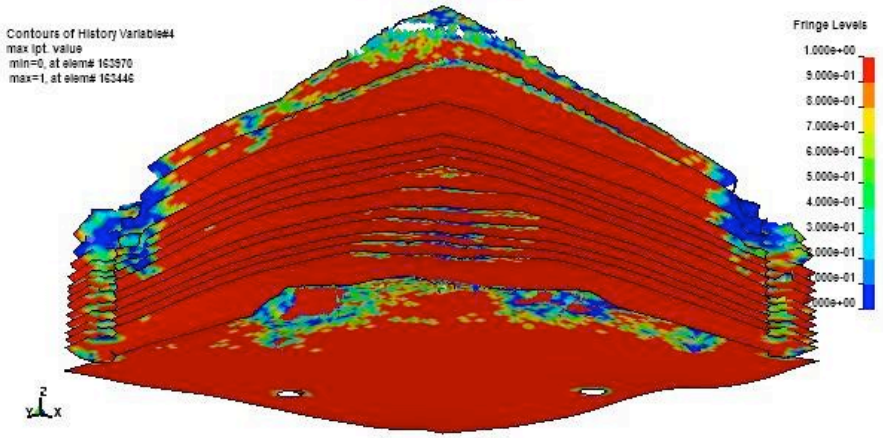

compressive matrix damage

Figure 66 – Damage maps CFRP 750 g

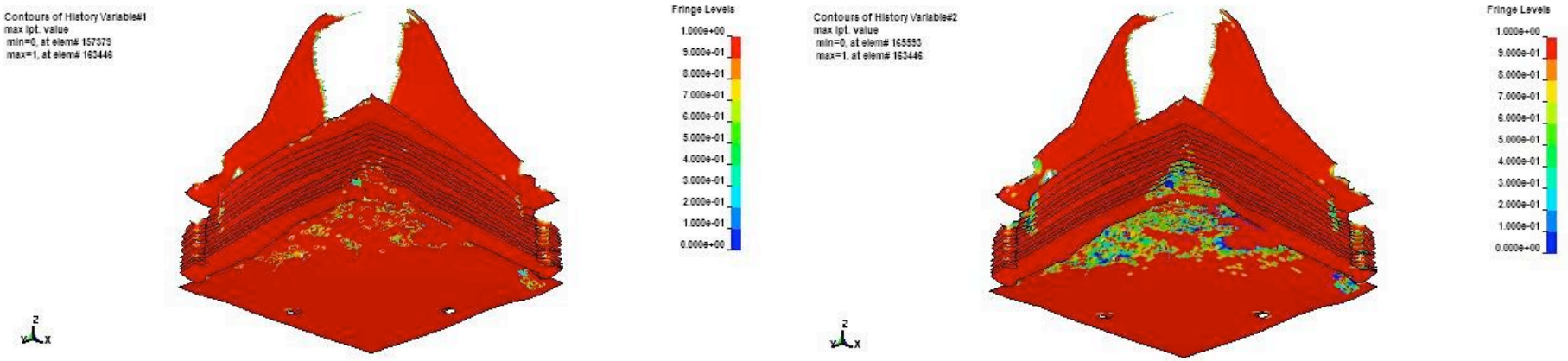

tensile fibre damage

compressive fibre damage

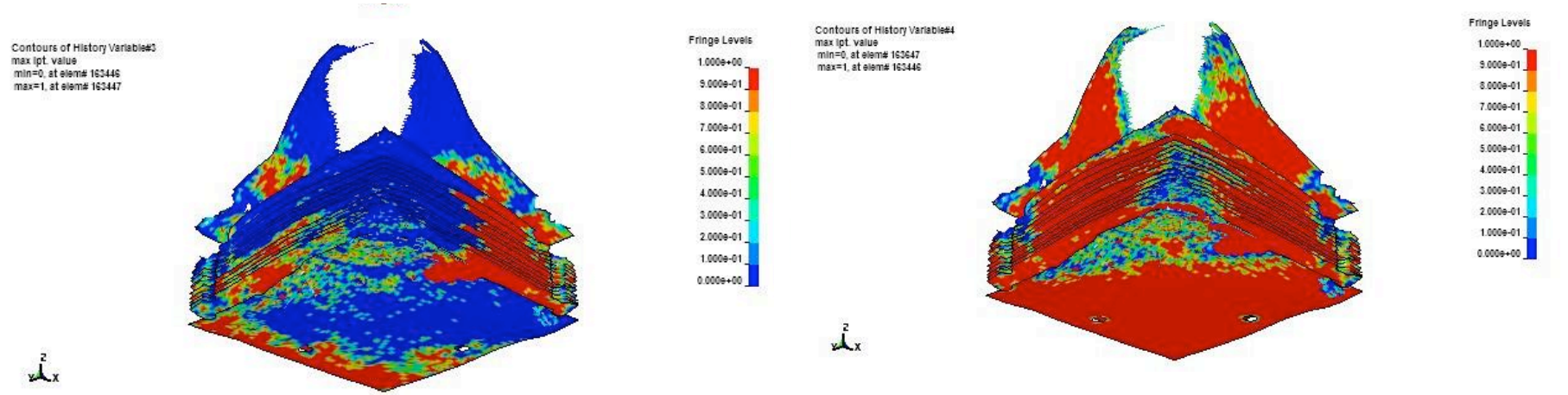

tensile matrix damage

compressive matrix damage

Figure 67 – Damage maps CFRP 870 g

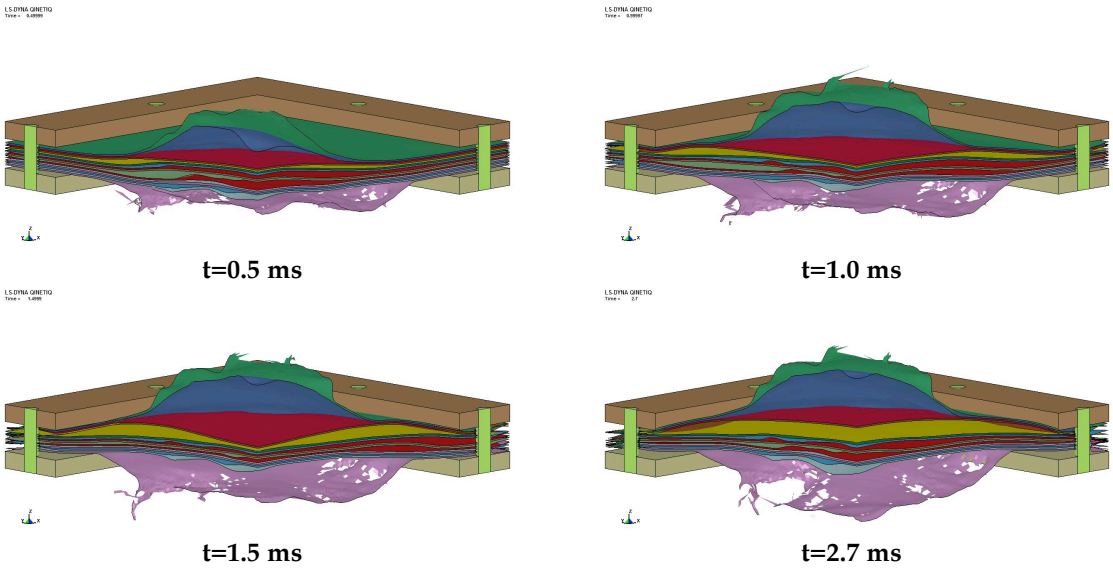

t=0.5 ms t=1.0 ms

t=1.5 ms t=2.7 ms

Figure 68 – Deformation shape E / Carbon 675 g

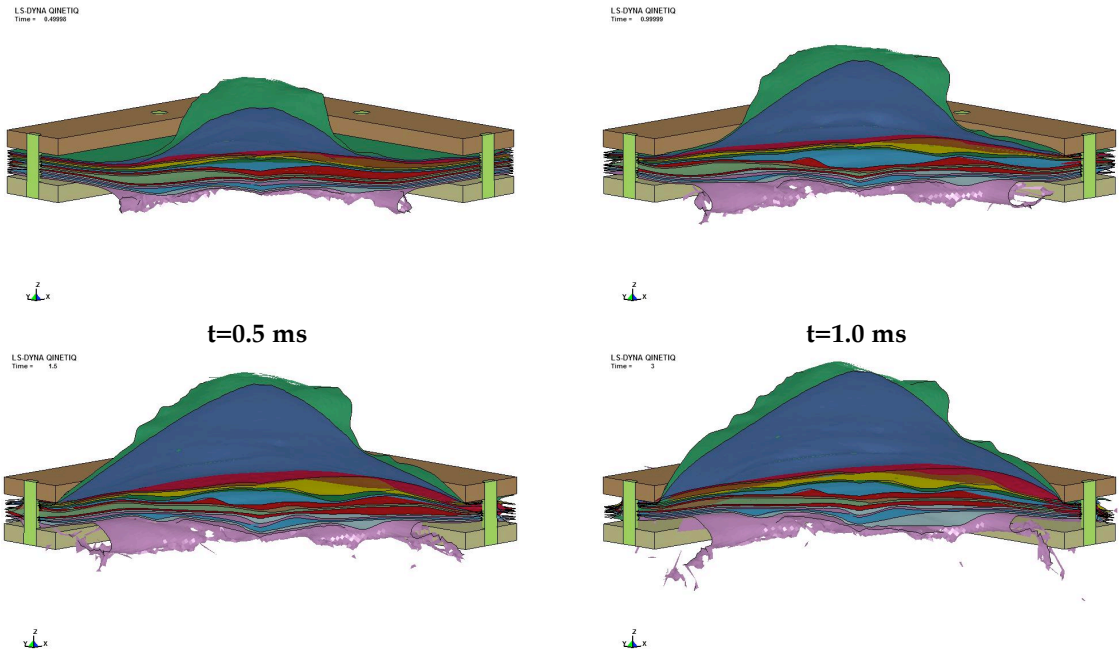

t=0.5 ms t=1.0 ms

t=1.5 ms t=3.0 ms

Figure 69 – Deformation shape E / Carbon 750 g

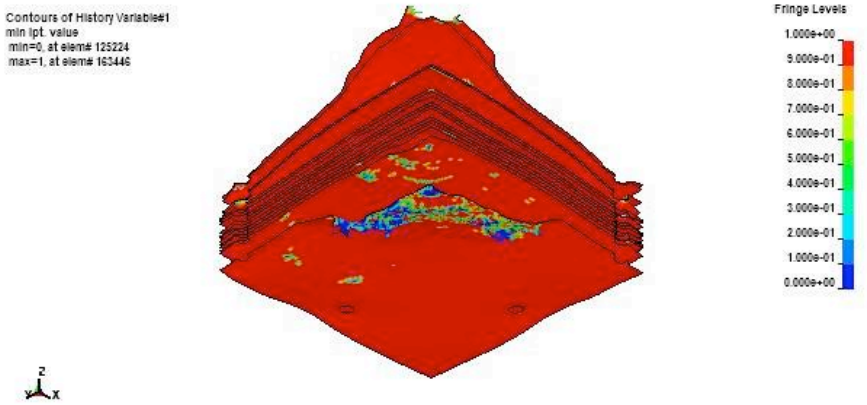

tensile fibre damage

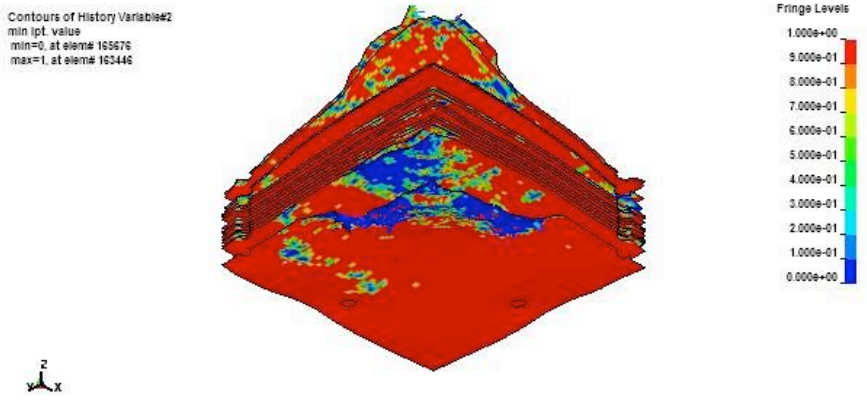

compressive fibre damage

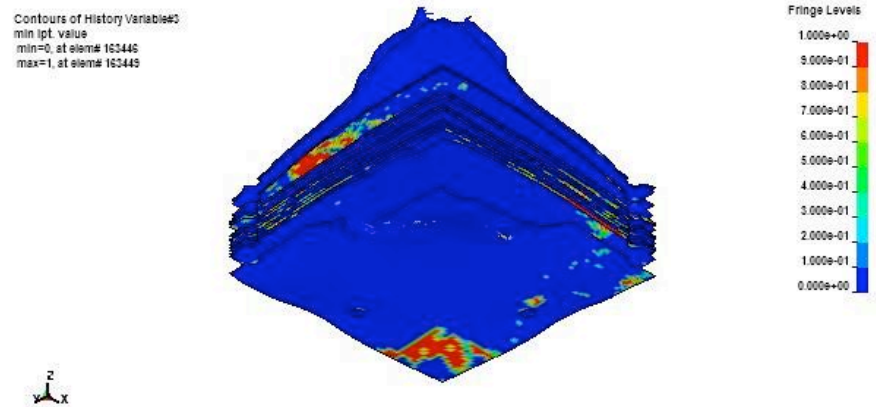

tensile matrix damage

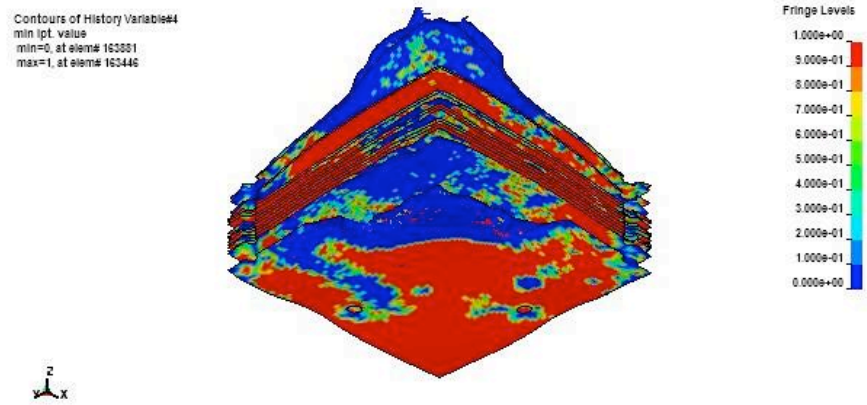

compressive matrix damage

Figure 70 – Damage maps E / Carbon 675 g

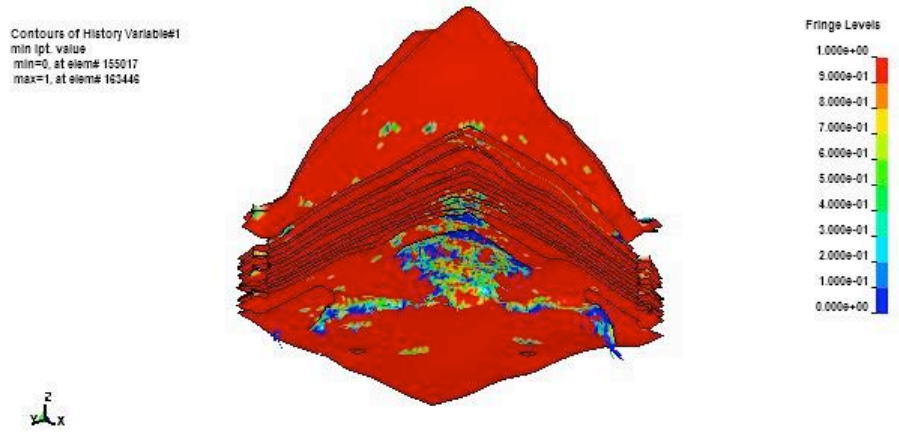

tensile fibre damage

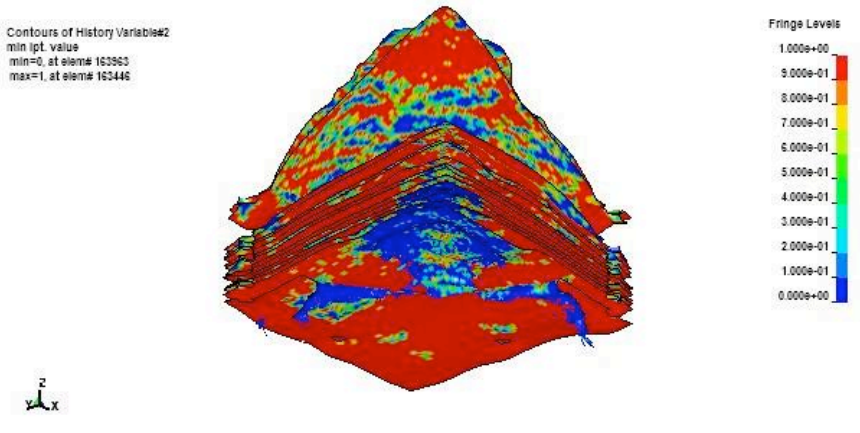

compressive fibre damage

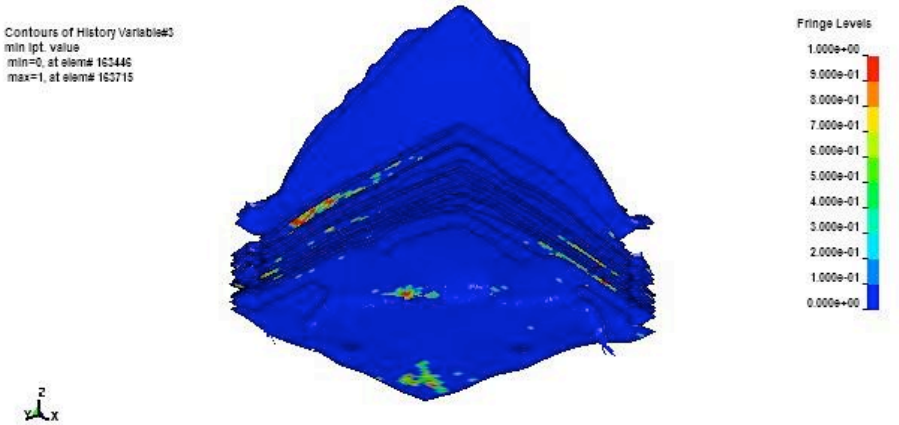

tensile matrix damage

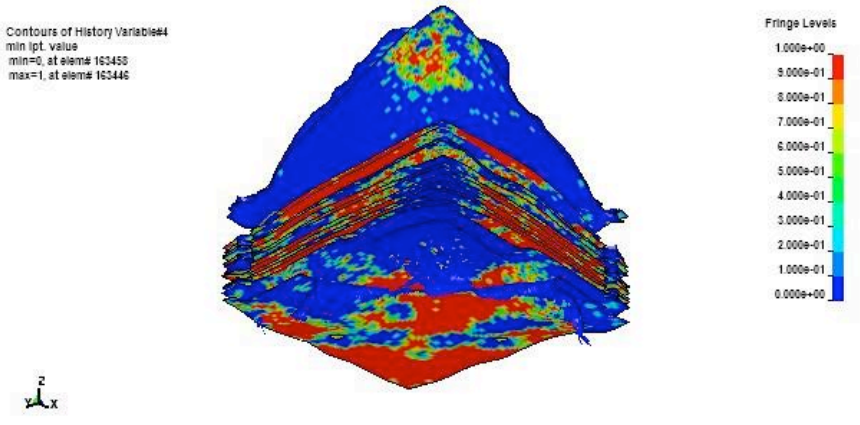

compressive matrix damage

Figure 71 – Damage maps E / Carbon 750 g

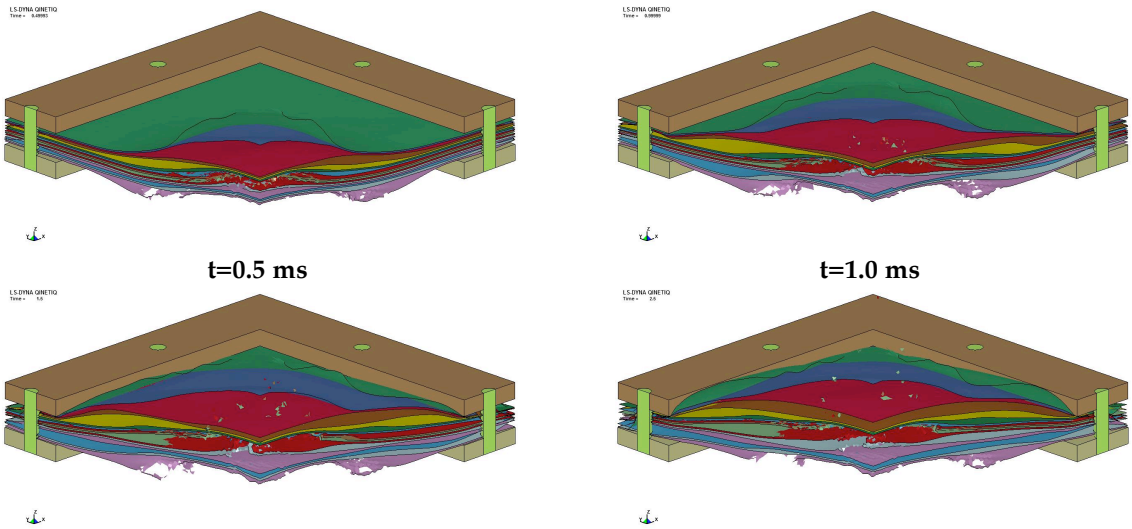

Figure 72 – Deformation shape S2 / Carbon 750 g

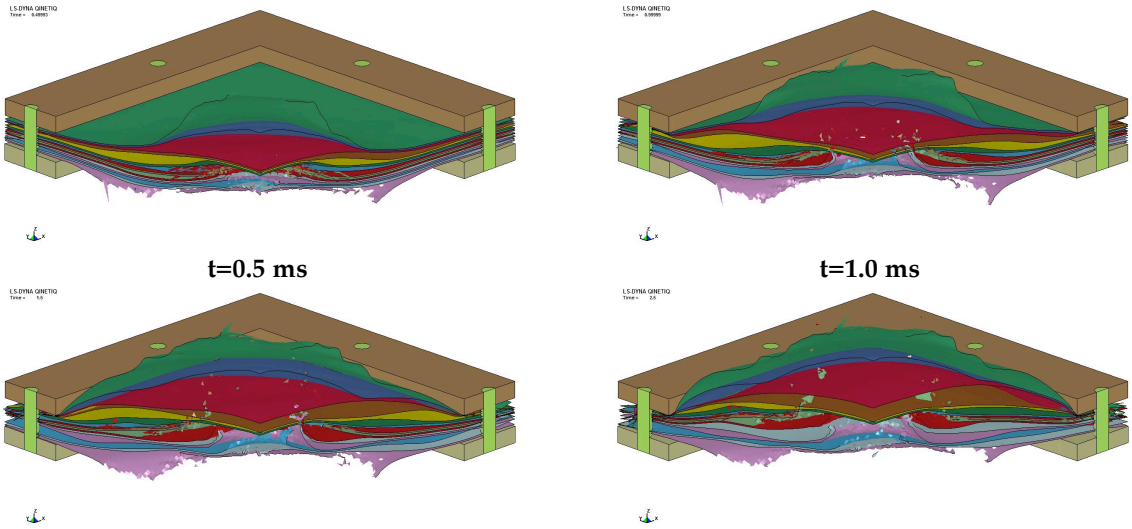

Figure 73 – Deformation shape S2 / Carbon 870 g

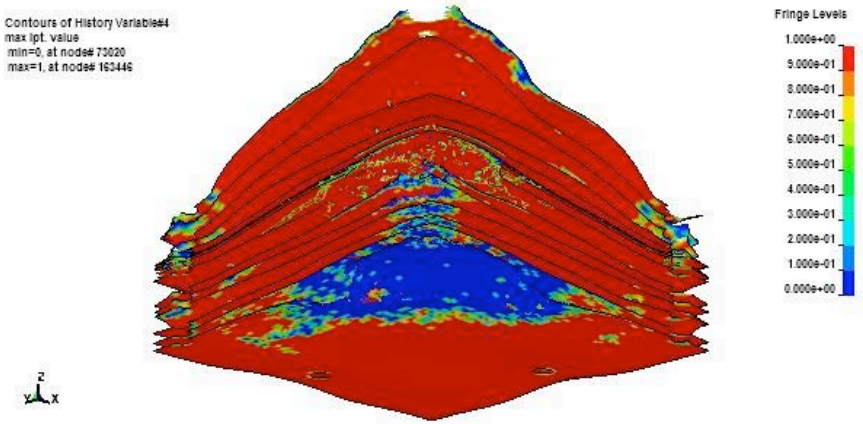

tensile fibre damage

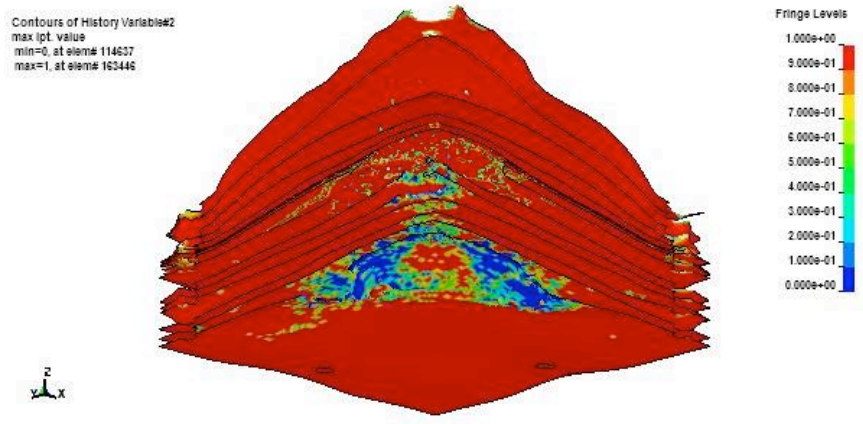

compressive fibre damage

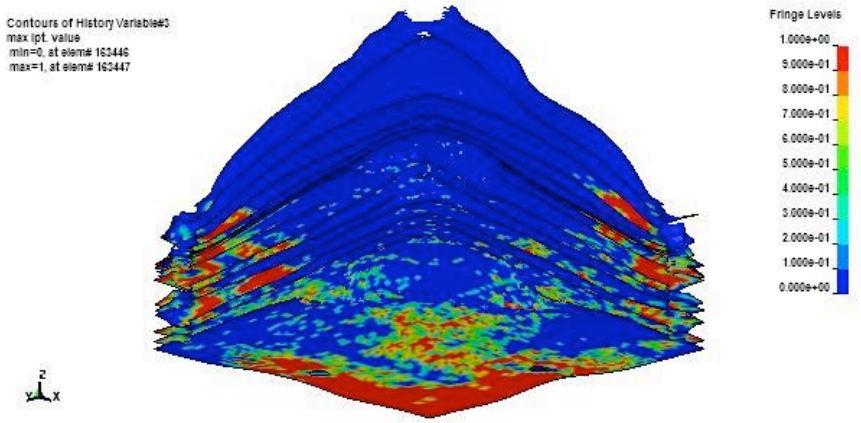

tensile matrix damage

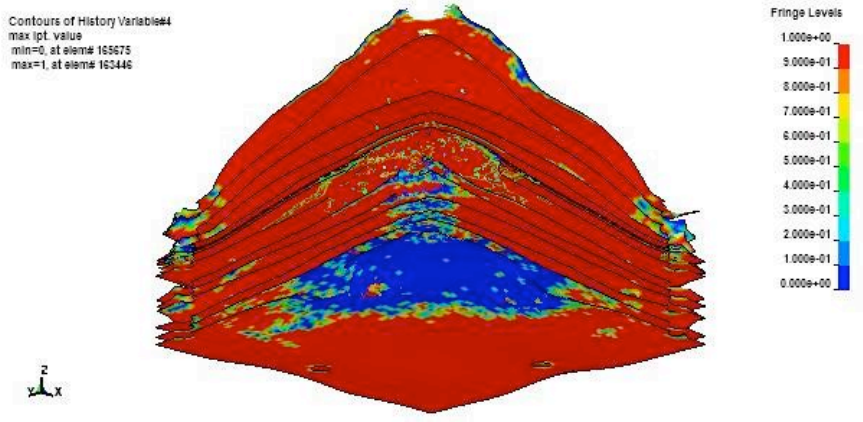

compressive matrix damage

Figure 74 – Damage maps S2 / Carbon 750 g

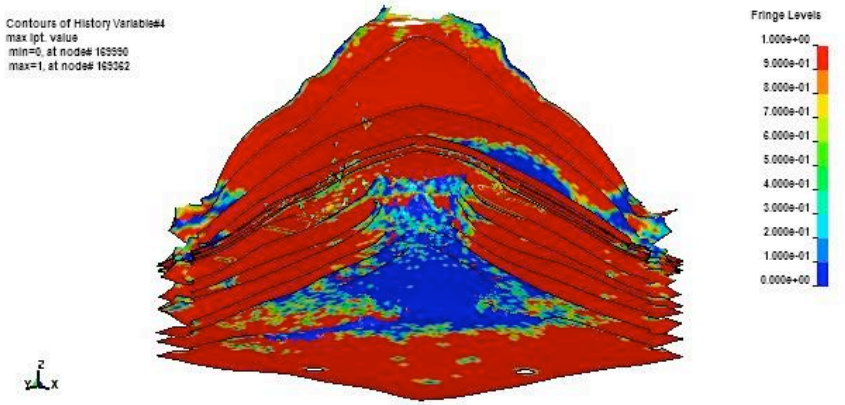

tensile fibre damage

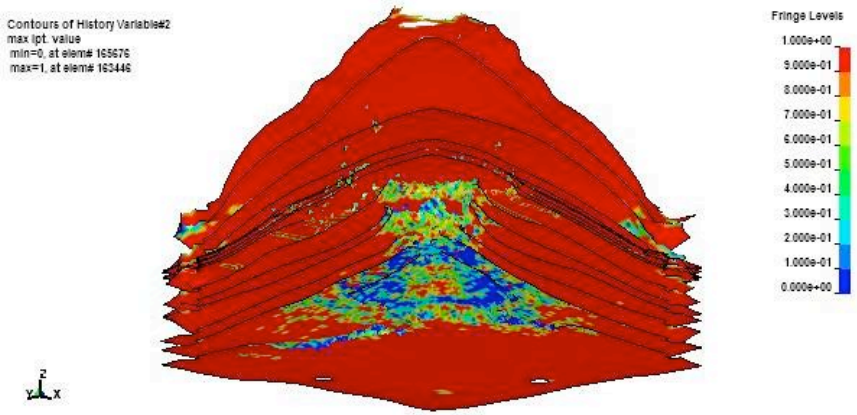

compressive fibre damage

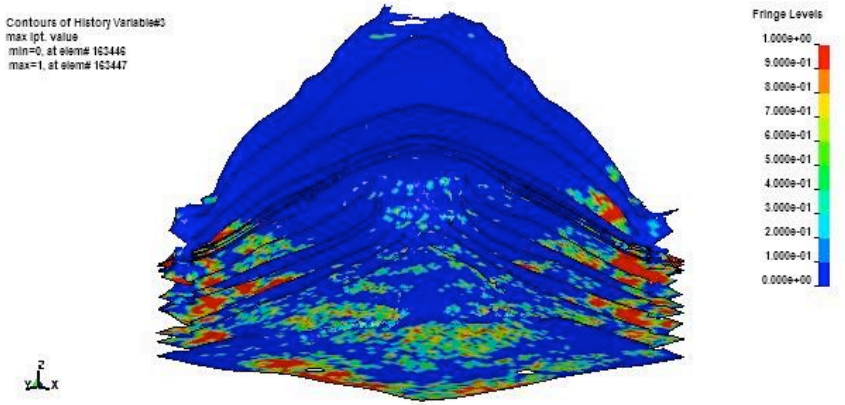

tensile matrix damage

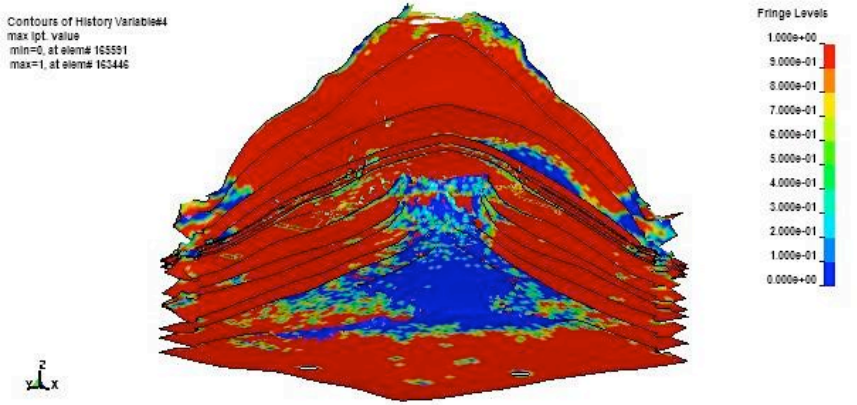

compressive matrix damage

Figure 75 – Damage maps S2 / Carbon 870 g

7.4 Numerical damage assessment and comparison with experimental results

Considering that the experimental damage assessment performed after blast tests (§5.8) is not possible to simulate and that the damage assessment plays a key role in the comparison of numerical and experimental results, a numerical failure criterion needs to be defined in order to evaluate model prediction capability. A numerical damage assessment criterion can be the matrix failure, both in tension and in compression. In fact, the water penetration through the panel thickness of experimental damage assessment can be much more easily associated with matrix failure rather than fibre breakage.

Hence, assuming the matrix failure in tension and compression as numerical failure criteria in the damage assessment, it can be noted that:

- tensile matrix damage is always present through all the panel thickness in all examined cases;
- for CFRP models, the compressive matrix damage zone is present along the whole central thickness in the case of 875 g blast load (Figure 67), while is almost absent in the case of 750 g blast load (Figure 66);
- for E/Carbon hybrid models, the compressive damage zone is spread in both 675 g and 750 g blast load, also if in the case of 675 g blast load there are few plies that appear undamaged (Figure 70);
- for S2/Carbon hybrid models, in the case of 875 g blast load (Figure 75) there is a compressive matrix damage zone that propagates for a slightly deeper zone than that obtained with 750 g blast load (Figure 74).

Furthermore, in the case of S2/Carbon hybrid models only for 875 g blast load a through the thickness fibre failure damage was observed. This agrees well with the experimental data showing that the composite panel was not able to resist to the considered blast load as found during the experimental campaign. As expected wider delamination damage was generally observed for the higher blast loads case and as observed in Figure 64, Figure 65, Figure 68, Figure 69, Figure 72 and Figure 73 the delamination occurred during the initial loading while, after the initial bending, delamination started to spread

toward the constrained edges. Finally, in Figure 76, Figure 77 and Figure 78 numerical results are also compared with provided real damage morphology showing a fairly good agreement.

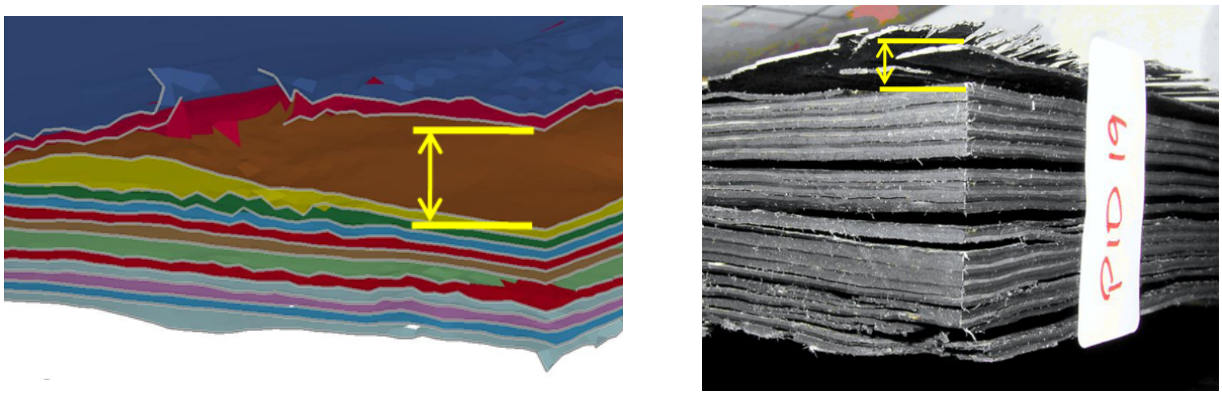

Figure 76 – CFRP delamination (750 g C-4)

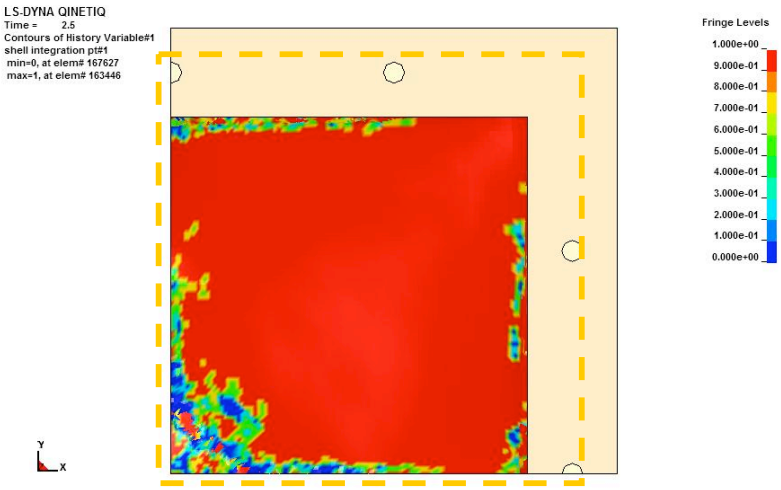

750 g C-4

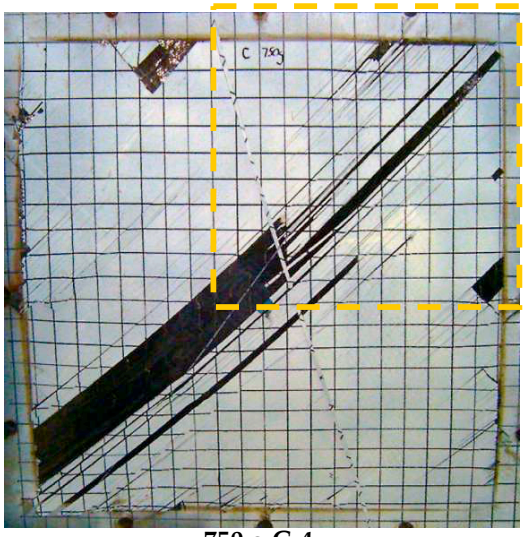

750 g C-4

Figure 77 – CFRP rear surface damage

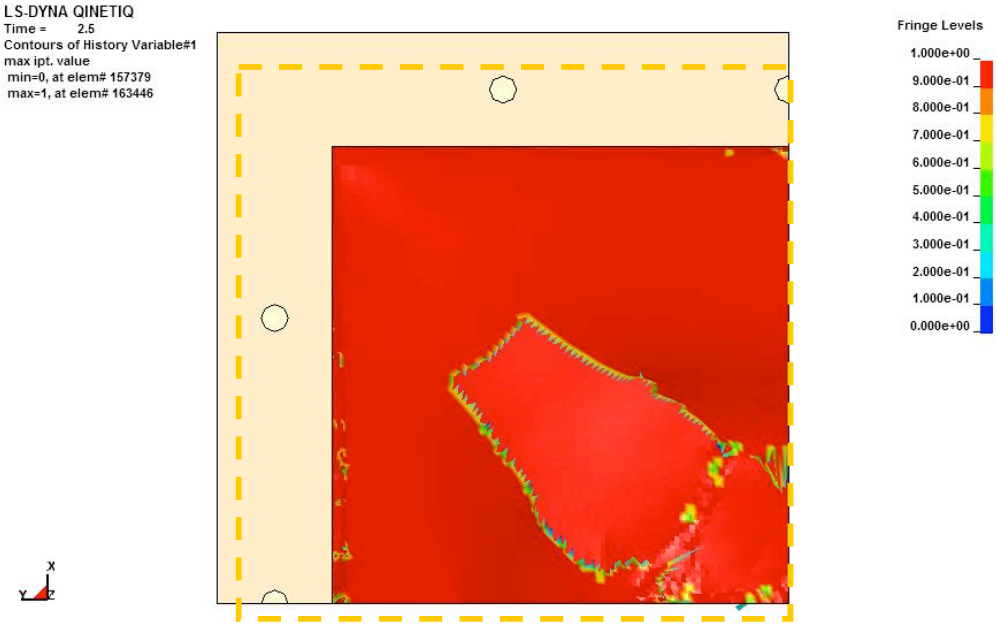

870 g C-4

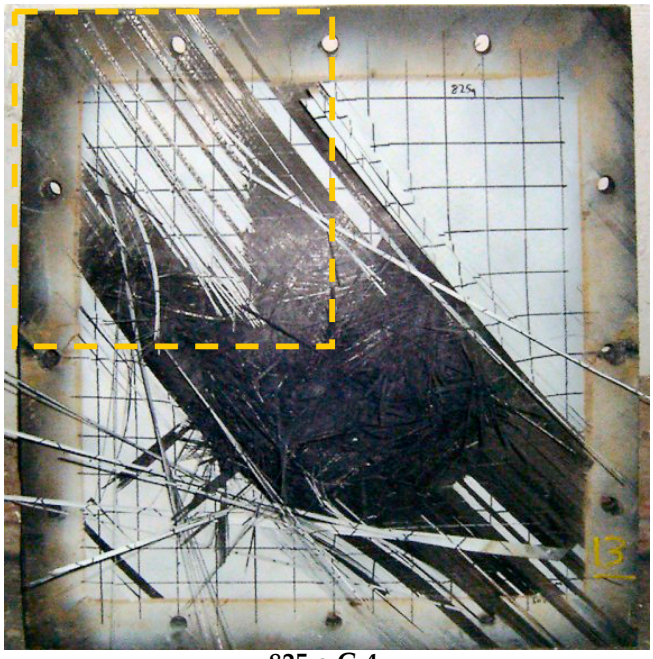

825 g C-4

Figure 78 – CFRP rear surface damage

This page is intentionally left blank

FINAL DISCUSSION AND CONCLUSIONS

The study examined the performance of both metallic and composite plates subjected to blast loads using commercial Finite Element Method (FEM) explicit code LS-DYNA.
The thesis dealt with numerical 3D simulations of response caused by air blast waves generated by C-4 charges on fully clamped rectangular targets.
Two different approaches were used to simulate the blast load.
Firstly CONWEP load function was applied in order to generate the blast equivalent pressure distribution on the Lagrangian plate model.
The second approach considered Multi Materials Arbitrary Lagrangian Eulerian (MMALE) formulation to simulate the shock phenomenon.
Numerical results were presented and compared with the tests performed by the EUROPA Research Technology Programme (RTP) military consortium and kindly provided by QinetiQ®.
Summarising both steel and composite target models results, it can be argued that fairly good agreement between numerical and experimental results has been achieved.

In particular, for the steel model simulations excellent results were obtained for low-scaled distance [§2.4] in terms of both dynamic and residual deflection. Furthermore, considering that experimental results provided for steel plates are slightly incoherent in terms of residual deformation, it could be argued that numerical models are able to predict very well the mechanical behaviour of steel plates also for high-scaled distance.

Regarding the composite models, first of all it should be considered that the experimental damage assessment performed after blast tests could not be performed numerically through the numerical approach used in this thesis. In consideration that the damage assessment plays a key role in the comparison process of numerical and experimental results, a numerical

failure criterion different from the experimental one was defined in order to evaluate model prediction capability. The matrix failure, both in tension and in compression, was the numerical damage assessment criterion selected. In fact, the water penetration through the panel thickness of experimental damage assessment can be much more easily associated with matrix failure rather than fibres breakage.

For S2/Carbon hybrid models assuming matrix failure in tension as failure criterion, it was found that in the case of 875 g blast load there is a compressive matrix damage zone that propagates for a slightly deeper zone than that obtained with 750 g blast load, while only for 875 g blast load a through the thickness fiber failure damage was observed.

For E/Carbon hybrid models, the compressive damage zone in the matrix resulted fairly spread for both 675 g and 750 g blast tests, also if in the case of 675 g a larger number of undamaged plies was observed.

The compressive matrix damage zone was found along the whole central thickness for CFRP models only in the case of 875 g blast load, while is almost absent in the case of 750 g blast load. This agrees very well with the experimental data showing that the composite panel was not able to resist the blast load experienced during the experimental campaign.

Hence, assuming the composite matrix failure as the damage criterion, the models very well simulated the CFRP armour tests, while in the case of hybrid targets the model's capability to predict the experimental results is slightly less reliable, probably due to the data applied in the hybrid interface delamination model. Nevertheless it needs to be taken into account that also for the composite plates tests, as for the metal ones, an uncertainty remains in the experimental measurement due to the reason that, because of the high cost related to each blast trial, there is not a sufficient number of an experimental result to provide reliable statistic data.

Finally, a reasonably good agreement between numerical and experimental results was found in terms of fracture morphology.

This page is intentionally left blank

BIBLIOGRAPHY

1. Remennikov, A.M., *A review of methods for predicting bomb blast effects on buildings.* Journal of Battlefield Technology, 2003. **6**(3): p. 5-10.
2. Wang, J., *Simulation of landmine explosion using LS-DYNA 3D software. Benchmark work of simulation of explosion in soil and air*, D.o.D.-W.S.D.A.a.M.R. Laboratory, Editor. 2001, DSTO Aeronautical and Maritime Research Laboratory: 506 Lorimer St Fishermans Bend Vic 3207 Australia.
3. Zukas, J.A., *Introduction to hydrocodes*. 2004, Amsterdam: Elsevier.
4. Jones, N., T.O. Uran, and S.A. Tekin, *The dynamic plastic behavior of fully clamped rectangular plates.* International Journal of Solids and Structures, 1970. **6**(12): p. 1499-1512.
5. Jones, N., R.N. Griffin, and R.E. Van Duzer, *An experimental study into the dynamic plastic behaviour of wide beams and rectangular plates.* International Journal of Mechanical Sciences, 1971. **13**(8): p. 721-735.
6. Menkes, S.B. and H.J. Opat, *Tearing and shear failures in explosively loaded clamped beams.* . Experimental Mechanics, 1973. **13**(11): p. 480-486.
7. Nurick, G.N. and J.B. Martin, *Deformation of thin plates subjected to impulsive loading -- A review. Part I: Theoretical considerations.* International Journal of Impact Engineering, 1989. **8**(2): p. 159-170.
8. Nurick, G.N. and J.B. Martin, *Deformation of thin plates subjected to impulsive loading -- A review. Part II: Experimental studies.* International Journal of Impact Engineering, 1989. **8**(2): p. 171-186.
9. Teeling-Smith, R.G. and G.N. Nurick, *The deformation and tearing of thin circular plates subjected to impulsive loads.* International Journal of Impact Engineering, 1991. **11**(1): p. 77-91.
10. Yu, T.X. and F.L. Chen, *The large deflection dynamic plastic response of rectangular plates.* International Journal of Impact Engineering, 1992. **12**(4): p. 605-616.
11. Olson, M.D., G.N. Nurick, and J.R. Fagnan, *Deformation and rupture of blast loaded square plates--predictions and experiments.* International Journal of Impact Engineering, 1993. **13**(2): p. 279-291.
12. Shen, W.Q. and N. Jones, *Dynamic response and failure of fully clamped circular plates under impulsive loading.* International Journal of Impact Engineering, 1993. **13**(2): p. 259-278.
13. Nurick, G.N., M.E. Gelman, and N.S. Marshall, *Tearing of blast loaded plates with clamped boundary conditions.* International Journal of Impact Engineering, 1996. **18**(7-8): p. 803-827.
14. Nurick, G.N. and G.C. Shave, *The deformation and tearing of thin square plates subjected to impulsive loads - An experimental study.* International Journal of Impact Engineering, 1996. **18**(1): p. 99-116.
15. Bonorchis, D. and G.N. Nurick, *The influence of boundary conditions on the loading of rectangular plates subjected to localised blast loading - importance in numerical simulations.* International Journal of Impact Engineering, 2008. **In Press, Accepted Manuscript**.

16. Chung Kim Yuen, S. and G.N. Nurick, *The significance of the thickness of a plate when subjected to localised blast loads.*, in *16th International Symposium on Military Aspects of Blast andShock, (MABS16)*. 2000: Oxford, UK.
17. Nurick, G.N. and A.M. Radford, *Deformation and tearing of clamped circular plates subjected to localised central blast loads.*, in *Recent developments in computational and applied mechanics - a volume in honour of John B. Martin.*, R. BD, Editor. 1997, CIMNE: Barcelona, Spain. p. 277-301.
18. Radford, A.M. and G.N. Nurick. *Circular plates subjected to localised central blast loads.In: Transient loading and response of structures*. in *An International Symposium Honouring Mr Arnfinn Jessen*. 1998. Trondheim, Norway.
19. Wiehahn, M.A., *Circular plates subjected to localised blast load – some insights into the mechanism of tearing and the energy required*. 2000, University of Cape Town.
20. Wiehahn, M.A., G.N. Nurick, and H.C. Bowles, *Some insights into the mechanism of the deformation and tearing of thin plates at high strain rates incorporating temperature dependent material properties* in *Structures under shock and impact*, N. Jones and C.A. Brebbia, Editors. 2000, WIT Press/Computational Mechanics Publications: Southampton, UK. p. 207-20.
21. Wierzbicki, T. and G.N. Nurick, *Large deformation of thin plates under localised impulsive loading.* International Journal of Impact Engineering, 1996. **18**(7-8): p. 899-918.
22. Mouritz, A.P., D.S. Saunders, and S. Buckley, *The damage and failure of GRP laminates by underwater explosion shock loading.* Composites, 1994. **25**(6): p. 431-437.
23. Mouritz, A.P., *The effect of underwater explosion shock loading on the fatigue behaviour of GRP laminates.* Composites, 1995. **26**(1): p. 3-9.
24. Mouritz, A.P., *The damage to stitched GRP laminates by underwater explosion shock loading.* Composites Science and Technology, 1995. **55**(4): p. 365-374.
25. Mouritz, A.P., *Effect of processing on the underwater explosion shock behaviour of GRP laminates.* Journal of Composite Materials 1995. **29**(18): p. 2488-2503.
26. Mouritz, A.P., *The effect of underwater explosion shock loading on the flexural properties of grp laminates.* International Journal of Impact Engineering, 1996. **18**(2): p. 129-139.
27. Comtois, J.L.R., M.R. Edwards, and M.C. Oakes, *The effect of explosives on polymer matrix composite laminates.* Composites Part A: Applied Science and Manufacturing, 1999. **30**(3): p. 181-190.
28. Franz, T., G.N. Nurick, and M.J. Perry, *Experimental investigation into the response of chopped-strand mat glassfibre laminates to blast loading.* International Journal of Impact Engineering, 2002. **27**(6): p. 639-667.
29. Langdon, G.S., W.J. Cantwell, and G.N. Nurick, *The blast response of novel thermoplastic-based fibre-metal laminates - some preliminary results and observations.* Composites Science and Technology, 2005. **65**(6): p. 861-872.
30. Lemanski, S.L., et al., *Understanding the behaviour of fibre metal laminates subjected to localised blast loading.* Composite Structures, 2006. **76**(1-2): p. 82-87.
31. Langdon, G.S., W.J. Cantwell, and G.N. Nurick, *Localised blast loading of fibre-metal laminates with a polyamide matrix.* Composites Part B: Engineering, 2007. **38**(7-8): p. 902-913.
32. Nurick, G.N., et al., *Deformation and tearing of blast-loaded stiffened square plates.* International Journal of Impact Engineering, 1995. **16**(2): p. 273-291.
33. Rudrapatna, N.S., R. Vaziri, and M.D. Olson, *Deformation and failure of blast-loaded square plates.* International Journal of Impact Engineering, 1999. **22**(4): p. 449-467.
34. Rudrapatna, N.S., R. Vaziri, and M.D. Olson, *Deformation and failure of blast-loaded stiffened plates.* International Journal of Impact Engineering, 2000. **24**(5): p. 457-474.

35. Jacob, N., et al., *Scaling aspects of quadrangular plates subjected to localised blast load-experiments and predictions.* International Journal of Impact Engineering, 2004. **30**(8-9): p. 1179-1208.
36. Ramajeyathilagam, K. and C.P. Vendhan, *Deformation and rupture of thin rectangular plates subjected to underwater shock.* International Journal of Impact Engineering, 2004. **30**(6): p. 699-719.
37. Balden, V.H. and G.N. Nurick, *Numerical simulation of the post-failure motion of steel plates subjected to blast loading.* International Journal of Impact Engineering, 2005. **32**(1-4): p. 14-34.
38. Nurick, G.N. and M.W. Bryant, *Fragmentation damage as a result of an explosion*, in *Plasticity and impact mechanics*, G. NK Editor. 1996: New Delhi, India. p. 484-498.
39. Langdon, G.S., S.C.K. Yuen, and G.N. Nurick, *Experimental and numerical studies on the response of quadrangular stiffened plates. Part II: localised blast loading.* International Journal of Impact Engineering, 2005. **31**(1): p. 85-111.
40. Chung Kim Yuen, S. and G.N. Nurick, *Experimental and numerical studies on the response of quadrangular stiffened plates. Part I: subjected to uniform blast load.* International Journal of Impact Engineering, 2005. **31**(1): p. 55-83.
41. Gupta, N.K. and Nagesh, *Deformation and tearing of circular plates with varying support conditions under uniform impulsive loads.* International Journal of Impact Engineering, 2007. **34**(1): p. 42-59.
42. Jones, N., *Plastic failure of ductile beams loaded dynamically.* Journal of Engineering for Industry - Transactions of the ASME, 1976. **98 (B1)**: p. 131-6.
43. Wright, A.J., *EUROPA CAFV Programme - Numerical Modelling Study*. 2006, QinetiQ.
44. Strehlow, R.A. and W.E. Baker, *The characterization and evaluation of accidental explosions.* Progress in Energy and Combustion Science, 1976. **2**(1): p. 27-60.
45. Anderson, C.R.W.a.J.G., *An Introduction to Detonation and Blast for the Non-Specialist*, D.o.D.-W.S.D.S.S. Laboratory, Editor. 2003, DSTO Systems Sciences Laboratory: PO Box 1500 Edinburgh South Australia 5111 Australia.
46. Cooper, P., *Explosives Engineering*. 1996, New York: Wiley-VCH.
47. Crawford, R.E., C.J. Higgins, and E.H. Bultmann, *The Air Force Manual for Design and Analysis of Hardened Structures*. 1974, Air Force Weapons Laboratory.
48. Barbagelata, A. and M. Primavori, *Blast on surface structures*, in *Shock and Impact on Structures*, C.A. Brebbia and V. Sanchez-Galvez, Editors. 1994, Computational Mechanics Publications: Southampton, UK.
49. Kinney, G.F., *Explosive Shocks in Air*. 1962, Monterey, California: The Macmillan Company.
50. Baker, W.E., et al., *Explosion hazards and evaluation*. Fundamental Studies in Engineering 5. 1983, Amsterdam - Oxford - New York: Elsevier Scientific Publishing Company.
51. Krauthammer, T., *AISC research on structural steel to resist blast and progressive collapse*. 1999, Penn State University.
52. Huffington, N.J., Jr. and W.O. Ewing, *Reflected Impulse Near Spherical Charges*. 1985.
53. Kinney and Graham. *Accident scenarios involving high explosives*. 1985 [cited; Available from: http://www.globalsecurity.org/wmd/library/report/enviro/eis-0157/eis0157_d4.html#7678.
54. *Structures to resist the effects of accidental explosions, AFM 88-22*. 1969, Department of the Army, the Navy and the Air Force: Washington.
55. *Structures to resist the effects of accidental explosions, A272342*. 1990, U.S. Department of Defense Explosives Safetyboard: Alexandria VA.

56. Kingery, C.N. and G. Bulmash, *Airblast parametrs from TNT spherical air burst and hemispherical surface burst*. 1984, U.S. Army BRL: Aberdeen Proving Ground.
57. Hyde, D.W., *CONWEP: Conventional Weapons Effects Program*. 1991: US Army Engineer Waterways Experiment Station, USA.
58. Randers-Pehrson, G. and K.A. Bannister, *Airblast Loading Model for DYNA2D and DYNA3D*. 1997, Army Researcg Lab Aberdeen Proving Ground MD.
59. *LS-DYNA keyword user's manual - Vol. I-II*, v. 971, Editor. 2007, Liveromore Software Technology Corporation (LSTC).
60. Matthews, F.L., et al., *Finite element modelling of composite and structures*. 2000, Abington: Woodhead Publishing Limited.
61. Belytschko, T., W. Liu, and B. Moran, *Nonlinear Finite Elements for Continua and Structures*. 2000.
62. Belytschko, T. and B. Moran, *Solution methods and stability*, in *Solution methods*. 1998, Nothwestern University.
63. Cook, R.D., D.S. Malkus, and M.E. Plesha, *Concepts and applications of Finite Element Analysis*. 2002: John Wiley & Sons. Inc.
64. Hallquist, J.O., *LS-DYNA theory manual*. 2006, Livermore Software Technology Corporation (LSTC).
65. Anderson, J.C.E., *An overview of the theory of hydrocodes.* International Journal of Impact Engineering, 1987. **5**(1-4): p. 33-59.
66. Barbero, E.J., *Finite Element Analysis of Composite Materials*. 2008: CRC Press.
67. Chang, F.K. and K.Y. Chang, *A Progressive Damage Model for Laminated Composites Containing Stress Concentrations.* Journal of Composite Materials, 1987. 21(9): p. 834-855.
68. Jones, C., S. Rook, and A. Rezai, WP2.1 Mechanical testing of carbon and carbon/glass hybrids. 2006, QinetiQ.
69. Jenkins, T.F., et al., Use of snow-covered ranges to estimate explosives residues from high-order detonations of army munitions. Thermochimica Acta, 2002. 384(1-2): p. 173-185.
70. Morris, A.J. and R. Vignjevic, *Consistent finite element structural analysis and error controls.* Computer Methods in Applied Mechanics and Engineering, 1997. **140**: p. 87-108.
71. Hughes, T.J.R. and W.K. Liu, *Nonlinear finite element analysis of shells-part II. two-dimensional shells.* Computer Methods in Applied Mechanics and Engineering, 1981. **27**(2): p. 167-181.
72. Hughes, T.J.R. and W.K. Liu, *Nonlinear finite element analysis of shells: Part I. three-dimensional shells.* Computer Methods in Applied Mechanics and Engineering, 1981. **26**(3): p. 331-362.
73. Johnson, G.R. and W.H. Cook, *Fracture characteristics of three metals subjected to various strains, strain rates, temperatures and pressures.* Engineering Fracture Mechanics, 1985. **21**(1): p. 31-48.
74. 2008 [cited; Available from: http://www.dynasupport.com/support-1/how-tos/hourglass/?searchterm=hourglass.
75 Tsai, S. W. and Wu, E. M., *A general theory of strength for anisotropic materials*. Journal of Composite Materials, 1971. vol. 5, p. 58-80.
76. Taylor and Francis, *Introduction to Composite Materials Design*. 1999.
77. [cited; Available from: http://www.agy.com/technical_info/graphics_PDFs/Advanced_Materials.pdf]
78. Naik, N.K., Y. Chandra Sekher, and S. Meduri, *Damage in woven-fabric composites subjected to low-velocity impact.* Composites Science and Technology, 2000. **60**(5): p. 731-744.
79. Bala, S., *Tie-Break Contacts in LS-DYNA* Livermore Software.
80. Lemmen, P.P.M. and G.J. Meijer, *Failure Prediction Tool Theory and User Manual*. 2001, TNO Report.

81. Michael J. Mullin, B.J.O.T. *Simulation of Energy Absorbing Materials in Blast Loaded Structures*. in *8th International LS-DYNA Users Conference*. 2004.har